UNIVERSITAT DE BARCELONA

Self-assembled molecules as efficient selective contacts in translucent quantum-dot light emitting diodes

Sarika Kumari

Self-assembled molecules as selective contacts in quantum-dot light emitting diodes.

Sarika Kumari

UNIVERSITAT DE BARCELONA

Programme of Nanoscience

Self-assembled molecules as selective contacts in quantum-dot light emitting diodes

Sarika Kumari

Supervised by

Dra. Eugenia Martínez Ferrero

Eurecat Centre Tecnològic de Catalunya

Institut Català d'Investigació Química (ICIQ)

Prof. Emilio Palomares Gil

Institut Català d'Investigació Química (ICIQ)

Thesis Tutor

Dr. Guillem Aromí Bedmar

Department of Inorganic Chemistry, University of Barcelona (UB)

Tarragona – September 2023

Outline of Thesis

Emilio Palomares Gil, Director, and group leader at the Institut of Chemical Research of Catalonia (ICIQ) in Tarragona, and research professor of the Catalan Institution for Research and Advanced Studies (ICREA) in Barcelona.

Dra. Eugenia Martinez Ferrero, Head of the photonics line in Technological Centre of Catalunya, Eurecat Mataro and currently, scientific group coordinator at ICIQ.

CERTIFY:

That the presented research study, entitled "Self-assembled molecules as efficient selective contacts in translucent quantum-dot light emitting diodes" by **Sarika Kumari** for the award of the degree of Doctor of Philosophy (Ph.D.), has been carried out under our supervision at ICIQ and Eurecat.

Tarragona, September 2023

Dra. Eugenia Martínez Ferrero   Dr. Guillem Aromí Bedmar   Prof. Emilio Palomares Gil

Eurecat Centre of Technology   University of Barcelona   Institute of Chemical

  Catalunya and Institute of   Research of Catalunya

Chemical Research of Catalunya

Acknowledgements

First and foremost, I would like to express my gratitude to very grateful for my Supervisors, Prof. Emilio Palomares and Dra. Eugenia Martinez Ferrero for trusting me and giving me the opportunity of working with them. Thank you for your kind support, guidance and encouragement throughout my journey. I am also grateful for the support of Prof. Iván Mora Seró during my short stay at INAM (Institute of advanced materials). I am grateful to Dr. Laura and Dr. Paul for their kind support during my stay at Eurecat, Mataro and for their support during my thesis.

I am thankful to all the Palomares group for creating a friendly, enjoyable and healthy atmosphere in the laboratory. Thanks to Dr. Sofia, Dr. Ilario, Dr. Jose, Dr. Maria, Dr. Wenhui, Dr. Ece, Dr. Jesus, Dr. Lijun, Dr. Lyu, Dr. Eyüp, Dora, Ece, Joan Marc, Laia, Bea for being so kind and for all the good times. Further, I want to express my gratitude to Santi for showing up every time I need any help. I want to thank Sorania, Beatriz and Aurora, for their kind help. Once again, I want to thank Palomares group for sharing the coffee breaks and a lot of sweets.

I am thankful to Dr. Andrés, Dr. Samrat, Dr. Sofia, Dr. Rafael, Dr. Juan, Dr. Silver, Alex for making my stay at INAM very convenient and for the Barbecue we had. Thanks to Mousumi, Pam and Dr. Somnath for the weekend dinner and making it home.

I would like to thank my friends Deepika, Adithya and Vinayak for their endless support during my stay in Tarragona. Thanks to Dr. Sharmistha for being my elder sister and sharing a lot of wisdom with me. Thanks to Dr. Thiru, Inderjeet, Dr. Sukruth, Suresh and Koushik for hosting dinners and cheering me up when I needed it most. I am also thankful to Dr. Aanchal, Dr. Laxmi, Gokul, Satyam for sharing some nice times. I want to thank Saptam for his love, affection and all the emotional roller coaster since last 4 years. I cannot thank enough to my dear friend Aleria who has stayed by my side since we first met.

I feel enormous gratification towards my family for making me what I am today and giving me different kinds of ideas, which can come from a large family.

"Science and technology go hand in hand in advancing society"

— **Albert Einstein**

Dedicated;

To my beloved parents (Mr. Mukhtyar Singh and Mrs. Sangeeta),

my brothers (Kapil and Shubham),

and my sisters (Sunita and Varsha).

Abstract

Since the last two decades, nanotechnology has been revolutionary for representing small solutions to the big problems. Nanoscience and Nanotechnology spread from the area of Electronics, Energy and Environment to Biomedicine, Food or Textile where it has made possible to selectively target the cells to repair the damaged genes. It has also made it possible to convert more sunlight into energy with efficient solar panels. Nanostructured materials make faster and more efficient microchips. It also contributes to making biosensors detect pollutants in bodies. Today, nanomaterials have made it possible to fabricate LEDs of different colors.

Colloidal quantum dots technology has drawn huge attention in academia and industry since the last decade. Quantum dots are also called "Artificial Atoms" because they have discrete energy levels just like atoms. QDs are zero dimensional particles showing quantum confinement effect which means that their size comparable to Bohr radius and their colour can change with their size which is typically between 2-10 nm. On the other hand, these materials show excellent optical properties including high absorption, strong and narrow emission with high colour purity making them suitable for various applications.

Perovskites are crystalline materials with the structure of calcium titanium oxide. They are extensively used for several applications because of their easy manufacturing process, abundance, low cost, and great flexibility. Metal halide perovskites are popular for their vast range of applications in optoelectronic devices while metal oxide perovskites are widely used in chemicals, electrochemical and photocatalysis.

Self-assembled molecules (SAMs) are a class of materials which can attach to any substrate modifying the work function of the electrode for their diverse application. They consist of three components including terminal group, spacer group and anchoring group. SAMs are used to make organic and perovskite solar cells with better efficiency and stability. Nowadays, their application in perovskite LEDs has also emerged.

The present thesis is focused on the synthesis of perovskite nanocrystals and their application in perovskite nanocrystal LEDs (PeLEDs) and the preparation of QDLEDs based on cadmium selenide QDs. We have used SAMs as hole transporting layer in PeLEDs which is a good alternative to the conventional hole transport materials (HTMs). SAM are good for the overall performance of devices including luminance and stability but also promotes thin sized LEDs. With this regard, we have also employed a thin layer of PDINO as electron transport material (ETM) for fabricating red QDLEDs in combination with commercial CdSe@ZnS quantum dots as emissive material.

Finally, we have performed doping of a rare-earth element Dysprosium (Dy) in the methylammonium bromide (MAPbBr$_3$) Perovskite lattice at different concentration to find the optimum for our LEDs.

The work discussed in this thesis was carried out between March 2019 and March 2023 at the Institute of Chemical Research of Catalonia (ICIQ) and Eurecat, the Technological center of Catalonia.

Resum

Durant les dues últimes dècades, la nanotecnologia ha estat revolucionària per representar una petita solució als grans problemes. La nanociència i la nanotecnologia es van estendre des de l'àrea d'electrònica, energia i medi ambient fins a la biomedicina, l'alimentació i el tèxtil on ha permès dirigir selectivament les cèl·lules per reparar els gens danyats. També ha permès convertir més llum solar en energia amb plaques solars eficients. Els materials nanoestructurats fan que els microxips siguin més ràpids i eficients. També contribueix a fabricar biosensors per detectar contaminants en els cossos. Avui dia, els nanomaterials han permès fabricar els LED de diferents colors.

La tecnologia de punts quàntics col·loidals ha cridat una gran atenció al món acadèmic i a la indústria des de la dècada passada. Els punts quàntics (QDs), també anomenats "àtoms artificials", tenen nivells d'energia discrets igual que els àtoms. Els QD són partícules de zero dimensions que mostren un efecte de confinament quàntic, cosa que significa que la seva mida és comparable al radi de Bohr i el seu color pot canviar amb la seva mida, que normalment està entre 2 i 10 nm. D'altra banda, aquests materials tenen unes excel·lents propietats òptiques, com ara una alta absorció, emissió forta i estreta amb una gran puresa de color que els fa aptes per a diverses aplicacions.

Les perovskites són materials cristal·lins amb l'estructura d'òxid de calci de titani. S'utilitzen àmpliament per a diverses aplicacions a causa del seu procés de fabricació fàcil, abundància, menor cost i gran flexibilitat. Les perovskites d'halogenur metàl·lic són populars per la seva àmplia gamma d'aplicacions en dispositius optoelectrònics, mentre que les perovskites d'òxid metàl·lic s'utilitzen àmpliament en química, electroquímica i fotocatàlisi.

Les molècules auto assemblades (SAMs) són una classe de materials que poden unir-se a qualsevol substrat modificant la funció de treball de l'elèctrode permetent diverses aplicacions. Consten de tres components que inclouen el grup terminal, el grup espaiador i el grup d'ancoratge. Els SAM s'utilitzen per fabricar cèl·lules solars orgàniques i perovskites amb una millor eficiència i estabilitat. Actualment també ha sorgit la seva aplicació en LED de perovskita.

La present tesi se centra en la síntesi de nanocristalls de perovskita i la seva aplicació en PeLEDs i en la preparació de QDLEDs basats en QDs de seleniür de cadmi. Hem utilitzat SAMs com a capa de transportadora de buits en LED de nanocristall de perovskita, com a alternativa als transportadors de buits convencionals en PeLED. Els SAM són bons per al rendiment general dels dispositius, inclosa la luminància i l'estabilitat, però també promouen LEDs de mida fina. En aquest sentit, també hem emprat una fina capa de PDINO com a material transportador d'electrons per fabricar QDLED vermells, utilitzant punts quàntics comercials CdSe@ZnS com a material emissiu.

Finalment, hem realitzat el dopatge d'un element de terres rares Disprosi (Dy) a la xarxa de perovskita de bromur de metilamoni (MAPbBr$_3$) a diferents concentracions per trobar l'òptim per als nostres LED.

El treball tractat en aquesta tesi es va dur a terme entre març de 2019 i març de 2023 a l'Institut Català d'Investigació Química (ICIQ) i Eurecat; Centre Tecnològic de Catalunya.

Oral and Poster at Conference

- ✓ **Applied Light-Matter Interactions in Perovskite Semiconductors 2021;** Oral presentation (online) "Self-assembled monolayers as hole-transporting materials for increasing the performance of Perovskite $CsPbBr_3$ Quantum Dot Light Emitting Diodes"

- ✓ **ICIQ 5th PhD Day 2021;** Oral presentation "Self-assembled monolayers for better stability of $CsPbBr_3$ Nanocrystal Perovskite light emitting diodes"

- ✓ **International Conference on Emerging Light Emitting Materials 2022;** Poster presentation in Cyprus in-person (Limassol; Cyprus) **"PDINO as the self-assembled molecule electron transporting material in the inverted quantum-dot Light Emitting Diodes"**

- ✓ **ICIQ 6th PhD Day 2022;** Oral presentation "PDINO molecule for better stability of CdSe@ZnS quantum dot-based light emitting diodes"

- ✓ **Materials for sustainable development conference;** Poster presentation in-person (Valencia; Spain) "Enhancing the performance of the $MAPbBr_3$ Perovskite Light emitting diodes with the doping of magnetic species Dysprosium"

Table of Contents

List of Figures

List of Tables

Chapter 1: General Introduction

Abstract

This chapter introduces the topics that have been tackled in the thesis. We have studied perovskite QDs, CdSe@ZnS QDs and their application in fabricating our QDLEDs. Also, we have studied the new charge transport layers for QDLEDs.

In the last few decades self-assembled monolayers have been extensively used in various fields like biotechnology, nanotechnology, semiconductors etc. for their interesting properties. In this chapter we will discuss as well about the basic properties of SAMs and their applications in light emitting diodes. Also, the doping in perovskites and their application in PeLEDs.

1.1 General introduction of LEDs

Light Emitting Device (LED) in simple terms; is a semiconducting device which works on the principle of electroluminescence that emits light when current flows through it. When the voltage is applied to the device terminals, the electrons and holes are recombined in the p-n junction region releasing the photons. The color of the emitted light (photons) from the devices depends upon the bandgap of semiconductor material used.

In 1907, the electroluminescence phenomenon was discovered by British experimenter Henry Joseph Round. In 1927, the first LED construction was reported by a Soviet Inventor, Oleg Losev with the semiconductor silver carbide crystals. Until a decade, no practical use was discovered. In 1951, Kurt Lehovec, Carl Accardo and Edward Jamgochian interpreted the mechanism in a LED device with silicon carbide crystals. In 1955, Rubin Braunstein discovered the emission generated in devices with the alloys of semiconductors gallium antimonide (GaSb), gallium arsenide (GaAs), indium phosphide (InP), and silicon-germanium (SiGe) .

The first LED for commercial purpose was developed by American physicist Prof. Nick Holonyak in 1962 with red (visible emission) published in Applied Physics Letters on December 1, 1962[1]. Later yellow, red, and orange LEDs were invented by his students, M. George Craford and Russell Dupuis. Those first LEDs were used to replace incandescent bulbs and used as seven segment displays and digital watches. Later in 2014, for the discovery of efficient blue light LEDs; Shuji Nakamura and physicists Hiroshi Amano and Isamu Akasaki were awarded the Nobel Prize in Physics. The recent advances in the application of LEDs allows them to use in display screens and sensors and in advanced communicator technologies because of their high switching speed. Over the years, LEDs have shown their potential over conventional incandescent bulbs because of their low power required, longer lifespan, smaller size, better physical robustness, manufactured in different forms.

The light emitting device is a multilayered structure with two different architectures, normal and inverted structures (Figure 2). The device contains one anode which should be the material with high work function, transparent to pass the light out of the device. It has to be able to transfer the hole to the hole transporting material (HTM) which should be able to transport the holes to the next layer (emissive layer). Thus, the HTM should have the perfect hole mobility of nearly $2 \cdot 10^{-6}\,cm^2\,V^{-1}s^{-1}$ whereas its HOMO level should be lower than that of Emissive layer. Some examples of commonly used HTMs for LEDs

are poly(3,4-ethylenedioxythiophene) polystyrene sulfonate and (PEDOT: PSS) or Poly (N, N'-bis-4-butylphenyl-N, N'-bisphenyl) benzidine (Poly-TPD) shown in Figure 1 below.
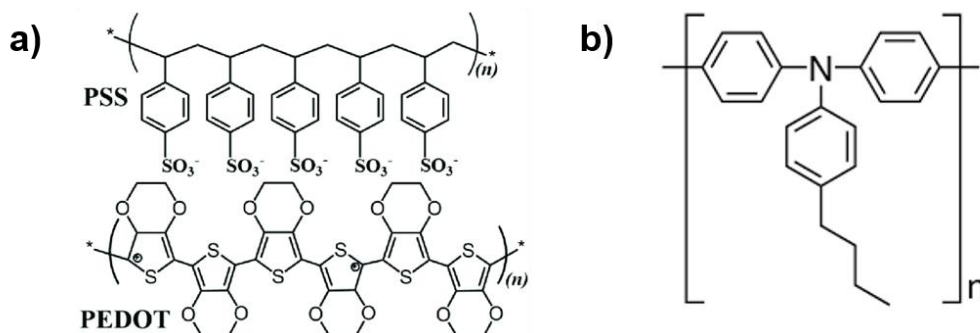
Figure 1 Chemical structure of a) PEDOT: PSS, b) Poly-TPD.

The EM layer should be robust enough to bear the applied voltage, some materials used as emissive layers in LEDs are Tris(8-hydroxyquinolinato) aluminium {Alq$_3$}, lead-halide perovskites (CsPbX$_3$, MAPbX$_3$) or Poly(9,9-dioctylfluorene-alt-benzothiadiazole) {F8BT}, among others. The electron transporting material (ETM) should be able to conduct the electrons hence it should have mobility of at least 10^{-6} cm^2 V^{-1}·s^{-1}. The LUMO level of ETM should be lower than the EML to inject the electron efficiently. The mobility of ETM should be lower than that of HTM. Some materials used as ETMs are 2,2',2''-(1,3,5-Benzinetriyl)-tris(1-phenyl-1-H-benzimidazole) {TPBi}, BPhen (Bathophenanthroline) and TmPyPB, 1,3,5-Tris(3-pyridyl-3-phenyl) benzene. The cathode is mostly an opaque metal which should have a low work function. The examples are Aluminum (Al), Silver (Ag), Gold (Au) etc.

The work function of cathode should be equal to the LUMO level of ETM. The hole and the electron injected in the LUMO and HOMO levels of the emissive material are then combined forming an exciton which recombines within and generate photons, in case of radiative recombination. If the mobility of the HTM is not optimized, then the transporting hole will continue to travel through the EML and crosses the interface to reach the ETM which results in not recombining in the emissive layer. Electrical leaks, short-circuits and electrical leaks that involve short-circuits are some of the drawbacks of LEDs.
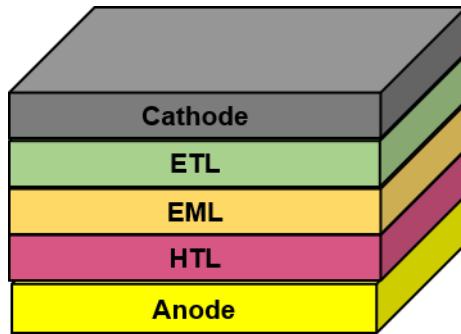
Figure 2 General structure of an OLED with normal structure.

1.1.1 Working Mechanism of LEDs

Light emitting diodes (LEDs) work on the principle of electroluminescence. When a forward bias is applied to the device between the anode and cathode, the electrons flow towards the cathode and the holes towards anode. The majority of charge carriers from the corresponding layers flow towards the emissive layer (if they can cross the barriers) by making the emissive layer negatively charged. Direct band gap semiconductors lead to the energy difference as the electron recombines to the holes by radiative recombination leading to the generation of photons. By the annihilation of an electron and hole, one photon generates. The band gap and chemical structure of the emissive material determines the color of the electroluminescence which is released from the device. Figure 3 illustrates the above mechanism of a typical OLED[2].
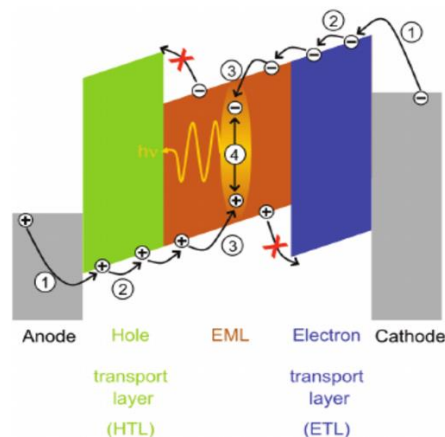
Figure 3 Working mechanism of an OLED.

1.1.2 Measurement of LEDs

After the fabrication, there are main parameters that explain the standard of a device. To characterize a light emitting diode there are few methods like using-

Camera - In the thesis, we have used the camera KONICA LS11. To measure the devices, the camera is placed on the top of device holder containing 4 devices at a time which is also connected to the voltage source while the camera is connected to the computer. We used home-made software for measuring luminance -voltage -current density and their lifetimes. To measure the CIE and EL, an extra Fibre optics cable attached with "Ocean Optics spectrometers" was used to place on the top of illuminated LED and record the data. The whole system was kept dark to avoid any outside light interaction.

Figure 4 Konica LS-110 for measuring the LEDs.

Photodiode - To measure the LEDs from a photodiode, one device at a time was put in the device holder. A photodiode was kept on the top of device holder and covered with a black cloth to protect any possible light and measured the devices with the software. The devices were measured with this system during my 3 months stay in Eurecat Mataro.
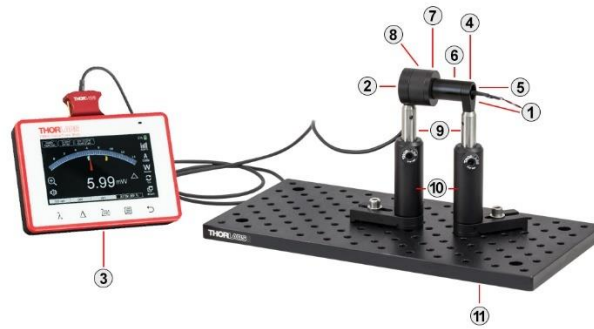
Figure 5 Photodiodes based set up to measure the LEDs

Integrated sphere - The integrated sphere is used to measure the devices. It is a sophisticated method to measure the devices where a device holder contains one device at a time. The integrated sphere is connected to the computer where the software is used to record the data of luminance-voltage-current density, Electroluminescence, CIE coordinates all at once. This method was used to measure the devices in my 2 weeks stay in INAM, Castello de la Plana. The integrated sphere has an inner surface made of light-scattering material to scatter the light uniformly.
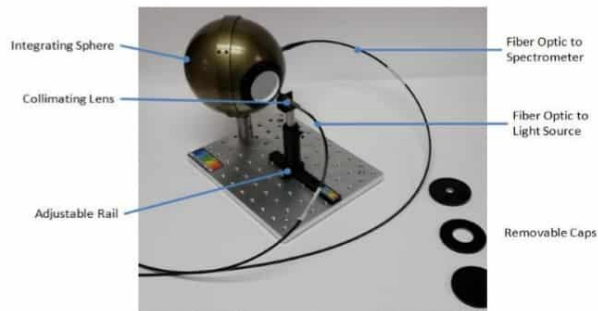
Figure 6 Integrated sphere based set up for measuring LEDs

1.1.3 Measurement parameters of a Light Emitting Diode

1. **Luminance** - The luminous intensity emitted from a light source per unit area in a given direction is called luminance and is measured in candela per square meter (Cd/m^2).

2. **Current density** - The Current flowing from a surface in per unit area is current density and is measured in mA/cm^2.
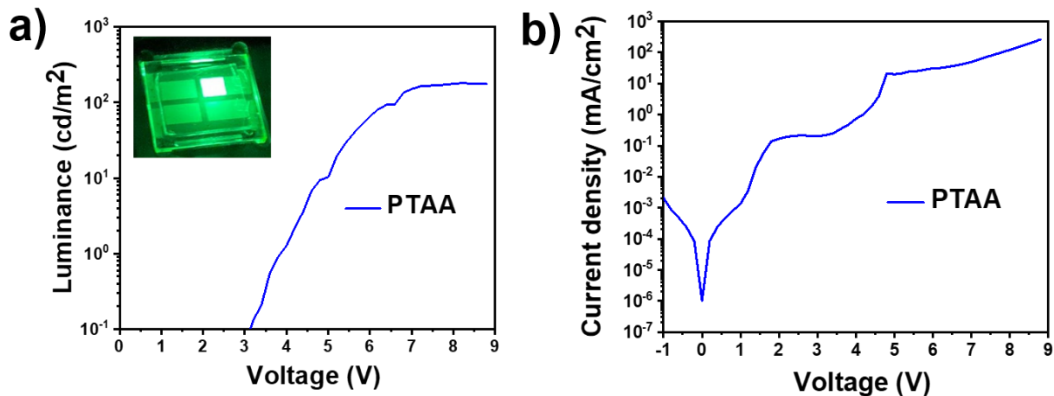
Figure 7 Luminance-Voltage-Current density curve of a PeLED prepared in our work

3. **Current Efficiency** – It is the ratio of the Luminance emitting from an illuminated Light emitting diode and the current density flowing from that device. The measurement unit of the current efficiency of the LED is Candela per Ampere (Cd/A).

4. **External Quantum Efficiency (EQE)** - It is defined as the ratio of emitted photons to the number of electrons injected into the device, which measures how efficiently the device converts electrons to photons. EQE is measured in (%).
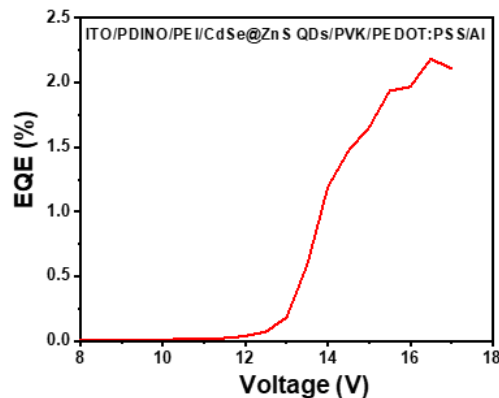
Figure 8 EQE vs Voltage curve of red QDLED prepared in our work

5. **Internal Quantum Efficiency (IQE)** - It is the proportion of electron–hole recombination that occurs radiatively in the emitter layer. IQE is measured in (%).

6. **Luminous Efficacy** – It is the ratio of emitted light (L) to injected energy (IV) by the source. It is the ratio of luminous flux to power measured in Lumens per watt.

7. **Electroluminescence (EL) –** It is the process by which photons are generated through a semiconductor device when the recombination of electron and hole pairs is induced by an external bias application.
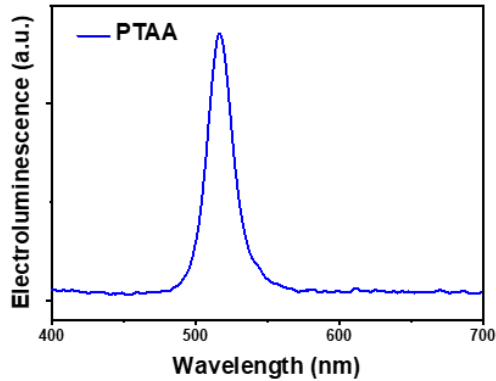
Figure 9 EL Intensity vs Wavelength for a PeLED.

8. **International Commission on Illumination (CIE) –** CIE 1931 xyz color space, or chromaticity coordinate is a coordinate system to establish the links between the wavelengths and the colors perceived by human eye which was established by **(Commission Internationale de l'Eclairage**) an international authority on light, illumination, colour, and colour spaces.
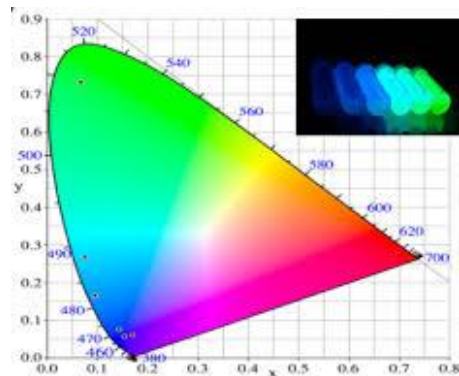
Figure 10 CIE coordinated graph of PSK QDs

9. **Radiant efficiency (RE) or Wall Plug Efficiency (WPE)** – is the electrical to optical energy conversion efficiency.

$$RE \text{ (or WPE)} = EQE.LE = \eta_{injection}. IQE.\eta_{extraction}. (L/I \cdot V)$$

Where, $\eta_{injection}$ is the proportion of electrons injected into the active emitter layer to the number of electrons passing through the device and $\eta_{extraction}$ is the proportion of generated photons in the emitter layer that exit the device.

1.2 Self-assembled monolayers: Introduction

According to Whitesides and Grzybowski, "Self-assembly is the autonomous organization of components into patterns and structures, without human interventions" [3] and self-assembly is a unifying concept in nature.

In optoelectronics, efficient light emitting devices have balanced charge carriers for the radiative-recombination process to happen in the emissive layer. For that, a few strategies have been proposed including interface engineering and choosing the best materials with charge carrier mobility, anode modification and chosen materials with suitable HOMO/LUMO energy levels[45]. Anode modification can be achieved by various methods like modification of the anode properties by the addition of a second material like metal oxide layer [6], spin coating of PEDOT: PSS [7], UV ozone treatment [8], oxygen plasma treatment [9], adding a graphene oxide layer [10], chlorination [11] etc.

Apart from such treatments, **Self-Assembled Monolayers (SAMs)** can be used for the same purpose which is turn out to be feasible because of their low cost, better stability in devices compared to other charge transport layers and having ability to change the properties of molecule by adjusting the structure of molecule by increasing or decreasing the component groups [12].

In other words, SAMs are used to modify the physicochemical properties like surface energy (which improves the wettability of organic materials on inorganic substrates) and shift the work function of inorganic substrates by forming covalent bonds at the interface [5].

A SAM molecule is typically composed of three parts:

1. The head group, which binds to the surface.
2. An aliphatic chain or an aromatic oligomer which is the backbone of the molecule, is responsible for the molecular ordering.
3. The terminal group determines the topography, surface energy and chemistry/properties of the outer interface.

By improving the carrier injection to the emissive layer, the performance of the device tends to improve[13]. SAMs does have a certain dipole moment because of which, the vacuum level of anode in the devices tries to align with the HOMO level of the SAM layer resulting in tuning of the work function of the metal. Hence, the dipole moment of the SAM is one of the important factors affecting the characteristics of the OLEDs [14].
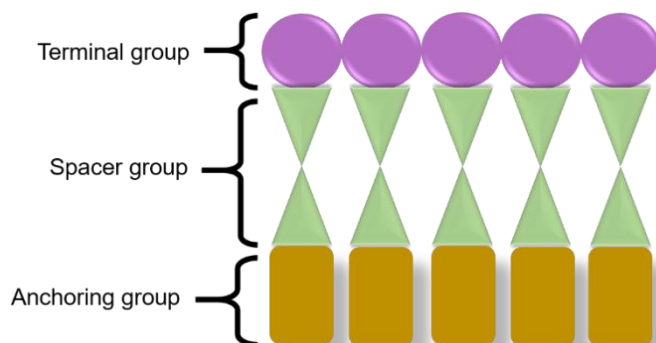
Figure 11. General structure of a SAM molecule

1.2.1 General properties of SAMs

SAMs can be either formed from molecules dissolved in solution or by condensation on a surface through gas phase.[15] The application of SAMs have been adopted for electrodes, dielectric and semiconducting surfaces to modulate the interfacial properties in organic electronic devices and proof to enhance the performance as well as stability of devices. SAMs have properties like optical transparency, electrical conductivity and electrochemical properties.

Few examples for the application of SAMs used as buffer layers and surface modification in organic thin film transistors [16]. SAMs can be fluorinated alkane, CF_3-terminated alkane, chloromethyl-terminated alkane. Generally, they are formed using $-SiCl_3$ [17] $-H_3PO_4$ [818], -COCl [19] or -COOH [20]. Apart from organic electronics, SAMs applications are versatile as following -

1.2.2 Application of SAMs

There are various fields where SAMs have been applied; some of them are in selective adsorption of protein to a substrate. The possibility of controlling the immobilization of proteins was an important step in the development of bioelectronics. This was achieved by two methods: First is Physisorption, which includes the electrostatic interaction between the terminal groups of SAMs and the protein; or the hydrophobic interaction between the terminal groups of SAMs and the biomolecule [21]. The second method is by forming covalent bonds with the biomolecules [22].

Self-Assembled Monolayers robustness and versatile nature was expanded to their applications in synapstors, biosensors, non-volatile memory, and logic circuitry. SAMs have been applied to biomedical devices for in vitro experiments[23], the point-of care test (POCT), implantable devices, environmental monitoring[24], wearable electronics, robotics[25] and low-cost disposable circuits[26].

Self-assembled monolayers have also increased charge transfer properties at the interface, decrease the charge recombination and better compatibility at the interface in organic solar cells [27]. leading to better charge extraction, and improvement of overall solar cell performance by improving open-circuit voltage, lowering hysteresis and better surface charge recombination

In 2016, Chun-Chu Lin et al investigated the effect of carboxylic acid and phosphonic acid-based SAMs to modify the TiO_2 electrode in dye-sensitized solar cells [28].

In Mesoporous structured perovskite solar cells, perovskite materials infiltrates into the mesoporous TiO_2 layer and because of the poor energy alignment, it has bad crystal growth on the mesoporous material [29]. To overcome this issue, Abrusci et al. in 2013 introduced a C_{60} based SAMs layer between perovskite and the mesoporous TiO_2 and observed an improvement in the open-circuit voltage and the short-circuit current [30].

For the first time perovskite solar cells with SAMs as hole transporting material was published by E. Yacin et al, with inverted structure of $ITO/SAMs/MAPbI_3/PC_{60}BM/Ag$. Two molecules, MC-43 and TPA were synthesized and reportedly increased the power conversion efficiency of solar cells compared to the solar cells with PEDOT: PSS layer[31].

1.2.3 SAMs in LEDs

In 2000, Appleyard et al used four different SAMs (phosphonic acids) (2-chloroethyl) phosphonic acid, (amino methyl) phosphonic acid, (trichloromethyl)phosphonic acid, (4-nitrophenyl) phosphonic acid investigating that the ITO/TPD interface with SAM has increased the work function by 0.3 eV in comparison to the ITO/TPD without SAM confirmed by scanning kelvin probe. In the device structure $ITO/SAM/TPD/Alq_3/Al$, *the* turn on voltage decreased by 4 V and the maximum luminance was increased by 3.5 times [32].

Manna et al in 2006 investigated that the use of SAM 1-decanethiol (H-$S(CH_2)_9CH_3$) between the cathode and the emissive region decreased the turn on voltage from 22 V

to 16 V in their device (ITO/TPD/Alq$_3$/SAM/Al), the brightness increased by 5 times and the quantum efficiency increased by 0.051% [33].

In 2012, Wang et al investigated that fluorinated phosphonic acid SAM layers increase the work function of ITO 0.15-0.4 eV in comparison to PEDOT: PSS. In the device structure, ITO/HTL/poly-TPD (40nm)/PFO: MEH-PPV (70 nm)/Ca (20 nm)/Al (70 nm) they found better charge injection in the devices containing SAMs resulting in luminous efficiency 10 times higher than that of devices without SAMs [34].

In 2016, Yalcin *et al* synthesized two SAM molecules, TPA and CAR and employed in the electroluminescent cells with structure ITO/SAMs/TPD/Alq3/Al and found that the molecules have increased the performance of the devices [35].

In the same year, Mori et al investigated that alkyl chain lengths of SAMs have also an effect on the ITO work function. They used fluorinated SAMs such as $CF_3(CH_2)_2Si$ $(OC_2H_5)_3$, $CF_3(CF_2)_5(CH_2)_2Si$ $(OC_2H_5)_3$, $CF_3(CF_2)_7(CH_2)_2Si$ $(OC_2H_5)_3$, $CF_3(CF_2)_9(CH_2)_2Si$ $(OC_2H_5)_3$ as F$_3$SAM, F$_8$SAM, F$_{10}$SAM and F$_{12}$SAM and showed that they increase the hole injection from ITO and improved the device lifetime for OLEDs [36].

In 2017, Sang -Geon Park et al, fabricated and compared devices with Heptadecafluoro-1,1,2,2-tetrahydrodecyl) triethoxysilane as SAM HIL (Hole injection layer), without HIL and PEDOT: PSS as HIL and found that the driving voltage among all the HILs was the lowest among all in the device architectures of ITO/with and without FSAM or PEDOT: PSS/GreenK2 (50~80 nm)/LiF(0.6 nm)/Al(150 nm). The authors suggested that the SAMs could replace PEDOT: PSS. [37].

In 2018, Zheng et al investigated that the use of SAMs, pentaflurobenzylphosphonic acid (F$_5$BPA) and heneicosaflourododecyl phosphonic acid (HF$_{21}$DPA) increased the work function of ITO from 4.82 eV to 5.20 eV and 5.81 eV, respectively. In the device performance, the turn on voltage could decrease form 4.2 V for bare ITO to 2.9 V for F$_5$BPA and 2.8 V for HF$_{21}$DPA modified devices. SAM based OLEDs reached 29,000 cd/m^2 which was 3 times higher than bare ITO based devices[38].

In 2019, Dong et al investigated that the value of the dipole moment of SAMs is proportional to the modification of the work function of ITO. They used SAMs with different aromatic carboxylic acids, benzoic acid (BA), cyclohexane carboxylic acid (CHCA), 2-naphthoic acid (NA) ,4-biphenylcarboxylic acid (BCA) and 9*H*-carbazole-2-carboxylic acid (CzCA). In devices with structure ITO/SAMs/α-naphthyphenylbiphenyldiamine (NPB) (25 nm)/tris(8-hydroxyquindino) aluminium (III)

(Alq$_3$) (60 nm)/LiF (1 nm)/Al (100 nm), they achieved maximum luminance of 30,418 cd/m^2 with the SAM CzCA which is 3.6 times higher than the unmodified devices [39].

Figure 13 shows different SAMs used applied in LEDs in above literature.
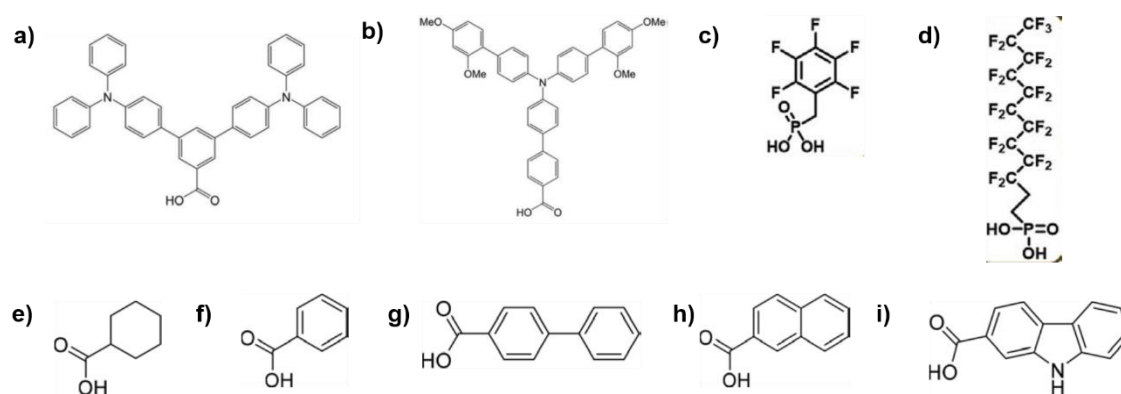
Figure 12 a) TPA b) MC-43 c) F5BPA d) HF21DPA e) CHCA f) BA g) BCA h) NA i) C$_z$CA

1.3 Quantum dots: Introduction

Quantum dots are nanometer sized typically of 2-20 nm materials containing 100 to 1000 atoms which shows quantum confinement effect because their size generally is comparable to the wavelength of electron.

The optoelectronic properties of quantum dots are directly related to their size and can be further manipulated by changing their size and shape and are different from their bulk form. The smaller the particles are, the smaller wavelength it will emit under UV radiation. We can say that the size is inversely proportional to their bandgap thus, the absorption and luminescence spectrum are redshifted with the increase in size.

Bulk semiconductors are crystalline or amorphous, whereas quantum dots can be molded in to 2D sheets or 3D arrays. Quantum dots having large surface to volume ratio helps to absorb more solar spectrum which are good for solar cells while their high color purity, low defect densities, high photoluminescence quantum yield and narrow FWHM are useful for LED application.
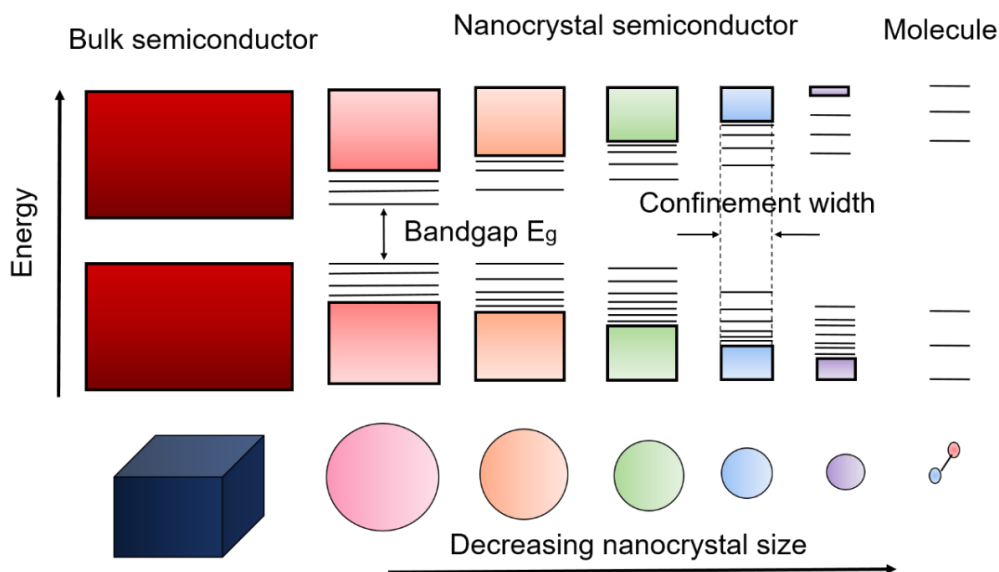
Figure 13. Quantum confinement effect.

1.3.1 CdSe based Quantum dots

Cadmium based quantum dots have vastly been investigated and applied in various applications from biomedical to optoelectronics. They are very luminescent nanomaterials with high PLQY. These nanoparticles are stable and mostly prepared by hot injection method which was first reported by Murray et al in 1933[40]. The synthesis was done with metal chalcogenide precursor with organic ligands to prevent the aggregation. The reaction takes place into an inert atmosphere at the high temperature of 300 ^{0}C to promote crystal formation. CdS, CdSe, and CdTe quantum dots are cadmium-based quantum dots which are commercially used in various applications[41].
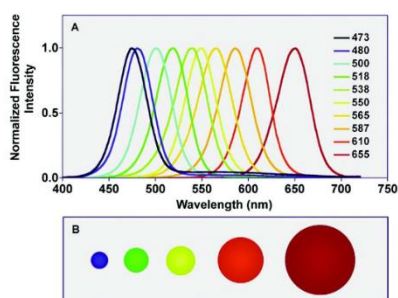
Figure 14 Size dependence of light emission of nanoparticles.[42]

The properties of quantum dots can be varied with the variation of their size. The size and the colour of quantum dots are dependent upon the reaction time and temperature.

Inspite of their several advantages, cadmium selenide quantum dots are prone to oxidize and forming traps (i.e., gap in the semiconductors which hinders the movements of charge carriers). To overcome this issue, researchers investigated to form inorganic layer on the top of the core quantum dots which are called core/shell structures of quantum dots or core/shell heterostructures. The emission can be tuned by changing the size of core and shell of the quantum dot structures [43].
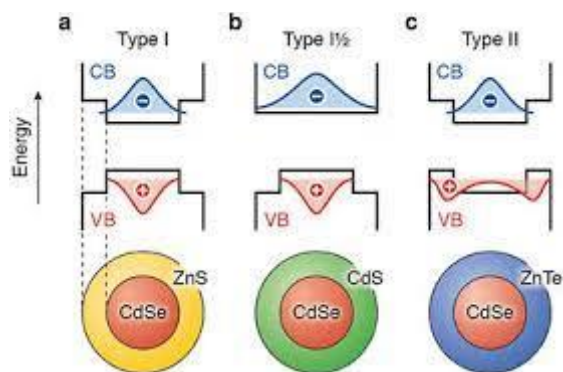
Figure 15 Different Core/shell heterostructures[43]

Among hetero-structured quantum dots, there are two types depending upon where the charge carries lies in core or distributed between the core and shell. In quantum dots CdSe@ZnS, the electron and holes are confined only in the core while in other core shell structures, electron and holes are confined in core and the shell respectively like in CdSe@CdS and CdSe@CdTe.

In this thesis, we have used CdSe@ZnS red quantum dots for applying them in fabricating light emitting diodes.
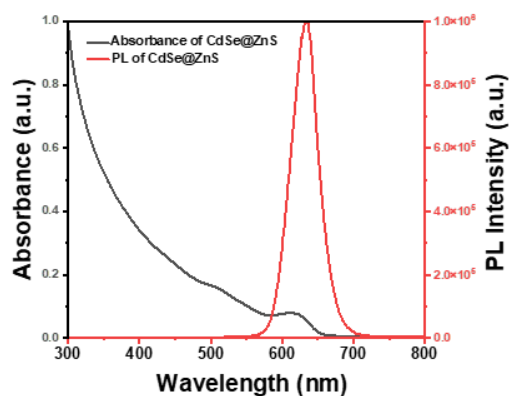
Figure 16 Absorption and PL spectra of CdSe@ZnS quantum dots.

1.3.2 Perovskite quantum dots

The perovskite material having the structure of perovskite mineral Calcium Titanite ($CaTiO_3$) was first discovered in 1839, by the German mineralogist, Gustav Rose (1798–1873) in Russian Ural Mountains. This material was named after the Russian mineralogist L.A Perovskii (1792–1856). The oxide perovskites were first brought in to popularity for their properties like high-temperature superconductivity, catalytic properties, magnetocaloric effect, and ferroelectricity. The research progress for the perovskite among researcher for their vast range of different applications.

Metal Halide perovskites (MHPs) have the general formula of (ABX_3) where A is a monovalent cation, B is divalent cation and X is monovalent halogen anion. They have attracted huge attention over recent years for their application in photovoltaic technologies like solar cells, Light emitting diodes, Photodetectors and LASERs. Perovskite materials possessing outstanding properties like low-cost preparation with cheap and earth abundant materials, low temperature synthesis, large diffusion length, low excitonic binding energy, high absorption coefficient and charge carrier mobility, tuning of emission wavelength and the band gap over entire visible region makes them the potential candidate for the above applications.

The Crystalline structure of Halide and Oxide perovskite materials are as follows-
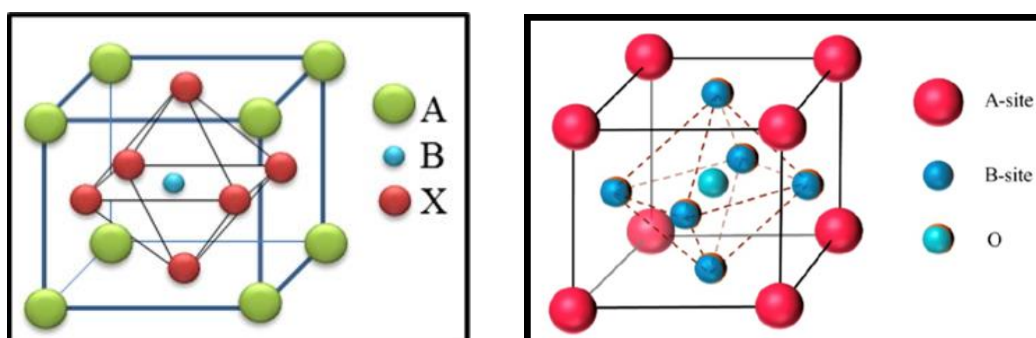
Figure 17 structure of General a) Halide Perovskite and b) Oxide Perovskite material[44].

In this thesis, we have used $CsPbBr_3$ perovskite quantum dots because of their higher color purities in comparison to the films. Depending upon the constituents, Halide perovskite quantum dots are hybrid Organic- Inorganic materials or all Inorganic. Report suggests that all inorganic perovskite quantum dots with Cesium monovalent anion are more stable than the hybrid perovskites with the same as Methylammonium (MA),

Formamidinium (FA), Octyammonium (OA)[45]. In the present thesis, we have worked with all Inorganic perovskite quantum dots.

1.3.3 Synthesis methods of Perovskite quantum dots

There are different methods to synthesize the perovskite quantum dots which can be classified as per the following flowchart-
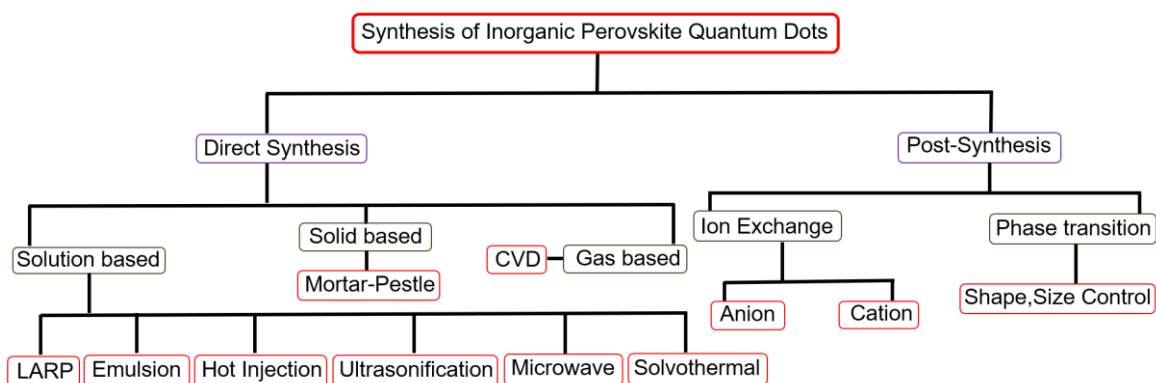
Figure 18 Classification of synthesis methods of Perovskite quantum dots

1. **Ligand-assisted precipitation Technique (LARP)-** In this method, the precursor solution is prepared in the nitrogen atmosphere for desired perovskite material. On the other hand, a vial with the solvent with 10 μl of ligand (e.g., oleic acid) were dissolved and kept at vigorous stirring in glove box. Then the prepared precursor is dropped into the solvent at definite intervals of few minutes until a 100 μl. Precursor solution breaks into its ingredient ions and forms perovskite Nanocrystals into the solution which is visible by the change of color of the solution and can be confirmed by exposing them into the UV light [46].
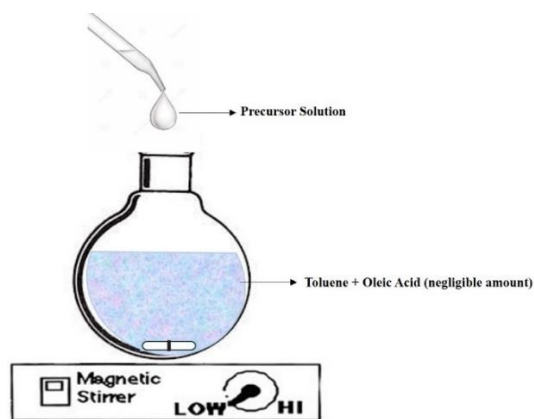
Figure 19 Schematic diagram for the synthesis of Perovskite Nanocrystal by LARP Technique

2. **Hot Injection Method-** In this thesis, we have used the hot injection method to prepare our cesium lead bromide ($CsPbBr_3$) nanocrystals. This method is commonly used for synthesis of perovskite as well as CdSe based quantum dots of various colors. The whole reaction takes place on the Schlenk line. All the materials used degassed in the inert atmosphere in nitrogen. Then, the Precursor is prepared in a flask by dissolving the cesium halide salt with the solvent and ligand at a definite and required amount. On the other hand, Lead halide salt is dissolved with the solvent and the ligands at an appropriate amount under the vacuum condition at rigorous stirring.

After the lead halide salt is completely dissolved, the flask is set to the reaction temperature. Meanwhile, an ice-water bath is prepared. Once the solution reaches the desired temperature, a definite amount of pre-heated precursor is injected quickly into the solution where the reaction happens to form the bright quantum dots. After 5 sec, the quantum-dot solution is placed into the ice-water bath to quench particles to prevent from growing any further.

The quantum dots can be washed by adding the solvent a few times and centrifuging to collect the precipitated quantum dots for further use [47].
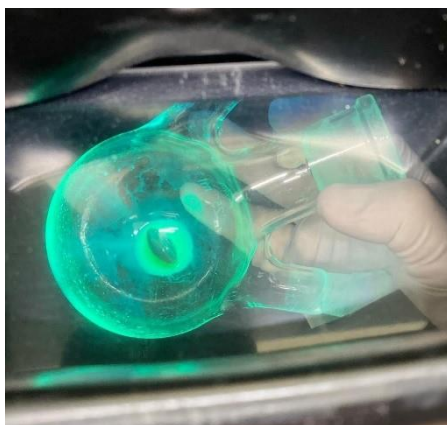
Figure 20 . Reaction flask under UV light after CsPbBr$_3$ QDs Synthesis at ICIQ.

3. **Emulsion Method-** In this method both the emulsification and demuslification are involved. MAPbX$_3$ is unstable in most of the polar solvents by inducing the PL quenching and sometimes destroying the QDs. To overcome that issue, Huan et al in 2015 used two immiscible solvents (DMF and n-hexane to form a non-aqueous emulsion which separates the two liquids at microscopic level.

   Further, the addition of demulsifer initiates the solvent mixing and induces the crystallization process. They were able to synthesize the size tunable QDs ranging from 2-8 nm by controlling the emulsion and demulsion process obtaining PLQY of 80-92% [48].

4. **Ultra sonification-** Tong et al in 2016, investigated the tip sonification method to produce the inorganic CsPbX$_3$ perovskite quantum dots. They mixed the corresponding precursor salts first, (Cs$_2$CO$_3$ and PbX$_2$ with the capping ligands (Oleylamine and oleic acid) in a non-polar solvent (Octadecene) in ambient atmosphere. The sonication process induced the cesium-oleate complex which is soluble in non-polar solvent and which then in the presence of ligands reacts with PbX$_2$ to form the colloidal CsPbX$_3$ quantum dots [49].

5. **Microwave-** Pan et al in 2017 used for the first time the microwave high-rate heating method to synthesize the CsPbX$_3$ perovskite nanocrystals. They obtained cubic sized uniform CsPbX$_3$ of high PLQY of 75% with a simpler method where cesium acetate (CsOAc), Lead Halide (PbX$_2$), a definite amount of trioctylphosphine oxide (TOPO), oleic acid (OA), Oleylamine (OAm), and 1-octadecene (ODE) were mixed in a microwave quartz tube in a microwave

reactor. The reactor was then heated at a certain rate to reach a certain reaction temperature by keeping it for 5 min followed by cleaning the crude QD solution twice by hexane solvent [50].

6. **Solvothermal-** This method is relatively simpler because of the simple set up, precise control over the morphology and high crystallinity of the product. Typically, the solvothermal process is conducted in an autoclave of stainless steel and maintaining a definite temperature and mixing the precursor altogether. Chen et al in 2017[51], prepared fully inorganic perovskite nanocrystals ($CsPbX_3$) by solvothermal method which is very well-known from some decades to prepare different type of nanocrystals.

   To prepare the perovskites, they mixed cesium acetate (CsOAc) and lead halide (PbX_2) with 1-ODE, OA and OAm at a certain amount and heat it at 160^0C and maintained the temperature for 30 min followed by washing the solution with hexane [51].

7. **Anion Exchange-** This is a unique method of synthesizing the mixed halide perovskite quantum dots by some specific treatments on the previously synthesized lead halide perovskite QDs, which can be done by several methods. Some of them are raising assisted synthesis method [52] and the microfluidic method [53] to achieve the mixed halide based PSKQDs.
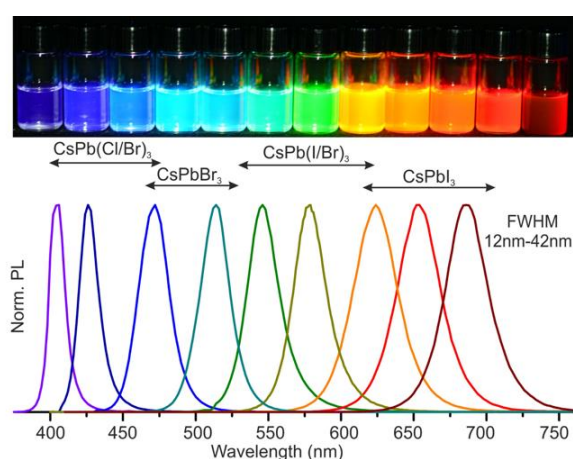
Figure 21 Visible spectral range perovskite emitters[47]

8. **Cation Exchange-** M. Hao et al. in 2020 have synthesized the mixed cation halide perovskite quantum dots with the solid-state A-site cation exchange strategy. They have combined the $CsPbI_3$ and $FAPbI_3$ layers to form a multinary

perovskite quantum dot layer [54]. In 2020, Hao et al. has used ligand-assisted cation exchange for preparing $Cs_{1-x}FA_xPbI_3$ quantum dots [55].
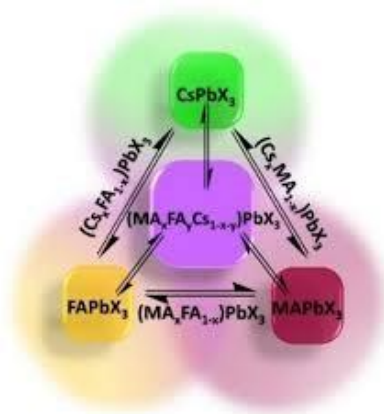
Figure 22 Cation exchange illustration in lead halide perovskites[56].

9. **Shape and Size Control-** As discussed above, the quantum dots band gap is dependent on their size, hence their optical properties. In halide perovskites, it is easy to alter their bandgap by varying the halide anion and control the properties and the band gap according to our desire. Peng et al in 2016 used a simple surfactant-assisted reprecipitation technique to play with the size of the PSK QDs. They have prepared the $MAPbCl_{3-x}Br_x$ and $MAPbBr_xI_{3-x}$ (x=1～3) by tuning the molar ratios of PbX_2 salts [57].

1.3.4 Efforts to improve the PSK QDs efficiency

For the emergence of perovskite nanoparticles applications, researchers have adapted several ways to improve the quality of the perovskite quantum dots by improving their photoluminescence quantum yield (PLQY) and also optimizing their size. In this thesis we have used hot injection method for the synthesis of our Cesium lead bromide nanocrystals QDs. The selected ligands were Oleic acid and Oleylamine followed by a post synthesis treatment with DDAB.

In 2016, Emre et al investigated that during the purification process of the perovskite quantum dots with polar solvents, the PSK QDs suffer degradation because of the proton exchange between oleic acid and Oleylamine. To address this issue, they have increased the colloidal stability by simply using tetraoctylammonium halides (TOAX) in

the preparation of OA-capped $CsPbX_3$ PQDs reaching PLQY of up to 70% improving the performance of LEDs [58].

In the same year Jun Pan et al investigated that the small chain ligand di-dodecyl dimethyl ammonium bromide (DDAB) facilitated better charge carrier transport between the Quantum dots. They used a ligand-exchange method to desorb OA to attach the DDAB to the $CsPbBr_3$ QDs which enabled the enhancement of performance of PeLEDs [59].

Chang et al in 2017 investigated a method called ligand post treatment to enhance the stability of $CsPbI_3$ quantum dots by treating the QDs with trioctylphosphine (TOP). The treated quantum dots persisted in its PLQY even after a month when optical properties remained the same after a few weeks [60].

Danila et al in 2018 reported a protocol to manage the surface chemistry of $CsPbBr_3$ quantum dots resulting in the PLQY of almost unity. They demonstrated that ligand binding affinity and ligand-to-NC molar ratio are the most important factors to control in order to achieve thermodynamically stable coordination which leads to excellent passivation. Post-synthesis addition of amines (and their conjugated acids) with different binding affinities were used for the NC surface [61].

In 2019, Jigeon et al investigated how to increase the electronic coupling within the $CsPbI_3$-PQD solids. They replaced the long-chained ligand oleic acid with the short chain ligand ions by using a post synthesis treatment of ligand exchange by sodium acetate (NaOAc) salt in MeOH solution [62].

Fang Chen et al in 2019 reported a passivation method of $CsPbBr_3$ nanocrystals with ammonium thiocyanate solution (SCN) followed by purification with ethyl acetate (EA) and re-dispersed with polar solvent hexane. SCN-treated NCs increased the performance of green PeLEDs with better stability of NCs in the devices [63].

Jun Pan et al in 2018 passivated their red $CsPBrI_3$ quantum dots with a post-synthesis treatment with bidentate ligand, namely 2,2′-iminodibenzoic acid (IDA) and observed a narrow photoluminescence with PLQY close to unity. They reported that the PL of untreated NCs was quenched after 5 days while, for the IDA treated NCs, their PL emission persisted even after 15 days. Also, the untreated NCs degrade into PbI_2 while the treated NCs show no phase transition after 40 days [64].

Chao et al in 2019 demonstrated a complete passivation method of $CsPbBr_3$ quantum dots with two ligands di-dodecyl dimethylammonium bromide (DDAB) and sodium thiocyanate (NaSCN) to achieve a stable PLQY of near unity. They have decreased the

surface defects of the QDs by passivating them with Br⁻ and SCN⁻ from the ligands to increase their stability. By this passivation strategy, they were able to achieve higher luminance and decreased the turn-on voltage in the PeLEDs [65].

Several reports claim that the optical properties of lead halide nanocrystals, their color purity, and stability depend critically on their surface passivation. In 2020 Palvasha et al studied the temperature dependent PL decay in $APbBr_3$ (A = Cs, MA, or FA) NCs with several different NC sizes, and surface passivating ligands. They found that, by increasing the temperature of NCs, there is no phase transition, and their PL lifetime decreases when decreasing temperature.

Surface passivation of NCs affects the temperature dependence of the PL and the PL lifetime. They observed in their study that the PL red shift is dominant in the large size of NCs, but emission spectral shape and lifetime dynamics does not depend upon NCs size [66].

In 2020 Kul et al demonstrated the use of chelating agents to increase PLQY and to control $CsPbBr_3$ QW distribution. They have incorporated γ-aminobutyric acid in the precursor solutions to passivate surfaces and electronic traps which destabilize the Pb sites to control the quantum well thickness distribution. The γ-aminobutyric acid incorporated $CsPbBr_3$ QDs yields blue LEDs which are more stable [67].

The above reports suggest that ligand passivation is one popular strategy to improve the stability and the optical properties of the QDs. In the same field, more efforts are dedicated to replacing the commonly used long-chained ligand OLA and OA to reduce the electrical insulativity among the QDs in colloidal solution and the films. In 2020, Qian et al conducted ligand engineering to replace Oleylamine (OAm) to Octylamine (OLA) in the synthesis of $CsPbBr_3$ Quantum dots to increase the PLQY from 61% to 92%. They spotted no aggregation in OLA treated QDs within 100 days of exposing them into the air. On the other hand, they observed a stable PL intensity to 97% even after 5 weeks [68].

Several works have been dedicated towards achieving higher PLQY for the PSK QDs (synthesized with hot-injection method) from different passivation techniques in the literature above. In 2020, Sujeong Jung et al were able to increase the PLQY by doping with trivalent dopant (In, Sb, and Bi) in their $CsPbBr_3$ QDs synthesized by LARP technique. They showed that the optimal doping concentration enhances lifetime of QDs while stability has increased over 10 days [69].

1.4 Application of QDs in LEDs

QD-LED is the class of display which uses electroluminescence of QDs. Since decades, it has become very popular among researchers and industries because of their outstanding properties like high efficiency, employment in flexible substrates, thin display and solution processability[70].

1.4.1 Application of CdSe QDs in LEDs

CdSe based colloidal QDs were first applied for LEDs in 1994, the seminal work was reported in Nature by Covlin et al with EQE of 0.01%[71] which was also the first QD-LED. Since then, the EQE has been increased upto 30.9% reported by Song et al in 2019[72] for red CdSe QDs based LEDs, 28.7% and 21.9% for green and blue QDLEDs respectively[73]. CdSe QDs based LEDs also have been successfully demonstrated as transparent[74], flexible[75] and wearable electronics[76].

1.4.2 Application of perovskite quantum dots in LEDs

Since 2009 after the first report of perovskite solar cell with the PCE of 3%, research has been focused on the field and the PCE till date (April 2023) has increased up to 33.3% with perovskite/silicon tandem Solar cells by the researchers from KAUST (the researchers have not revealed the details of research yet[77]) and which is comparable to the conventional silicon solar cells. The first report of perovskite materials on LED application came in 2014 with the external quantum efficiency of 0.1% [78]. Since then, the research on perovskite-based LEDs has been rapidly increased and the maximum EQE achieved over the past 8 years has increased up to 28.6% [79] which is comparable to CdSe based quantum dot LEDs [72].

In 2019, Wanqing et al have reported that by adding Poly(2-methyl-2-oxazoline) [PMOXA] in the $CsPbBr_3$ perovskite film have increased the photoluminescence of the films and also increased the performance of the LEDs in comparison to the devices with pristine films. In addition, they have achieved 2.5 hours of operational half-lifetime at initial luminance of 1000 cd/m^2 in the device structure ITO/PEDOT: PSS/PMOXA/$CsPbBr_3$/TPBi/LiF/Al [80].

1.4.3 Shortcomings in perovskite LEDs

Despite all the advantages of perovskite-based LEDs over CdSe based QDLEDs, there are several other issues that hinder the commercialization of PeLEDs. Efficiency roll-off at high current density; which is larger than 50% in most PeLEDs[81], lesser EQE for blue PeLEDs; despite of reaching high EQE of more than 28%, EQE of blue PeLEDs still lag behind. In 2021, Zhu et al investigate sky-blue LEDs with 13.8% at 496 nm[82]. And operational stability which plays an important role to make the device structure efficient overall. To address the issue of stability in perovskite LEDs, there are several internal and external factors that affect the PeLEDs stability. The external factors include Humidity, Temperature and Light, where the main internal factors are as follows-

1. Joule heating causes the charge carrier imbalance between the hole and the electrons.
2. The anion decompositions within the halide perovskite while the device is in operation.
3. Defect engineering, stable perovskite structures.

1.5 Doping in perovskites and its advantages in LEDs

Inspite of all the advantages with perovskite materials in LEDs, devices operational stability (due to ion migration most importantly and intrinsic phase instability) still lag behind the OLEDs which further limits them from practical use. For that, researchers have reported several ways to play with perovskite dimension, making devices with mixed halide anion and mixed cations, B-site doping with different elements.

Various reports suggest that the partial doping of B-site cation can reduce the defect density and hence reduced ion migration turns to increased operational stability of PeLEDs. Monovalent (K^+, Rb^+) [83], divalent (Mn^{2+}, Zn^{2+}, Cd^{2+}, Co^{2+}, Cu^{2+}, Sr^{2+}, Sn^{2+}, Ni^{2+}, Ge^{2+}) [84] and trivalent (Sb^{3+}, Bi^{3+}, Al^{3+}, Y^{3+}) [85] and lanthanide cations (Ce^{3+}, Tb^{3+}, Yb^{3+}) [86] were reported to improve the performance of MHPs in the perovskite LEDs.

In recent years, Lanthanide Rare earth (RE) ions doped perovskites have the attention for their potential application in photovoltaics and light emitting diodes [87]. Zhou et al in 2017 reported that the thermal stability and optical performance of Mn^{+2} doped $CsPbX_3$ perovskite nanocrystal has improved which are an efficient candidate for the LED application [88]. After few months Pan et al published a report where they have doped

CsPbCl$_3$ nanocrystals with different lanthanide ions (Ce^{3+}, Sm^{3+}, Eu^{3+}, Tb^{3+}, Dy^{3+}, Er^{3+}, and Yb^{3+}) and found the increased Photo luminescence quantum yield (PLQY) with expanding the emission from visible region to NIR spectral region. They suggested that the lanthanide doped perovskites can play an important role with good magnetic and electric properties [89].

In this thesis, we have fabricated PeLEDs with MAPbBr$_3$ perovskite as emissive material with different doping concentration of Dysprosium and compared the luminance with that of without any doping. Our aim was to understand the effects of Doping of this element in our PeLEDs. Figure 23 shows the PL spectra of MAPbBr$_3$ perovskite with and without doping with Dy.
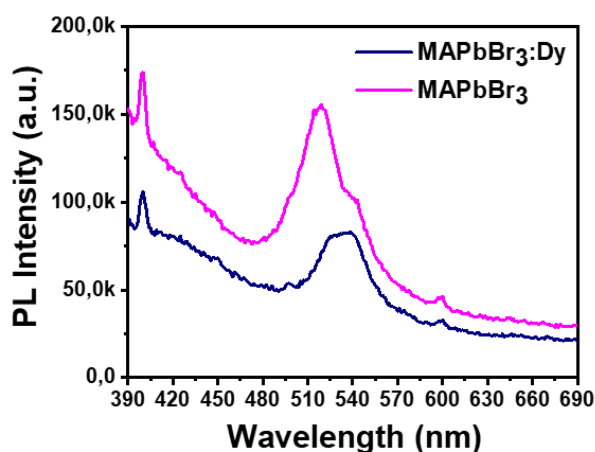
Figure 23 PL Spectra of MAPbBr$_3$ films before and after the doping of Dy

1.6 Application of Transparent QDLEDs

To make the fabrication of devices easier and cheaper, the device research has leaned towards the fully solution processes where the other thin film deposition methods like thermal evaporation, sputtering atomic layer deposition can be replace by the methods like spin-coating, slot-die etc. On the other hand, to scale-up the device fabrication can be difficult if it includes the deposition techniques like thermal evaporation. ITO has been widely used as a transparent conductive electrode in LEDs application but suffers with the problems like high-cost fabrication of devices, scarcity and brittleness, which arises the need to investigate other materials. There arises the need for the materials that can replace ITO like graphene, carbon nanotubes and the silver nanowires (AgNWs). Since past few years, AgNWs have demonstrated their potential among the thin films, which

has high electrical conductivity as well as the transparency; for the application as electrode in light emitting diodes, liquid crystal displays and solar cells. AgNWs are widely used in flexible electronics as well because of their good electro-mechanical properties (bending and stress), stability and low-cost fabrication[90] .

In this thesis, we have tried to fabricate the QDLEDs with CdSe@ZnS QDs as emissive layer. Figure 24 shows the prepared device and red luminescent colour from our device.
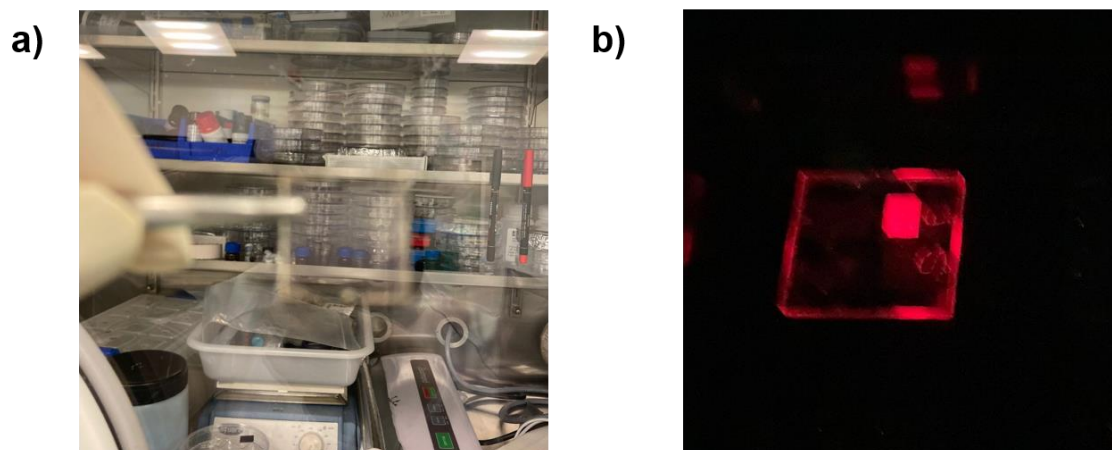
Figure 24 a) Transparent QDLEDs prepared at ICIQ with structure ITO/PEI/QDs/PVK/AgNWs b) Functional QDLED at underapplied bias

1.7 References

1.   Holonyak, N. & Bevacqua, S. F. Coherent (visible) light emission from Ga(As1-xPx) junctions. *Appl. Phys. Lett.* **1**, 82–83 (1962).

2.   Ruhstaller, B. *et al.* Advanced Numerical Simulation of Organic Light-emitting Devices. *Optoelectron. Devices Prop.* (2011) doi:10.5772/14626.

3.   George, W. & Bartosz, G. Self-Assembly at All Scales. *Sci.* **295**, 2418–2421 (2002).

4.   Kim, H. R., Jo, H. K., Hong, J. W., Park, S. G. & Kim, T. W. Performance enhancement of organic light-emitting diodes using fluorinated self-assembled monolayer. *Mol. Cryst. Liq. Cryst.* **653**, 151–156 (2017).

5.   Ono, S. *et al.* Effect of reactive self-assembled monolayer at the anode interface of organic light-emitting diode. *J. Nanosci. Nanotechnol.* **16**, 3407–3413 (2016).

6.   Matsushima, T., Kinoshita, Y. & Murata, H. Formation of Ohmic hole injection by inserting an ultrathin layer of molybdenum trioxide between indium tin oxide and organic hole-transporting layers. *Appl. Phys. Lett.* **91**, 10–13 (2007).

7.   Brewer, P. J. *et al.* Role of electron injection in polyfluorene-based light emitting diodes containing PEDOT:PSS. *Phys. Rev. B - Condens. Matter Mater. Phys.* **71**, 1–6 (2005).

8.   Li, C. N. *et al.* Improved performance of OLEDs with ITO surface treatments. *Thin Solid Films* **477**, 57–62 (2005).

9.   Lu, H. T. & Yokoyama, M. Plasma preparation on indium-tin-oxide anode surface for organic light emitting diodes. *J. Cryst. Growth* **260**, 186–190 (2004).

10.   Park, M. *et al.* MoS2-nanosheet/graphene-oxide composite hole injection layer in organic light-emitting diodes. *Electron. Mater. Lett.* **13**, 344–350 (2017).

11.   Helander, M. G. *et al.* Chlorinated indium tin oxide electrodes with high work function for organic device compatibility. *Science (6032).* **332**, 944–947 (2011).

12.   Sharma, A., Kippelen, B., Hotchkiss, P. J. & Marder, S. R. Stabilization of the work function of indium tin oxide using organic surface modifiers in organic light-emitting diodes. *Appl. Phys. Lett.* **93(16)**, (2008), 391.

13.   Zheng, H. *et al.* Self-assembled monolayer-modified ITO for efficient organic light-

emitting diodes: The impact of different self-assemble monolayers on interfacial and electroluminescent properties. *Org. Electron.* **56**, 89–95 (2018).

14. Casalini, S., Bortolotti, C. A., Leonardi, F. & Biscarini, F. Self-assembled monolayers in organic electronics. *Chem. Soc. Rev.* **46**, 40–71 (2017).

15. Scranton, A. B. , Kinney, A. B. Formation and Structure of. *Chem. Rev.* **i**, 1518–1520 (1994).

16. Gundlach, D. J., Nichols, J. A., Zhou, L. & Jackson, T. N. Thin-film transistors based on well-ordered thermally evaporated naphthacene films. *Appl. Phys. Lett.* **80**, 2925–2927 (2002).

17. Song, C. K. *et al.* 'Supersaturated' Self-Assembled Charge-Selective Interfacial Layers for Organic Solar Cells. *J. Am. Chem. Soc.* **136**, 17762–17773 (2014).

18. Yu, S. Y., Chang, J. H., Wang, P. S., Wu, C. I. & Tao, Y. T. Effect of ITO surface modification on the oled device lifetime. *Langmuir* **30**, 7369–7376 (2014).

19. Delgertsetseg, B. *et al.* Detailed investigation of dependencies of photovoltaic performances of P3HT:PC61BM based solar cells on anodic work function modified by surface treatment of indium-tin-oxide electrode with benzenesulfonyl chloride derivatives. *Org. Electron.* **23**, 164–170 (2015).

20. Can, M. *et al.* Electrical properties of SAM-modified ITO surface using aromatic small molecules with double bond carboxylic acid groups for OLED applications. *Appl. Surf. Sci.* **314**, 1082–1086 (2014).

21. Ranieri, A. *et al.* PH and solvent H/D isotope effects on the thermodynamics and kinetics of electron transfer for electrode-immobilized native and urea-unfolded stellacyanin. *Langmuir* **28**, 15087–15094 (2012).

22. Hoare, D. G. & Koshland, D. E. A method for the quantitative modification and estimation of carboxylic acid groups in proteins. *J. Biol. Chem.* **242**, 2447–2453 (1967).

23. Kim, S. & Yoo, H. Self-assembled monolayers: Versatile uses in electronic devices from gate dielectrics, dopants, and biosensing linkers. *Micromachines* **12(5)**, (2021), 565.

24. Cancino, J., Razzino, C. A., Zucolotto, V. & MacHado, S. A. S. The use of mixed self-assembled monolayers as a strategy to improve the efficiency of carbamate detection in environmental monitoring. *Electrochim. Acta* **87**, 717–723 (2013).

25. Wei, F., Zhong, T., Zhan, Z. & Yao, L. Self-assembled Micro-nanorobots: From Assembly Mechanisms to Applications. *ChemNanoMat* **7**, 238–252 (2021).

26. Chaki, N. K. & Vijayamohanan, K. Self-assembled monolayers as a tunable platform for biosensor applications. *Biosens. Bioelectron.* **17**, 1–12 (2002).

27. Hau, S. K. *et al.* Interfacial modification to improve inverted polymer solar cells. *J. Mater. Chem.* **18**, 5113–5119 (2008).

28. Lin, C. C. & Cho, C. P. Modified photoanodes by amino-containing phosphonate self-assembled monolayers to improve the efficiency of dye-sensitized solar cells. *RSC Adv.* **6**, 49702–49707 (2016).

29. Ali, F., Roldán-Carmona, C., Sohail, M. & Nazeeruddin, M. K. Applications of Self-Assembled Monolayers for Perovskite Solar Cells Interface Engineering to Address Efficiency and Stability. *Adv. Energy Mater.* **10**, 1–24 (2020).

30. Abrusci, A. *et al.* High-performance perovskite-polymer hybrid solar cells via electronic coupling with fullerene monolayers. *Nano Lett.* **13**, 3124–3128 (2013).

31. Yalcin, E. *et al.* Semiconductor self-assembled monolayers as selective contacts for efficient PiN perovskite solar cells. *Energy Environ. Sci.* **12**, 230–237 (2019).

32. Appleyard, S. F. J., Day, S. R., Pickford, R. D. & Willis, M. R. Organic electroluminescent devices: enhanced carrier injection using SAM derivatized ITO electrodes. *Journal of Materials Chemistry.* 10(1), 169–173 (2000).

33. Manna, U. *et al.* Enhanced carrier injection of organic light emitting devices using self assembled monolayer in the cathode/organic interface. *Thin Solid Films* **495**, 380–384 (2006).

34. Wang, M. & Hill, I. G. Fluorinated alkyl phosphonic acid SAMs replace PEDOT:PSS in polymer semiconductor devices. *Org. Electron.* **13**, 498–505 (2012).

35. Yalcin, E. *et al.* Functionalized organic semiconductor molecules to enhance charge carrier injection in electroluminescent cell. *Opt. Mater. (Amst).* **69**, 283–290 (2017).

36. Mori, T., Inden, T. & Nishikawa, T. Effect of alkyl chain length of fluorinated self-assemble monolayer to organic light-emitting diodes as a hole injection layer. *2016 Compd. Semicond. Week, CSW 2016 - Incl. 28th Int. Conf. Indium Phosphide Relat. Mater. IPRM 43rd Int. Symp. Compd. Semicond. ISCS 2016* 1–

2 (2016) doi:10.1109/ICIPRM.2016.7528816.

37. Park, S.-G. & Mori, T. Hole-Injection Properties Characteristics of Fluorinated Self-Assembled Monolayer on Polymeric and Organic Light-Emitting Diodes. *ECS J. Solid State Sci. Technol.* **6**, R53–R55 (2017).

38. Zheng, H. *et al.* Self-assembled monolayer-modified ITO for efficient organic light-emitting diodes: The impact of different self-assemble monolayers on interfacial and electroluminescent properties. *Org. Electron.* **56**, 89–95 (2018).

39. An, D., Liu, H., Wang, S. & Li, X. Modification of ITO anodes with self-assembled monolayers for enhancing hole injection in OLEDs. *Appl. Phys. Lett.* **114**, (2019).

40. Murray, C. B., Norris, D. J. & Bawendi, M. G. Synthesis and Characterization of Nearly Monodisperse CdE (E = S, Se, Te) Semiconductor Nanocrystallites. *J. Am. Chem. Soc.* **115**, 8706–8715 (1993).

41. Mo, D. *et al.* Cadmium-containing quantum dots: properties, applications, and toxicity. *Appl. Microbiol. Biotechnol.* **101**, 2713–2733 (2017).

42. Barzinjy, A. A., Salih, S. H., Sadraden, Z. A. & Qadir, H. M. Nanostructured Device in Sensing Applications: A Review. *Eurasian J. Sci. Eng.* **4**, (2018).

43. Rabouw, F. T. & de Mello Donega, C. Excited-State Dynamics in Colloidal Semiconductor Nanocrystals. *Top. Curr. Chem.* **374**, 1–30 (2016).

44. Almora, O., Vaillant-Roca, L. & Garcia-Belmonte, G. Perovskite Solar Cells: a Brief Introduction and Some Remarks Celdas Solares De Perovskitas: Una Breve Introducc on Y Algunas Consideraciones. *Rev. Cuba. Fis.* **34**, 58–68 (2017).

45. Kulbak, M. *et al.* Cesium Enhances Long-Term Stability of Lead Bromide Perovskite-Based Solar Cells. *J. Phys. Chem. Lett.* **7**, 167–172 (2016).

46. Zhang, F. *et al.* Brightly luminescent and color-tunable colloidal CH3NH3PbX3 (X = Br, I, Cl) quantum dots: Potential alternatives for display technology. *ACS Nano* **9**, 4533–4542 (2015).

47. Protesescu, L. *et al.* Nanocrystals of Cesium Lead Halide Perovskites (CsPbX3, X = Cl, Br, and I): Novel Optoelectronic Materials Showing Bright Emission with Wide Color Gamut. *Nano Lett.* **15**, 3692–3696 (2015).

48. Huang, H. *et al.* Emulsion Synthesis of Size-Tunable CH3NH3PbBr3 Quantum Dots: An Alternative Route toward Efficient Light-Emitting Diodes. *ACS Appl. Mater. Interfaces* **7**, 28128–28133 (2015).

49. Tong, Y. *et al.* Highly Luminescent Cesium Lead Halide Perovskite Nanocrystals with Tunable Composition and Thickness by Ultrasonication. *Angew. Chemie - Int. Ed.* **55**, 13887–13892 (2016).

50. Pan, Q. *et al.* Microwave-assisted synthesis of high-quality 'all-inorganic' CsPbX3 (X = Cl, Br, I) perovskite nanocrystals and their application in light emitting diodes. *J. Mater. Chem. C* **5**, 10947–10954 (2017).

51. Chen, M. *et al.* Solvothermal Synthesis of High-Quality All-Inorganic Cesium Lead Halide Perovskite Nanocrystals: From Nanocube to Ultrathin Nanowire. *Adv. Funct. Mater.* **27**, (2017).

52. Wang, C. *et al.* Full-visible-spectrum perovskite quantum dots by anion exchange resin assisted synthesis. *Nanophotonics* **11**, 1355–1366 (2022).

53. Lignos, I. *et al.* Synthesis of Cesium Lead Halide Perovskite Nanocrystals in a Droplet-Based Microfluidic Platform: Fast Parametric Space Mapping. *Nano Lett.* **16**, 1869–1877 (2016).

54. Park, S. Y. & Shim, H. C. Highly Efficient and Air-Stable Heterostructured Perovskite Quantum Dot Solar Cells Using a Solid-State Cation-Exchange Reaction. *ACS Appl. Mater. Interfaces* **12**, 57124–57133 (2020).

55. Hao, M. *et al.* Colloidal Cs. *Nat. Energy* 1–27 (2020).

56. Otero-Martínez, C. *et al.* Fast A-Site Cation Cross-Exchange at Room Temperature: Single-to Double- and Triple-Cation Halide Perovskite Nanocrystals. *Angew. Chemie - Int. Ed.* (2022) doi:10.1002/anie.202205617.

57. Peng, L., Tang, A., Yang, C. & Teng, F. Size-controlled synthesis of highly luminescent organometal halide perovskite quantum dots. *J. Alloys Compd.* **687**, 506–513 (2016).

58. Yassitepe, E. *et al.* Amine-Free Synthesis of Cesium Lead Halide Perovskite Quantum Dots for Efficient Light-Emitting Diodes. *Adv. Funct. Mater.* **26**, 8757–8763 (2016).

59. Pan, J. *et al.* Highly Efficient Perovskite-Quantum-Dot Light-Emitting Diodes by Surface Engineering. *Adv. Mater.* **28**, 8718–8725 (2016).

60. Lu, C. *et al.* Enhanced stabilization of inorganic cesium lead triiodide (CsPbi3) perovskite quantum dots with tri-octylphosphine. *Nano Res.* **11**, 762–768 (2018).

61. Quarta, D. *et al.* Stable Ligand Coordination at the Surface of Colloidal CsPbBr3

Nanocrystals. *J. Phys. Chem. Lett.* **10**, 3715–3726 (2019).

62. Kim, J. *et al.* Alkali acetate-assisted enhanced electronic coupling in CsPbI3 perovskite quantum dot solids for improved photovoltaics. *Nano Energy* **66**, 104130 (2019).

63. Chen, F., Boopathi, K. M., Imran, M., Lauciello, S. & Salerno, M. Thiocyanate-treated perovskite-nanocrystal-based light-emitting diodes with insight in efficiency roll-off. *Materials (Basel).* **13(2)**, 367 (2020).

64. Pan, J. *et al.* Bidentate Ligand-Passivated CsPbI 3 Perovskite Nanocrystals for Stable Near-Unity Photoluminescence Quantum Yield and Efficient Red Light-Emitting Diodes. *J. Am. Chem. Soc.* **140**, 562–565 (2018).

65. Zheng, C., Bi, C., Huang, F., Binks, D. & Tian, J. Stable and Strong Emission CsPbBr3 Quantum Dots by Surface Engineering for High-Performance Optoelectronic Films. *ACS Appl. Mater. Interfaces* **11**, 25410–25416 (2019).

66. Ijaz, P. *et al.* Composition-, Size-, and Surface Functionalization-Dependent Optical Properties of Lead Bromide Perovskite Nanocrystals. *J. Phys. Chem. Lett.* **11**, 2079–2085 (2020).

67. Wang, Y. K. *et al.* Chelating-agent-assisted control of CsPbBr3 quantum well growth enables stable blue perovskite emitters. *Nat. Commun.* **11**, 1–7 (2020).

68. Xiong, Q. *et al.* Surface Ligand Engineering for CsPbBr3 Quantum Dots Aiming at Aggregation Suppression and Amplified Spontaneous Emission Improvement. *Adv. Opt. Mater.* **8**, 1–8 (2020).

69. Jung, S. *et al.* Enhancement of Photoluminescence Quantum Yield and Stability in CsPbBr3 Perovskite Quantum Dots by Trivalent Doping. *Nanomaterials* **10(4)**, 710 (2020).

70. Jang, E. & Jang, H. Review: Quantum Dot Light-Emitting Diodes. *Chem. Rev.* (2023) doi:10.1021/acs.chemrev.2c00695.

71. Colvin, V. L., Schlamp, M. C. & Alivisatos, A. P. Light-emitting diodes made from cadmium selenide nanocrystals and a semiconducting polymer. *Nature* **370**, 354–357 (1994).

72. Song, J. *et al.* Over 30% External Quantum Efficiency Light-Emitting Diodes by Engineering Quantum Dot-Assisted Energy Level Match for Hole Transport Layer. *Adv. Funct. Mater.* **29**, 1–9 (2019).

73. Deng, Y. *et al.* Solution-processed green and blue quantum-dot light-emitting diodes with eliminated charge leakage. *Nat. Photonics* **16**, 505–511 (2022).

74. Zhang, N., Ding, S., Wang, K., Lyu, Q. & Sun, W. X. Efficient transparent quantum-dot light-emitting diodes with an inverted architecture. *Opt. Mater. Express* **11**, 2145 (2021).

75. Choi, M. K., Yang, J., Hyeon, T. & Kim, D. H. Flexible quantum dot light-emitting diodes for next-generation displays. *npj Flex. Electron.* **2**, 1–14 (2018).

76. Lee, Y. *et al.* Stretchable array of CdSe/ZnS quantum-dot light emitting diodes for visual display of bio-signals. *Chem. Eng. J.* **427**, 130858 (2021).

77. Wang, R. *et al.* Recent progress on efficient perovskite/organic tandem solar cells. *J. Energy Chem.* **83**, 158–172 (2023).

78. Tan, Z.-K. *et al.* Bright light-emitting diodes based on organometal halide perovskite. *Nat. Nanotechnol.* **9**, 687–692 (2014).

79. Liu, Z. *et al.* Perovskite Light-Emitting Diodes with EQE Exceeding 28% through a Synergetic Dual-Additive Strategy for Defect Passivation and Nanostructure Regulation. *Adv. Mater.* **33**, 1–9 (2021).

80. Cai, W. *et al.* High-performance and stable CsPbBr3 light-emitting diodes based on polymer additive treatment. *RSC Adv.* **9**, 27684–27691 (2019).

81. Zhao, C., Zhang, D. & Qin, C. Perovskite light-emitting diodes. *CCS Chem.* **2**, 859–869 (2020).

82. Zhu, Z. *et al.* Highly Efficient Sky-Blue Perovskite Light-Emitting Diode Via Suppressing Nonradiative Energy Loss. *Chem. Mater.* **33**, 4154–4162 (2021).

83. Amgar, D., Binyamin, T., Uvarov, V. & Etgar, L. Near ultra-violet to mid-visible band gap tuning of mixed cation Rb: XCs1- xPbX3 (X = Cl or Br) perovskite nanoparticles. *Nanoscale* **10**, 6060–6068 (2018).

84. Van der Stam, W. *et al.* Highly Emissive Divalent-Ion-Doped Colloidal CsPb1-xMxBr3 Perovskite Nanocrystals through Cation Exchange. *J. Am. Chem. Soc.* **139**, 4087–4097 (2017).

85. Wang, Q. *et al.* Efficient sky-blue perovskite light-emitting diodes via photoluminescence enhancement. *Nat. Commun.* **10(1)**, 5633 (2019).

86. Yao, J. S. *et al.* Ce3+-Doping to Modulate Photoluminescence Kinetics for

Efficient CsPbBr3 Nanocrystals Based Light-Emitting Diodes. *J. Am. Chem. Soc.* **140**, 3626–3634 (2018).

87. Chen, Y. *et al.* An overview of rare earth coupled lead halide perovskite and its application in photovoltaics and light emitting devices. *Prog. Mater. Sci.* **120**, 100737 (2021).

88. Zou, S. *et al.* Stabilizing Cesium Lead Halide Perovskite Lattice through Mn(II) Substitution for Air-Stable Light-Emitting Diodes. *J. Am. Chem. Soc.* **139**, 11443–11450 (2017).

89. Pan, G. *et al.* Doping Lanthanide into Perovskite Nanocrystals: Highly Improved and Expanded Optical Properties. *Nano Lett.* **17**, 8005–8011 (2017).

90. Langley, D. P. *et al.* Silver nanowire networks: Physical properties and potential integration in solar cells. *Sol. Energy Mater. Sol. Cells* **125**, 318–324 (2014).

Chapter 2: Motivation and aims of the thesis

Since the first application of perovskites, the investigation about their various applications have exponentially increased. On the other hand, self-assembled monolayers have also been extensively applied at multidisciplinary stages. The first report on the properties of nanoparticles was written in 1857 by Michal Faraday about gold nanoparticles (Au NPs). The first report on doping of lead halide perovskites by rare earth elements was by Gencai Pan.

In the preparation of thesis, our focus was on studying the properties of self-assembled monolayers and applications; properties and synthesis of perovskite quantum dots; and the doping of bulk perovskite. All the materials were tested for fabrication of Perovskite Light Emitting Diodes/Quantum dot LEDs (QLEDs). We have synthesized two different types of quantum dots Core-shell CdSe@ZnS quantum dots and all inorganic $CsPbBr_3$ perovskite quantum dots.

This thesis is divided into seven chapters where three main chapters focused on the experiments carried out during the PhD. The research has been carried out at two institutions: Institute of Chemical Research of Catalonia (ICIQ) and Eurecat, the technological Centre of Catalonia, between March 2019 and March 2023.

In **Chapter 1**, We have overviewed the various types and applications of self-assembled monolayers a perovskite, general properties of quantum dots, synthesis methods, literature survey and the efforts for improvement of the perovskite quantum dots. In this chapter we have described also fundamental properties of LEDs and their working mechanism.

In **Chapter 3,** We have described the different film formation techniques used in our experiments. We have described the techniques used to characterize the

materials used in our experiments and the synthesis of the different materials used in our projects.

In **Chapter 4,** we have described the most commonly used HTMs for preparation of PeLEDs; PEDOT: PSS and PTAA polymers which show having good efficiencies in the devices but hinders the operational stability. Therefore, in order to constructing overall efficient PeLEDs, we have tried to investigate new HTMs for devices which not only shows good luminance but also enhances their operational stabilities in comparison to our reference devices which has PTAA as HTM.

Our HTMs consists of carbazole based self-assembled molecules EADR03 and EADR04 as hole transporting layer in the $CsPbBr_3$ nanocrystals-based light emitting diodes with normal structures. We have also shown the synthesis of the $CsPbBr_3$ perovskite nanocrystals with hot injection method as the active layer in our PeLEDs. This project was published in Journal of Materials Chemistry in 2023: **Kumari, S.**, Sánchez, J. G., Imran, M., Aktas, E., González, D. A., Manna, L., ... & Palomares, E. J. (2023). Self-Assembled Molecules as Selective Contacts in CsPbBr3 Nanocrystal Light Emitting Diodes. *Journal of Materials Chemistry C.* This project was completed at ICIQ Tarragona in collaboration with Prof. Liberato manna from Italian Institute of Technology.

In **Chapter 5,** we have studied the most commonly used ETLs in QDLEDs such as PEI and ZnO NPs, the insulating nature of PEI and the lesser EQE of ZnO NPs pushes the need to investigate other materials which are suitable ETMs for these devices. Therefore, in order to take a step for new materials for the QDLEDs, we have tried to employ PDINO [N, N'-Bis (N, N-dimethylpropan-1-amine oxide) perylene-3,4,9,10-tetracarboxylic diimide] molecule as the ETL in the inverted structured CdSe@ZnS quantum dot light emitting diodes. This molecule was already applied as an ETL for the application of organic solar cells.

The performance of devices with PDINO as ETL was compared to devices with PEI and PDINO/PEI as ETL. This project was done with the collaboration of Prof. Ivan Mora Sero from INAM (Institute of Advanced Materials) where a part of this research was also done during my two weeks of research stay.

In **Chapter 6,** we have studied that in order to improve the overall performance of PeLEDs, doping of perovskite material at B-cation is one of the strategies. Thus, we have tried to dope the Methyl Ammonium Bromide (MAPbBr$_3$) perovskite with a rare earth element Dy^{+3} and used as active material for fabricating our devices. We have done the doping at different concentrations to find optimum and compared the performance to the PeLEDs with un-doped perovskite-based devices.

In **Chapter 7,** we explain the general conclusion of all experiments performed during the development of thesis with future perspective.

Chapter 3: Experimental methods and techniques

Abstract

In this chapter we describe all the experimental techniques used to prepare or characterize the materials in the development of thesis. The facilities are situated mostly in ICIQ (Institut Català d'Investigació Química)https://www.iciq.org/ and Eurecat - Centre Tecnològic de Catalunya, unless otherwise indicated.

3.1 Introduction

In this chapter, the general information about material synthesis, characterization and device preparation are explained in a provident manner divided in the sections of material synthesis, material characterization, device assembly and device characterization.

3.2 Material Synthesis

3.2.1 General Reactants

The reactants which were used in our thesis for experiments are as follows-

ITO/glass substrates were purchased from Xinyan Technology Limited, water based PEDOT: PSS was purchased from Heraeus, TPBi was purchased from LumTec, LiF from Sigma-Aldrich, PTAA was purchased from Sigma-Aldrich. CdO, TOPO, ODPA, Sulphur and $Zn(ac)_2 \cdot H_2O$ were purchased from Strem chemicals, Sigma-Aldrich, PolyCarbon Industries INC, Acros and Sigma Aldrich. Whereas PDINO and PEI materials were purchased from 1-materials and Sigma Aldrich respectively. Dysprosium nitrate salt was purchased from Sigma Aldrich.

3.2.2 Synthesis of CsPbBr$_3$ Quantum dots

The synthesis follows the procedure reported by Protesescu et al.[1]Cesium oleate was prepared by dissolving 81.4 mg of cesium carbonate (Cs_2CO_3, Aldrich, 99.9%) into 4 mL of octadecene (ODE, Sigma-Aldrich, 90%) and 250 µl of oleic acid (OA, Sigma Aldrich, 90%) while degassing the solution with the help of Schlenk line under a vacuum of $5 \cdot 10^{-1}$ mbar at 80 ºC for 3 h with continuous stirring. Since cesium oleate precipitates out of ODE at room temperature, it was preheated to 100 ºC before injection. 345 mg of PbBr$_2$ in a three-neck flask, 25 mL of ODE, and two commonly used organic surface ligands, 2.5 mL of OA and 2.5 mL of Oleyl amine (OLA), were degassed in different flasks under the same conditions than cesium oleate. After degassing, ODE, OA and OLA were injected into the three-neck flask containing the lead bromide to dissolve it completely

under vacuum at 120 ºC with continuous vigorous stirring. After the complete dissolution of $PbBr_2$, the flask was slowly switched to N_2 atmosphere, and the temperature was increased to 170ºC. Once the desired temperature was achieved, 2 mL of cesium oleate precursor preheated at 170 ºC was injected swiftly into the solution resulting in yellowish-green solution that led to the formation of $CsPbBr_3$ nanocrystals. After 5 seconds, the solution was placed into an ice-water bath to stop further growth of the nanocrystals. Later, the crude solution was centrifuged at 4500 rpm for 10 min at 15 ºC, the supernatant was discarded, and 1.5 mL of toluene was added to the precipitate and centrifuged again. The as-prepared precipitate was dissolved in toluene with a concentration of 25 mg/mL for further use.

3.2.3 Synthesis of CdSeS@ZnS Quantum dots

CdSeS@Zns were prepared via hot injection reported in the bibliography[2]. In 10 mL three-neck flask equipped with a reflux condenser and heating mantel, 0.060 gr Cadmium Oxide (CdO), 0.224 gr of octadecyl phosphonic acid (ODPA) and 3 gr trioctylphospine oxide (TOPO) was mixed 150 ºC during 30 min under inert conditions. After that, the sample was heated up to 305 ºC. A solution of 0.27 mmol Se, 0.03 mmol S with 0.5 ml of trioctylphosphine was added quickly. The reaction was heated during 10 min. The quantum dots were precipitated with acetone and purified with a mixture of toluene/acetone (1:4).

For producing the ZnS shell, 172 mg of QDs were solved in 25 ml ODE and heated at 270 ºC under inert conditions. Then, a solution of 2.86 mmol $Zn(ac)_2 \cdot H_2O$, 4 ml OA and 1 ml ODE was added to a solution of 6.75 mmol of Sulphur with 3.5 mL of TOP. The reaction was maintained during 10 min at 270 ºC. The quantum dots were precipitated with acetone and purified with a mixture of toluene/acetone (1:4)

3.3 Material Characterization

To understand the structural and optical properties of our samples, we have divided this section into two parts which can be described below.

3.3.1 Optical Characterization

The optical characterization techniques which we have used in our thesis are as follows:

3.3.1.1 UV-VIS Spectroscopy

It is a molecular/quantitative technique to measure how a sample can absorb light with respect to blank or a reference sample along a certain range of wavelengths. The absorbed light gives the information about the functional group present and energy gap between HOMO and LUMO of the samples by exciting the electrons from ground energy level to higher energy levels (the excited state). The technique follows the Beer-Lamberts law, according to which the absorbance of the sample is directly proportional to the concentration of the sample and the path length.

$$A = \log_{10}(I_0/I) = \varepsilon cL$$

Where I_0 is the intensity of the incident light of the given wavelength, I is the intensity of transmitted light, L in cm is the path length through the sample, c in mol/L is the concentration of absorbing sample and A is absorbance in Absorbance Units (au).

A schematic diagram of a double beam spectrophotometer is shown in the following figure 25 to understand the basic principle of an UV-VIS spectrophotometer. Hydrogen discharge lamp/deuterium discharge lamp/mercury arc lamps are used as a source of desired electromagnetic (EM) radiation. Then the radiation goes to the wavelength selector which cuts off the polychromatic light to monochromatic with the help of gratings. Then the beam falls in a mirror from where the beam is reflected to the shutter splitting it into half. Further, half the beam is passed to the sample cuvettes and the other half is passed to the reference which should be transparent. As the beams pass through the cuvettes, the detectors are used to detect their intensities and send the beams to the amplifier where the signals are enhanced, and the result can be seen on the monitor. In our thesis, we have used SHIMADZU UV-2401PC spectrophotometer to characterize our samples.
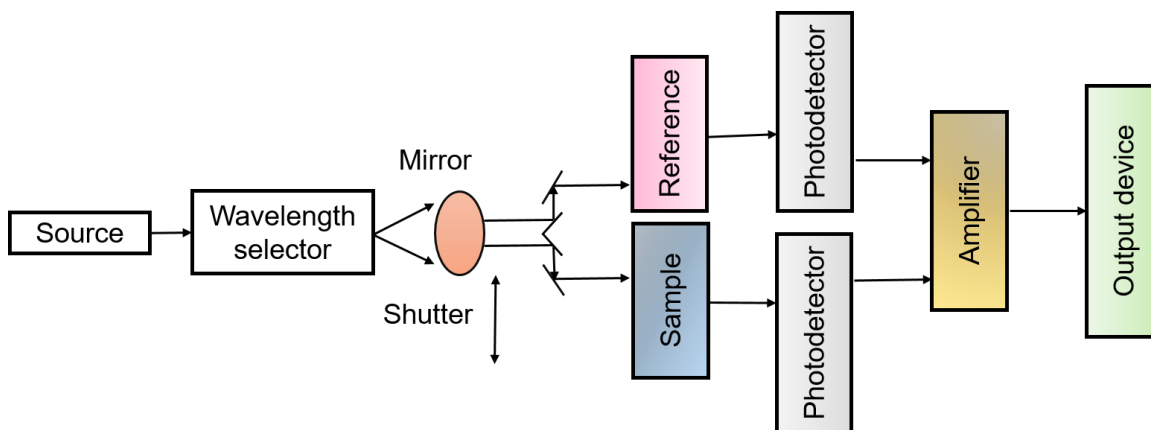
Figure 25 Scheme of the UV-VIS spectrometer

The same spectrophotometer can be used to analyze the transmittance apart from the absorbance of the sample. The transmittance of a sample can be calculated by the following relation-

$$A = \log_{10} (1/T)$$

Where T is transmittance, which is defined as the ratio of the light passes through a sample to the light incidents on a sample. Absorbing unit (a.u.) are proportional to the transmittance of a sample and can be related as follows-

1 a.u. = 10% of T

2 a.u. = 20% of T
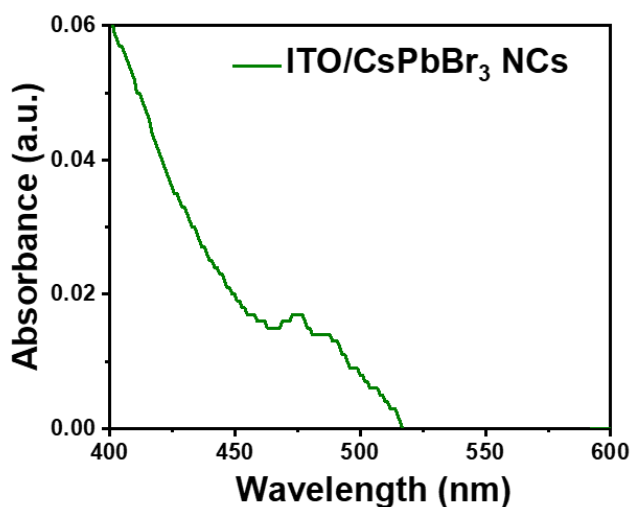
Figure 26 UV-VIS Spectra of ITO/CsPbBr$_3$ NCs film prepared during the thesis.

3.3.1.2 Photoluminescence Spectroscopy

It is a nondestructive contactless technique which can be used to determine the material quality, defect states, recombination mechanism of the charges and molecular structure. When the light is absorbed by the material, the electrons get photo-excited moving from the ground state to the excited state. After a certain time, they return to their original states by releasing the absorbed energy in the form of photons (radiative relaxation) or heat (non-radiative relaxation). The photoluminescence (PL) process is of two types of **fluorescence** and **phosphorescence**. After a certain time, when an electron relaxes back to ground energy state from the lowest excited state by emitting photons within a short time of 10^{-9} to 10^{-6} s, the process is called fluorescence. On the other hand, phosphorescence includes a metastable state for the electrons. In this process the electron relaxes from excited singlet state to the energetically favorable excited triplet state by inverting its spin within 10^{-11} to 10^{-6} s, followed by the delayed relaxation from higher triplet energy level to the ground singlet state within delayed time 10^{-3} to 100s.

The processes of absorbance, internal conversion, intersystem crossing, vibrational relaxation, and photoluminescence can be understood by the Jablonski diagram which is an energy diagram shown in Figure 27. The absorbance process is very fast of 10^{-15} seconds, it occurs when an electron absorbs the energy from the photon and excites it to a higher energy level. It happens only when the energy absorbed is equal to the difference between the two energy levels. Vibrational relaxation occurs as a fast process of 10^{-14} and 10^{-11} seconds. It is a non- radiative process where the energy is transformed to kinetic energy. On the other hand, if the excited electron can transition from a vibration level in one electronic state to the vibrational level of lower electronic state, the transition is called internal conversion which occurs because of the overlapping of vibrational and electronic levels. When an electron changes its spin-multiplicity from an excited singlet state to an excited triplet state, the method of dissipation of energy is called intersystem crossing. Which further leads to photoluminescence. In this thesis, we have used a Horiba Jobin Yvon Ltd with PMT and InGaAs detectors for characterizing the samples during the thesis. An example of PL spectra obtained during the thesis is shown in figure 28.
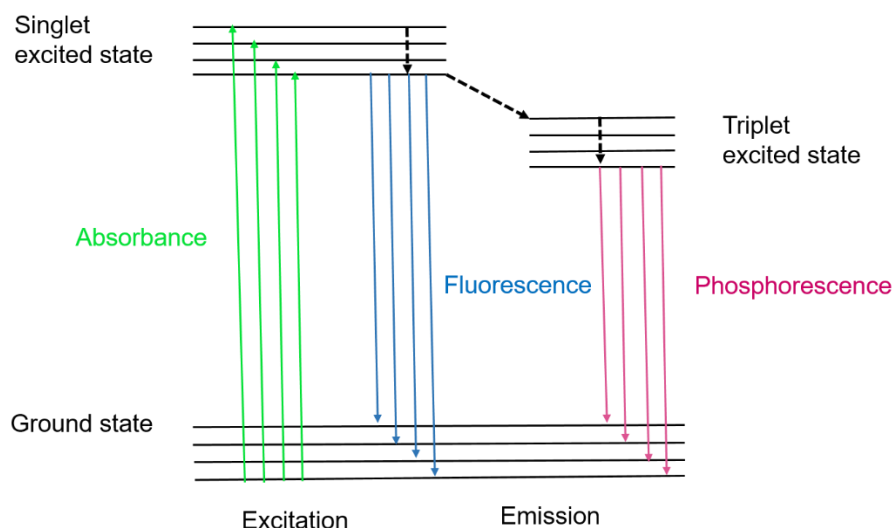
Figure 27. The Jablonski Diagram.
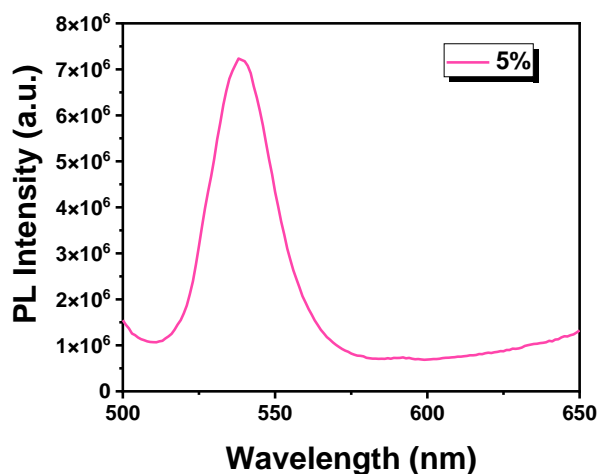
Figure 28. PL Spectra of MAPb$_{0.95}$Dy$_{0.5}$Br$_3$ film prepared during thesis.

3.3.1.3 Photoluminescence quantum yield

It is the measure of the fraction of the number of photons emitted to the number of photons absorbed. It can be calculated by two different methods a) the absolute photoluminescent quantum yield (PLQY), and b) comparatively. For the absolute PLQY calculation, the material is characterized with the help of integrated sphere, which is a direct method to calculate PLQY. Here, a sphere is used having all reflecting surface with materials like barium-sulphate to capture all the incoming and outgoing light from the surface. While, in our work, we have calculated the PLQY comparatively where the yield of our sample of interest is compared to another material (usually dye) with known PLQY value, with the help of equation 1.

Equation1

$$QY = QY\text{ref} \frac{(\text{Iem sample})}{(\text{Iem reference})} \frac{(\text{Abs reference})}{(\text{Abs sample})} \frac{(n \text{ sample})^2}{(n \text{ reference})^2}$$

Where, $I_{em\ sample}$ and $I_{em\ reference}$ are the area under the curve of PL spectra of sample and the reference dye used at a particular excitation wavelength (λ_{ext}). Abs_{sample} and $Abs_{reference}$ are the absorbance values of sample and references respectively at λ_{ext} from absorbance spectra. n_{sample} and $n_{reference}$ are the refractive index of the solvents used to dissolve the sample and reference dye respectively.

For the PLQY measurements, we have used a few different commercial dyes for different samples. The dyes have different quantum yields indicated below in table1.

Table 1. Characteristics of the Fluorophores solved in ethanol at room temperature.

Dye	QY_{ref} (%)	Excitation range (nm)	Emission range (nm)
C-102	0.764 (±0.039)	340-420	430-530
C-153	0.544 (±0.028)	360-470	485-635
Rh-101	0.913 (±0.046)	515-565	585-665

3.3.1.4 Time corelated single photon counting

This technique is used to determine the fluorescence lifetimes. A short laser pulse of a particular frequency as a reference signal is applied to the sample and the single photons and their arrival times are being detected. The fluorescence lifetime was recorded by using an Edinburgh Instruments LifeSpec II spectrometer based on the time-correlated single photon counting technique (TCSPC), equipped with PMT detectors, double subtractive monochromator, and picosecond pulsed diode lasers sources. The working scheme of a general spectrometer is illustrated in figure 29.
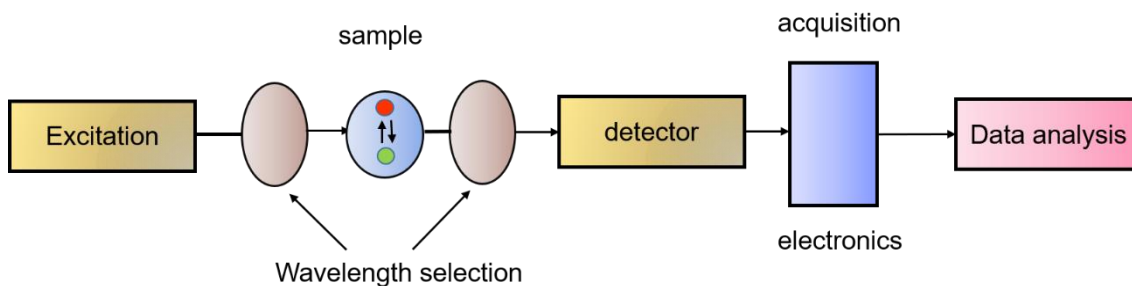
Figure 29. Schematic description of the TCSPC mechanism.

Figure 30 shows the single photon counting measurement for the CsPbBr$_3$ nanocrystals prepared during the thesis. The signal is fitted by exponential equations (see Equation 2) that permit to estimate the decay lifetime of the different processes. Where PL(t) shows the total PL decay lifetime value, A1 and A2 are the amplitudes of radiative decay lifetimes and where $\tau 1$ and $\tau 2$ are lifetimes decay of two radiative decay processes while t is the constant.

$$PL(t) = A1e - (t/\tau 1) + A2e - (t/\tau 2) \qquad \text{Equation 2}$$
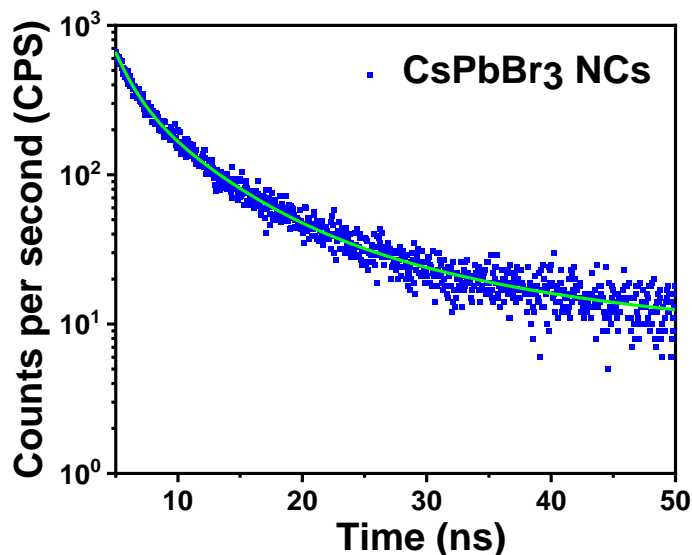
Figure 30. Example of a lifetime decay curve of CsPbBr$_3$ NCs prepared during thesis.

3.3.2 Structural Characterization

3.3.2.1 X ray diffraction

It is a non-destructive technique used to identify the crystal structure of the materials including orientation of grains or single crystals, crystallite size, lattice parameters, arrangement patterns of the crystals and ratio of crystal to amorphous regions within the crystalline solids. When an X ray beam falls on a crystalline sample, its interferences many times due to the atomic planes of the crystal while passing through it. Sir W.H. Bragg and W.L Bragg developed a relation to study the diffraction patterns which resulted in the Bragg´s law. According to this law, when a monochromatic X-Ray of wavelength λ falls upon atomic planes at an angle θ, it gets reflected and gives constructive interference. When the path difference of two rays is equal to the multiple of λ, it satisfies the equation $2d\sin\theta=n\lambda$ where n is the multiple number and d is the interplanar spacing. Diffraction occurs when the above equation satisfies the Bragg´s law that can be explained with the following figure 31.

Incident beam   Reflected plane

Upper plane

Lower plane
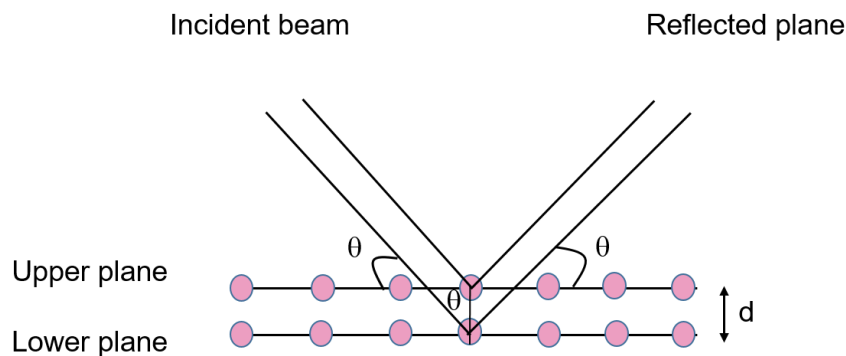
Figure 31. Schematic description of the Bragg´s Law.

3.3.2.2 Transmission Electron Microscopy

It is a microscopic technique which provides topological, morphological, compositional, and structural information like dislocations and grain boundaries in the samples. It produces high resolution black and white images of the samples when the beam of high energy electrons penetrates through the thin sample. The transmission electron microscopy (TEM) functions at the same basic principle as optical microscope but photons are replaced by electron beam and the glass lenses replaced by

electromagnetic lenses. We have used JEOL 1011 microscope in our thesis to study the morphology of the CsPbBr$_3$ Quantum dots are shown in the following figure 32.
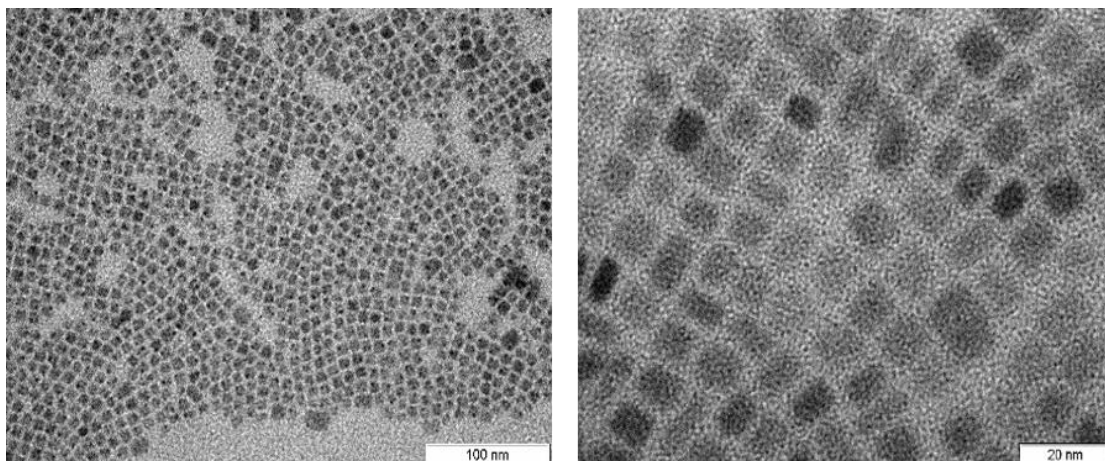
Figure 32. TEM images of CsPbBr$_3$ Quantum dots.

The histogram, shown in figure 33 below, obtained from the above pictures describes the average size of 50 different quantum dots which is 7.5 nm in diameter.
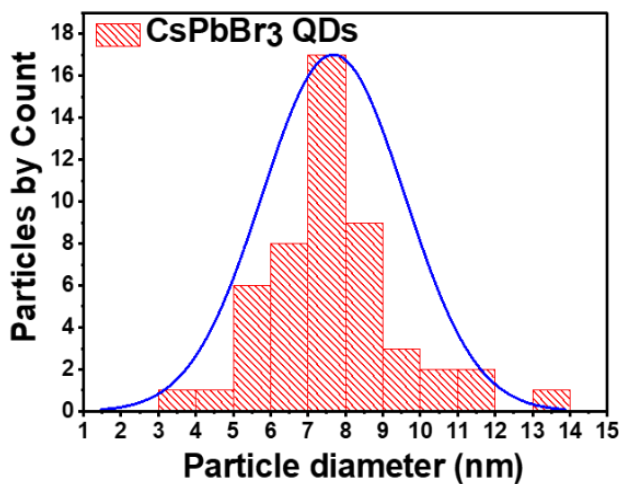
Figure 33 Histogram of TEM images of CsPbBr$_3$ Quantum dots

3.3.2.3 Field Emission Scanning Electron Microscopy

It is a microscopic technique which uses electron guns as the electron source. The field emission scanning electron microscopy (FESEM) allows to get information about topography and elements at a very high resolution of 1 to 0.5 nm and also high-quality, low-voltage images with negligible electric charging of the samples. On the other hand, the dielectric samples do not need to be necessarily coated with conducting materials for analyzing the samples.

In a typical FESEM, the electrons from an electron gun source are liberated in a high vacuum column. The electron beam is focused by electromagnetic lenses to bombard on the specimen/object. With the interaction of these electrons to the sample, secondary electrons are emitted which have a particular velocity and angle with the sample. Secondary electrons are detected by the detectors and produce an electronic signal based on their angle and velocities. Then the signals are amplified by an amplifier and can be seen on the screen as an image giving the desired information about topography. The general scheme of FESEM column is shown in figure 34.
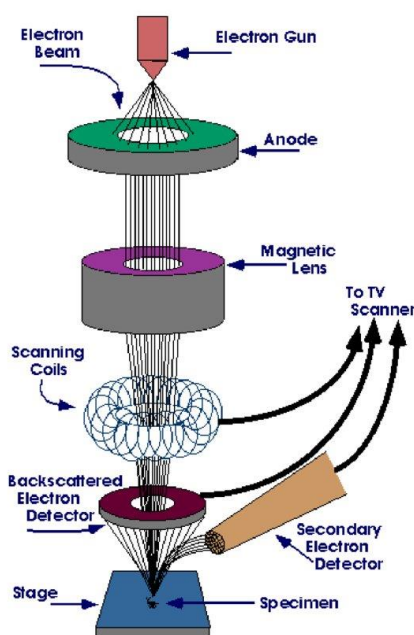
Figure 34 Schematic diagram of FESEM optical column representing its components This image has been taken from [3]

We have used the model Thermo Scientific Scios 2 model for measuring our samples. The following figure 35 shows FESEM images of ITO/MAPb$_{0.95}$Dy$_{0.5}$Br$_3$ films obtained during this thesis.
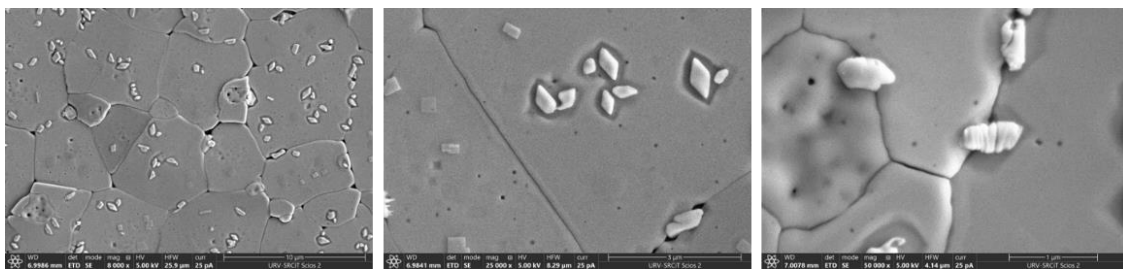
Figure 35 FESEM Images of MAPb$_{0.95}$Dy$_{0.5}$Br$_3$ film prepared during thesis

3.3.3 Electrochemical Characterization

3.3.3.1 Cyclic Voltammetry

It's an electrochemical technique which is used to estimate the highest occupied molecular orbital (HOMO)/lowest occupied molecular orbital (LUMO) levels of an organic molecule and conduction band (CB)/valence band (VB) of inorganic compounds. We have used this technique to estimate the energy levels of CsPbBr$_3$ NCs in a CH Instruments© 600c potentiostat/galvanostat with the help of three electrodes; carbon based working electrode, Ag/AgCl non-aqueous Ag/Ag+ reference electrode and the platinum wire as our counter electrode. The experiment was carried out at room temperature with toluene as the solvent of our sample and tetrabutylammonium hexafluorophosphate 0.1M as electrolyte. All the solution was used after bubbling a few minutes in nitrogen. In figure 36, we have shown the cyclic voltammetry (CV) curve of CsPbBr$_3$ NCs. To calculate the HOMO/LUMO levels, we use the oxidation/reduction peaks information with the following equation:

$$E_{HOMO} = -(E_{OX} + 4.8) \qquad \text{Equation 3.1}$$

$$E_{LUMO} = E_{HOMO} + E_{o-o} \qquad \text{Equation 3.2}$$

$$E_{o-o} = h \cdot c \, \lambda \qquad \text{Equation 3.3}$$

E$_{ox}$ is the oxidation potential obtained from the CV, E$_{o-o}$ is the band gap and λ is the wavelength resulting of the intersection between the absorbance and the emission band, h is the Planck constant $6.62607004 \cdot 10^{-34}$ m^2 kg /s and c is the speed of the light $3*10^8$ meter/sec.
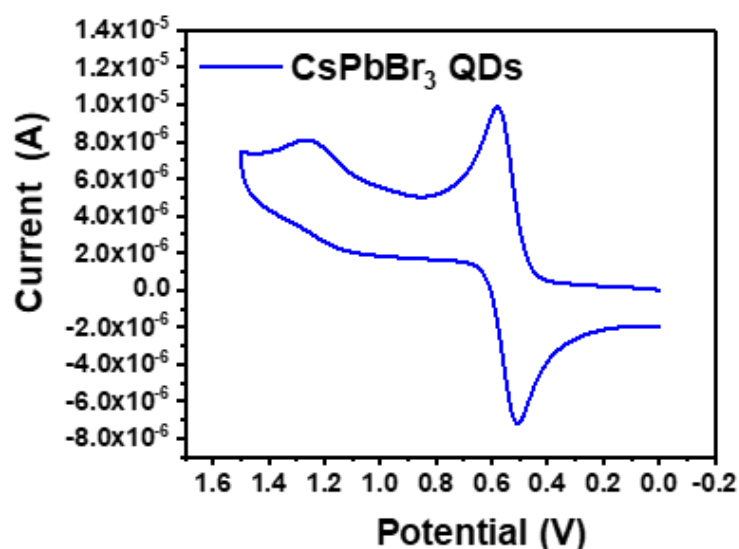
Figure 36 Cyclic Voltammetry of CsPbBr$_3$ NCs

The level alignment between the electrodes and the HOMO and LUMO or VB and CB levels of active layers determine how the electron and hole can easily move through the devices. We couldn't calculate the LUMO level of our NCs with this method because no reduction peaks were observed.

3.3.4 Surface Analysis

3.3.4.1 Contact Angle Measurement

It is a qualitative characterization technique to determine whether a material deposited on a surface or the surface itself is hydrophobic or hydrophilic in nature. We can also use this technique to learn about the wettability of potential solvents in the multilayer structure. In this method typically, a drop of water is dropped onto the surface. The intermolecular interactions between the drop and the surface determine the angle formed with the surface. When water is used, low angle values indicate that the surface is hydrophilic. We have used solvents with different polarities to check the hydrophobicity/hydrophilicity of different materials. In our thesis, we have used water and diiodo-methane for characterizing our films of silver nanowire ink AgNW 35 and AgNW 36 prepared with the doctor blade film coating method which are shown below in Figure 37. This technique was also used to study the effects of different underlying ETLs like PEI, PDINO and PEI/PDINO covered with the films of CdSe@ZnS prepared by spin-coating. For that we used water and toluene drops with the contact angle (Attension theta life optical tensiometer from Biolin scientific, Gothernburg, Sweden)
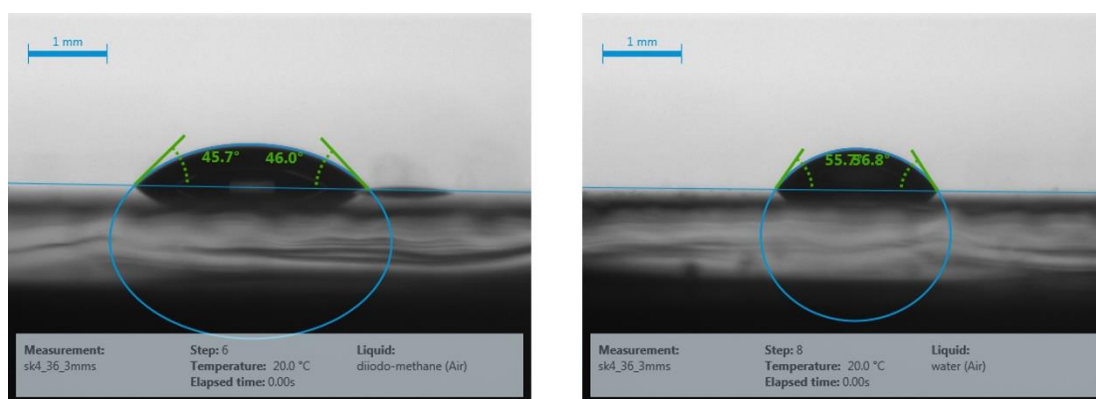
Figure 37 Contact angle measurement to the AgNWs films with different solvents

3.3.4.2 Atomic Force Microscopy

Atomic force microscopy (AFM) or Scanning Force Microscopy (SFM) is a non-optical high-resolution topography technique to study the roughness of the surface of the sample with 3-D imaging at nanoscale. In this thesis we have used the model of Molecular Imaging Pico SPM II (pico+) using the tip with curvature radius of 1 nm.

The basic operation of an AFM system includes an AFM probe in which a sharp silicon/silicon nitride AFM tip of the diameter 5-10 nm connected to AFM cantilever. The tip moves through the different height of sample which deflects the AFM cantilever, and it is recorded by a laser beam and a position sensitive photodetector (see Figure 38). The AFM cantilevers movement and the interaction force between the cantilever and surface is kept near constant by a feedback loop. The coordinates recorded by AFM tip are used to generate a three-dimensional topographic image of the surface.
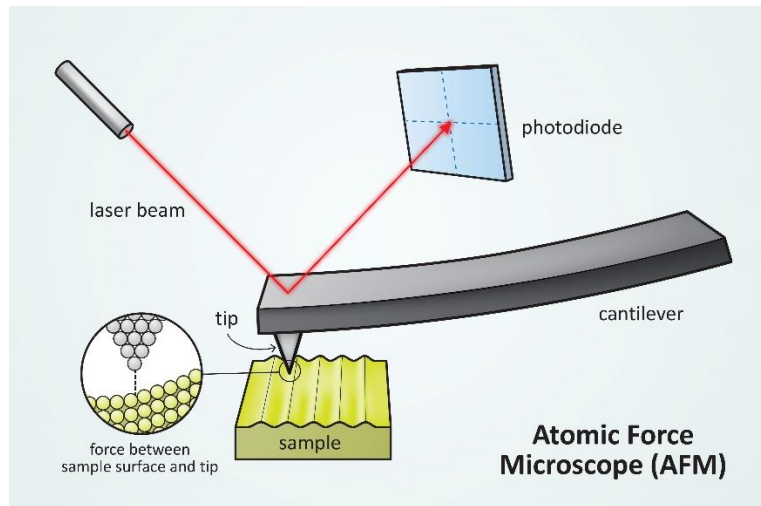
Figure 38 Illustration of a typical AFM system. Image taken from [4]

3.4 Film deposition techniques

To study our materials and for device fabrication, different film deposition techniques were used in our work which are explained below-

3.4.1 Spin-coating

This technique is used to form uniform thin films of thickness range from micrometer to nanometer. Here, the substrate is mounted on a chuck to rotate at a desired velocity, time and acceleration. The centrifugal force is responsible to spread the liquid radically outward, surface tension and the viscous forces are responsible for the flat surface of the deposited film. The solvent used for the spin-coating is either evaporated during the process or it is evaporated by the post-annealing process. The process of spin-coating a film is explained with illustration in figure 39.
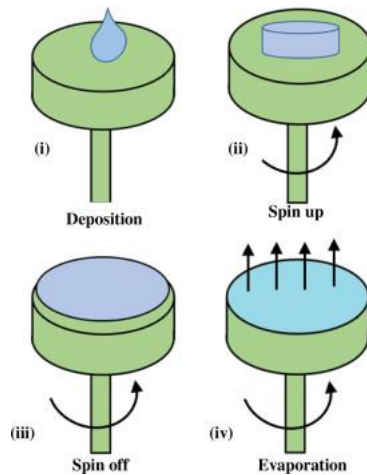
Figure 39 Simple illustration of the spin-coating method

There are different parameters which affect the thickness of the films, like spin velocity, acceleration and the spin time. Having the merits of smooth and uniform film forming capability, the technique has disadvantages of lacking material efficacy and incompatibility with large substrates. In our thesis, two different spin-coater have been used: WS-400E-6NPP from Laurell Technologies Corporation and the SPPIN150 wafer spinner from SPS Semiconductor Production Systems located in the at clean room and the glove box, respectively.

3.4.2 Thermal evaporation

This is a vacuum deposition technique that works on resistive heating principle. The substrates on which the material is to be deposited are mounted on a substrate holder in a vacuum chamber and the materials are placed in a sample source. When the current is applied through external sources, the boats get heated through it by the principle of "resistive heating". Because of the heated boat, the material starts to melt and finally starts to evaporate atom by atom.

At this stage, the distance between the boat and the shutter holder has a high importance in order to get the vaporized material to solidify to the substrate on its optimum. Also, the atoms of the material then align in the direction of the substrates because of the high vacuum of 10^{-6} mbar. The organic layers can be deposited by manual thermal evaporation. We have deposited the metal contacts and buffer layers in our devices with this technique. One schematic diagram of thermal evaporation chamber is shown below in Figure 40. The thermal evaporator INFICON SQC-310C was used in this thesis to

evaporate materials with the controller with model CreaPhys GmbH CU 103 for manual evaporation.
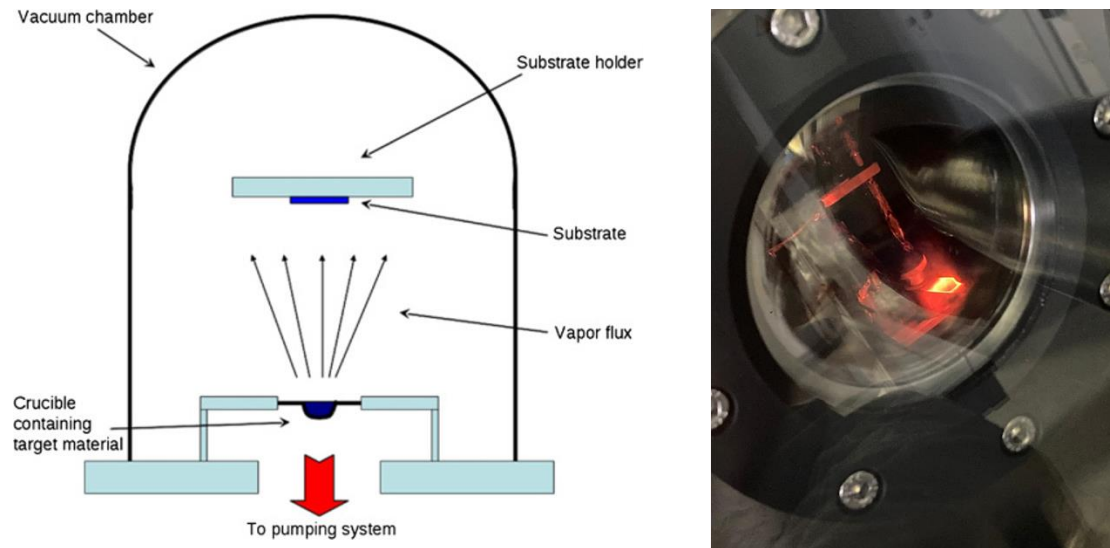
Figure 40 Simple illustration of thermal evaporator and an Al evaporation on our devices

3.4.3 Doctor-Blade

The technique is used to make films of micrometer thickness. The solution to be coated is placed in the front of a blade which is placed a fixed distance from the substrate to be covered. Then, the blade is moved in-line across the substrate resulting in the creation of wet film. In spite of the easy process of making the film, this technique requires a few attempts to get the optimum conditions. On the other hand, the solution losses in this film deposition technique are about 5%. We have prepared the films of AgNWs ink 35 and 36 on the top of glass by this technique with ZAA 2300 Zehntner Automatic Film applicator during my stay in Eurecat. A typical doctor blade equipment is shown below in figure 41.
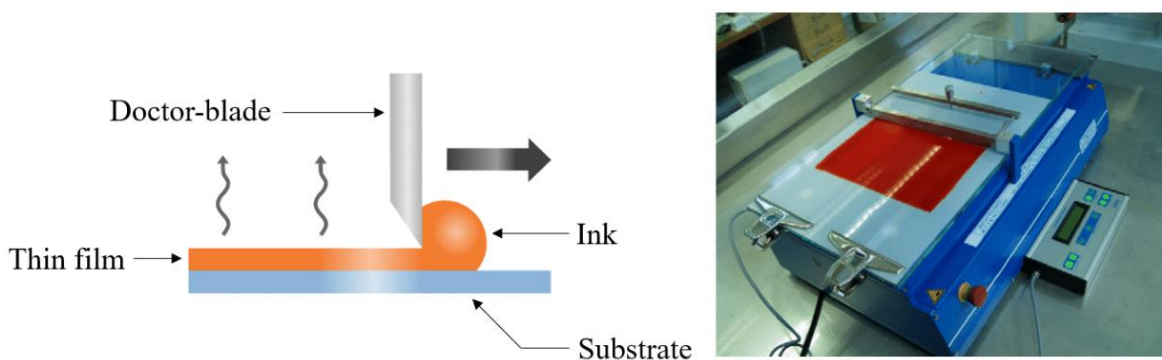
Figure 41 Doctor blade technique illustrative diagram (left) and image of the model used in the thesis (right).

3.4.4 Dip-coating

This is a simple, reliable and low-cost technique for the deposition of films. The substrate is immersed into the solution and taken out after a certain time resulting in a thin film which can later be dried by annealing process or blow drying. The technique is economically friendly and can be useful with different metallic, ceramic, polymer films and fibrous materials surface (see Figure 42).

In our thesis, we used this method to deposit two self-assembled molecules (SAMs) EADR03 and EADR04 on the top of ITO as hole transporting layers in $CsPbBr_3$ NCs perovskite LEDs and to prepare ITO/SAMs/ $CsPbBr_3$ NCs films. For that, we immersed clean substrates in the SAM solution and kept it for 4 hours at 50^0 C. Later, the substrates were rinsed by the iso-propanol alcohol by spin coating at 3000 rpm for 30 seconds.
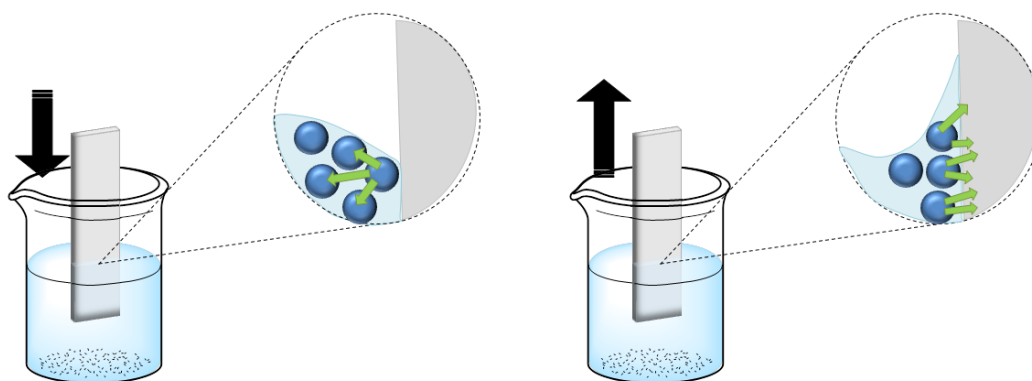
Figure 42 Illustrative diagram of the Dip-coating method. Image is taken from [5]

3.5 Device Construction

A Light Emitting Diode (LED) is a multilayer structure where an emissive layer is sandwiched between hole transporting and electron transporting layers which are then layered between cathode and anode. There are two configurations of an LED device:

Normal structure (p-i-n) - If the hole transporting layer is deposited on the top of substrate, the substrate works as anode in the operation of LED and the architecture of the device is called normal structure or p-i-n structure which states p-type semiconductor, intrinsic semiconductor and n-type semiconductor respectively from bottom to the top as shown in figure 43.
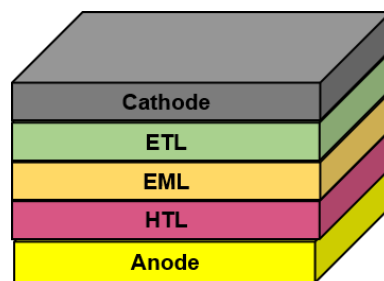
Figure 43 General Architecture of p-i-n structured LEDs

Inverted structure (n-i-p) - If the electron-transporting layer is deposited at the top of substrate, the substrate works as cathode in the operation of LED and the architecture of the device is called inverted structure or n-i-p structure which states the existing layers of n-type semiconductor, intrinsic semiconductor and p-type semiconductor respectively from bottom to the top as shown in figure 44.
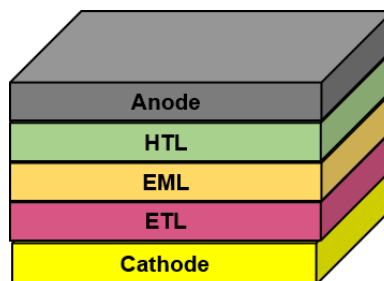
Figure 44 General Architecture of n-i-p structured LEDs

For the device construction/fabrication, a Transparent Conducting Oxide (TCO) coated glass substrate is used. TCO provides a conductive path to the electrons via external

circuit. As TCO materials, mainly Fluorine doped tin oxide (FTO), Indium doped tin oxide (ITO) and boron doped zinc oxides are used. These can be coated on the glass substrate by the very known thin film deposition techniques like epitaxial growth, physical vapor deposition, chemical vapor deposition and sputtering. In this thesis, we have worked with ITO as substrate (15x15 mm, 15 Ω sq^{-1} and also 25x25 mm, 15 Ω sq^{-1}, commercialized available at Xinyan Technology Limited and Automatic Research GmbH respectively.).

3.5.1 Substrate Cleaning

For making the LEDs, the first step is to clean the substrate. We cleaned our substrate with the first diluted Hellmax soap mixed with distilled water by ultrasonicating the solution for 10 min. After that we repeat the distilled water cleaning for 10 minutes without soap. We then added acetone for cleaning for 10 min of ultrasonication and in the end we repeated the same steps with Iso-propanol alcohol two times.

3.5.2 Device Assembly

The second step is to deposit the layers. Before that we expose our cleaned substrate to the UV-Ozone lamp for 30 minutes to remove any possible organic contamination and smoothen the surface. For deposition of hole transport layers, emissive layer, and electron transport layers we have used the spin-coating method. The borders of the device are wiped and cleaned after each layer with the help of corresponding solvents. In the end, we deposited the metal contacts cathode (or anode) depending upon the architecture of the device if its normal or inverted structure. The active area, defined by the area where all the layers are superposed, is 3 mm x 3 mm, for the devices prepared at ICIQ, and 5 mm x 5 mm for the devices prepared at Eurecat. Finally, our device construction is completed (see figure 45). We have also encapsulated our devices by applying 3 drops of an encapsulating resin LumTec LT-U001 on the active area followed by device treatment with UV lamp for 10 minutes to dry the resin.
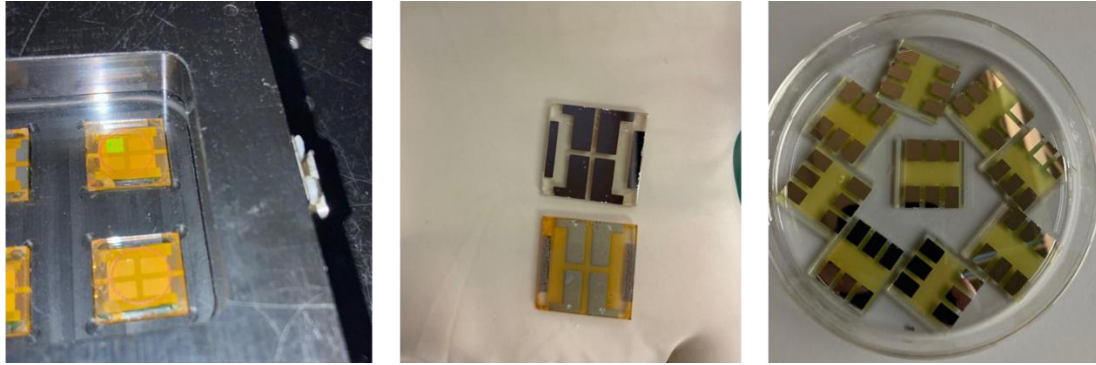
Figure 45 Pictures of real devices prepared during thesis In ICIQ and Eurecat with active area of 9 mm^2 (left) and 25 mm^2 (right) respectively

3.5.3 Fabrication of F8BT based organic light emitting diodes

OLEDs with normal structure of ITO/PEDOT: PSS/F8BT /LiF/Al were fabricated while learning the device fabrication procedure. ITO was used as the substrates and cleaned with isopropanol alcohol and acetone in ultra-sonicator for 40 minutes followed by UV-Ozone treatment for 30 minutes. PEDOT: PSS was spin-coated as hole transport layer at 4000 rpm for 45 sec and heated at 150 ^{0}C for 30 minutes. For the emissive layer, F8BT polymer [poly(9,9-dioctylfluorene-alt-benzothiadiazole)] was dissolved in chloroform at 23 mg/ml concentration to spin-coat on the top of HTL at 3000 rpm for 60 sec followed by annealing at 110 ^{0}C for 30 minutes. To complete the device, LiF (0.8 nm) and Al (100 nm) were thermally evaporated on the top of the F8BT layer as electron injection and cathode layer respectively. The following figure 46 shows the OLED function which is fabricated with the above procedure.
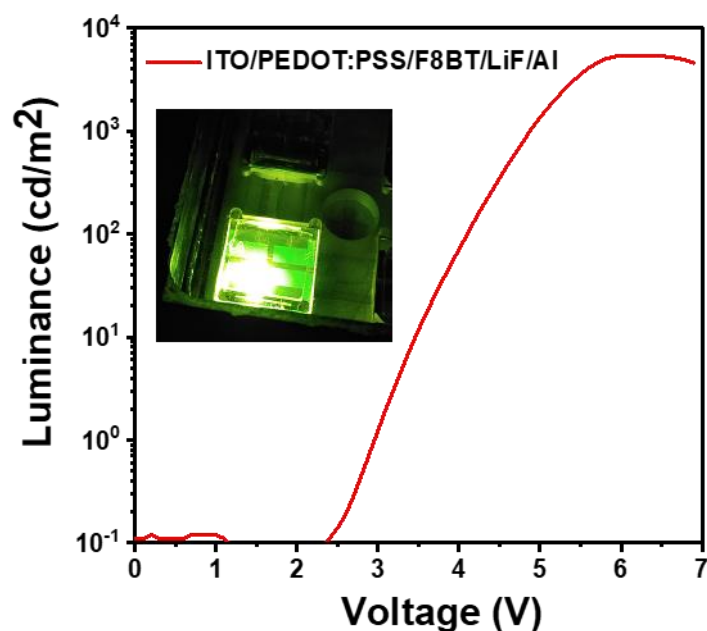
Figure 46 Luminance vs Voltage curve for the F8BT based OLED

3.5.4 Electron Only Devices

The electron only devices were prepared to study the electron mobility using the Space charge-limited current (SCLC) model. The curves were fitted using the Mott-Gurney law, (equation 3) with PEI and PDINO as electron transporting layers. For that, we prepared the three different configurations of ITO/QDs/TPBi (30 nm)/LiF (0.8 nm) /Al (120 nm), ITO/PEI/QDs/TPBi (30 nm) /LiF (0.8 nm) /Al (120 nm) and ITO/PDINO/QDs/TPBi (30 nm) /LiF (0.8 nm) /Al (120 nm). In all the devices, PDINO was dissolved at 1mg/ml in MeOH and spin-coated at 6500 rpm for 45 sec. PEI layer 0.2 wt% was dissolved in EtOH and spin-coated at 3000 rpm for 40 sec followed by annealing at 120 ^{0}C for 15 minutes. For deposition of CdSe@ZnS quantum dots, we used 1000 rpm for 60 sec followed by100 ^{0}C for 20 minutes.

To measure the electron mobility and trap densities of the devices, we have used the Keithley 2400 as a voltage source to obtain J-V curve for the devices with reference, PEI and PDINO based devices. Electron mobilities were obtained with the help of the following equation 3.

Equation 3
$$Jscl = \frac{9}{8} \in_0 \in_R \mu_e \frac{V_1^2}{L_1^3}$$

Where, J_{scl} is charge limited current in mA/cm^2, ϵ_0 is the permittivity of free space which is measured in C^2/N·cm^2, ϵ_R is the dielectric constant, which is unitless, L is the thickness of the active material in cm and μ_e is the electron mobility which are measured in m^2 V^{-1} S^{-1}.

On the other hand, trap density of devices was measured with the help of following equation 4.

Equation 4
$$N_{trap} = \frac{2V_{TFL}\epsilon_0\epsilon_R}{qd^2}$$

Where N_{trap} is the trap density measured in cm 3, V_{TFL} is trap filled limit voltage measured in V, q is electron charge measured in Coulomb and d is the thickness of the layer in cm. Again ϵ_0 is the permittivity of free space which is measured in C^2/N·cm^2, ϵ_R is the dielectric constant which is unitless.

3.6 Device Characterization

After the device construction, the next step is to characterize the devices. For characterizing the devices, we first record the variations in light emission and current density as a function of applied bias. Second, we record the operational stability of the devices.

I have worked with three different set ups for characterizing the LEDs in ICIQ, Eurecat and INAM respectively.

3.6.1 Luminance-Voltage-Current density Characteristics

In ICIQ, we have used a Keithley 2400 as a voltage source and Konica Minolta LS100 luminance meter to measure our devices. The camera needs to set up facing the devices and focus on the middle of the diode of the substrate containing four light emitting diodes. For measuring the Luminance-voltage and Current density-voltage, we set up measuring parameters like voltage range, compliances, and device area in the home-made software.

By applying the voltage from the source meter, the charge carriers begin to flow, and the devices begin to illuminate at their corresponding turn-on voltage. We have also

measured the current efficiency with the same set-up. Figure 47 a) and b) shows the variation of the current efficiency with current density and the variation of Luminance with applied bias respectively.
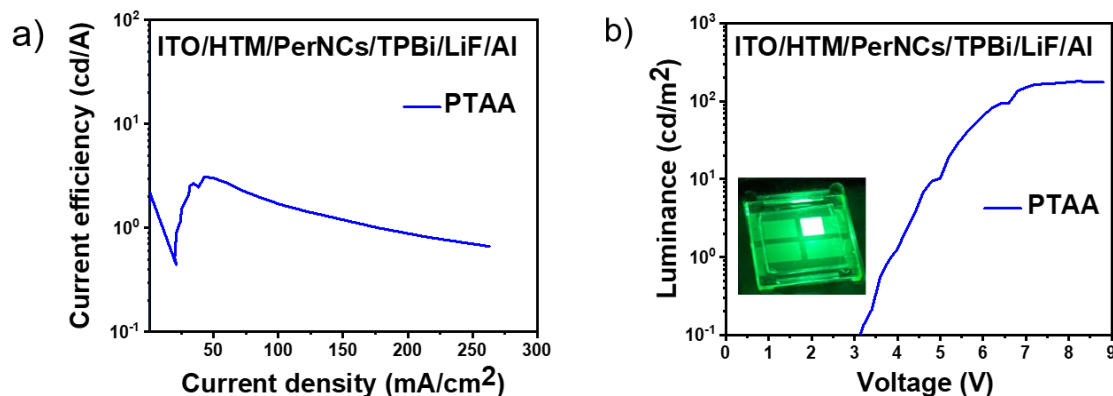
Figure 47 a) Current efficiency vs Current density curve b) Luminance vs Voltage curve of a PeLED prepared during thesis

In Eurecat, both the current intensity-voltage and photogenerated current-voltage were recorded using a photodiode in combination with Keithley. With this method, we do not measure the LEDs directly in luminance (Candela/m^2) but in radiometric units (Watts/cm^2). We changed the watts to candela/m^2 with a specific electroluminescence spectrum of sample and the standard luminosity function. Here, luminosity function represents the sensitivity of human eye to a particular wavelength. We have used - UV Enhanced SM1PD2A Silicon Photodiode, 200-1100 nm with Cathode Grounded from Thorlabs for measuring the devices.

In the Institute of Advance Materials (INAM), we have used integrated sphere to measure our devices with model A10104-01 from Hamamatsu Photonics K.K Japan which in combination with a detector from Hamamatsu Photonic Multi channel analyzer PMA-12.

3.6.2 Operational Stability Measurements

For measuring the operational stability of our devices, we have applied a constant current, determined from the previously measured IV curves, to the diode and recorded the variation of the luminance versus time. We observe an initial luminance which decreases exponentially with time which is shown in the following figure 48 which shows that the device undergoes a degradation with time.
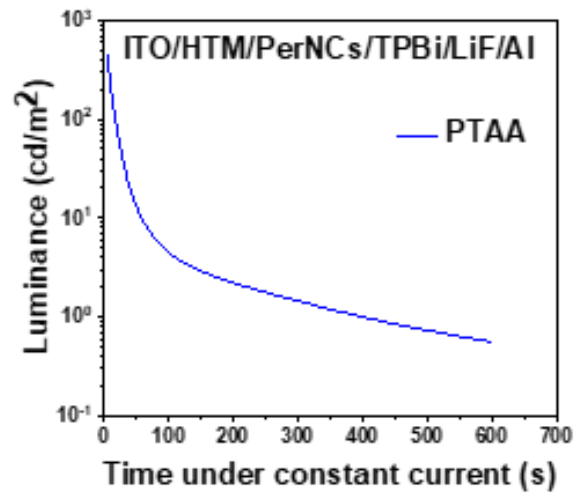
Figure 48 Luminance vs Time for CsPbBr$_3$ NCs based PeLED prepared during thesis

3.7 References

1. Protesescu, L. *et al.* Nanocrystals of Cesium Lead Halide Perovskites (CsPbX$_3$, X = Cl, Br, and I): Novel Optoelectronic Materials Showing Bright Emission with Wide Color Gamut. *Nano Lett.* **15**, 3692–3696 (2015).

2. Lee, Ki-Heon, et al. "Highly efficient, color-reproducible full-color electroluminescent devices based on red/green/blue quantum dot-mixed multilayer." *ACS nano* 9.11 (2015): 10941-10949.

3. Billah, A. H. M. A. "Investigation of multiferroic and photocatalytic properties of Li doped BiFeO3 nanoparticles prepared by ultrasonication." *Bangladesh University of Engineering and Technology, Dhaka, Bangladesh* (2016).

4. Scientific-Image-Atomic-Force-Microscope-Illustration @ Www.Nisenet.Org.

5. 69-dip-coating-for-the-fabrication-of-thin-films @ services.icmab.es.

Chapter 4: Self-Assembled Monolayers as HTLs for CsPbBr$_3$ Nanocrystal Perovskite Light Emitting Diodes

Abstract

Lead halide perovskite nanocrystals have successfully been incorporated in the fabrication of light emitting diodes (LEDs) as the promising emissive material. However, the conventionally used hole transport layers lead to poor stability and efficiency in the devices. In this Chapter, we have described the use of two different carbazole-based molecules (self-assembled molecules, SAMs) as hole transporting material in CsPbBr$_3$ perovskite nanocrystal based green LEDs. The two SAMs are different to each other by one phenyl ring in the bridge which enhances the operational stability of the LEDs in comparison to the extensively used polymer PTAA.

4.1 Introduction

Metal halide perovskite (MHP) semiconductors with the general formula ABX_3, where A and B are monovalent and divalent cations (A = $CH_3NH_3^+$, Cs+ , $HC(NH_2)^{2+}$, B= Pb^{2+}, Sn^{2+}) and X is the halide anion (Cl^-, Br^-, I^-), have attracted much interest since 2009 the influential work from Miyasaka et al.[1][2]. Metal halide perovskites not only have the tunable emission wavelength, good photoluminescent quantum yield, high absorption coefficient, high charge-carrier mobility, low excitonic binding energy and long excitonic diffusion length,[3] but also, they can be easily solution processed at low temperature. With those physical properties, these materials have not only been applied in the field of photovoltaic cells but also in light-emitting diodes (LEDs)[4], photodetectors,[5],[6] and LASERs.[7] In particular, the excellent properties of metal halide perovskites like narrow spectral distribution and high color purity, have pushed their application in perovskite-based LEDs.[8] A seminal work reported by Zhi-Kuang Tan et al in 2014 shows green light emission and external quantum efficiency (EQE) of 0.1%. [9] Since then, the different perovskite materials have been used for the PeLEDs and the research has grown exponentially. Since last years, the maximum EQE achieved from PeLEDs has increased up to 23.8% till date for green LEDs,[10] which is comparable to CdSe based quantum dot LEDs.[11]

Despite these promising results, PeLEDs still face several challenges to be used commercially. However, the highest efficiency in PeLEDs comes from the application of lead-based perovskite materials; thus, the toxicity of the device can be considerable at large -scale. On the other hand, long-term stability and efficiency also are the major drawbacks.[12] In this sense, some reports suggested that Tin-based perovskites can replace the lead-halide perovskites for efficient and stable solar cells.[13],[14] Moreover, PeLEDs are operated at the high external bias and high current densities which increases the stress on materials and affects the stability and efficiency.

On the one hand, there are several factors that affect the operational stability like presence of defects and the ion migration processes in ABX_3 perovskite materials, the charge accumulation at the interfaces and the generation of local heat. The defects present in the perovskites, the effect of ion mobility, weak light outcoupling efficiency and the existence of unbalanced charge injection into the active layer are the key factors for

the decreased efficiency of the devices. To reduce the ion mobility and the presence of defects, researchers have investigated several methods, one of them is to prepare the low-dimensional perovskites such as colloidal perovskite $CsPbBr_3$ nanocrystals (MHP NCs). These nanometer-sized semiconductors, whose size typically ranges between 2-20 nm, exhibit narrow full-width at half maximum (FWHM) photoluminescence (PL), hence high color purity, and almost unity PL quantum yield, which makes them very appropriate materials for LED application.[15] In the device, the interface between the emissive layer and charge transport layer plays an important role in determining the performance. Therefore, passivation of not only NCs but also interface between NCs layer and charge transport layer is crucial for the optimum stability of device. One strategy is molecular passivation, which has potentially reduced the non-radiative recombination and hence increased the stability of the devices.[16]

For PeLEDs, the most popularly used hole transporting material is poly (3,4-ethylenedioxythiophene) polystyrene sulfonate (PEDOT: PSS). In spite of having high solution processability, moderate band gap (2.9 eV), good thermal stability, high transmittance in the visible range and adequate hole conductivity, the device suffers with the hygroscopic and acidic nature of PEDOT: PSS which causes the degradation in the device and hence reduces their lifetime.[17] On the other hand, PTAA, (poly [bis(4-phenyl) (2,5,6- trimethylphenyl) amine), another widely used polymer in the field of PeLEDs is more hydrophobic in nature but has high cost (1000 euros/gr), that limits its potential application for large-scale devices. Therefore, the need to substitute these materials by SAMs help in simplifying the device architecture, avoids interlayer mixing and reduces the amount and cost of the materials used for fabricating the devices which is a step towards more economically friendly devices.

In this thesis, we have used two carbazole-based self-assembled molecules, EADR03, (4-(3,6-bis(2,4-dimethoxyphenyl)-9H-carbazol-9-yl) benzoic acid) and EADR04, (4'- (3,6-bis (2,4- dimethoxyphenyl) - 9H-carbazol-9-yl) - [1,1'-biphenyl] - 4 - carboxylic acid) which are shown in figure 49a), as hole transporting layer in $CsPbBr_3$ PeLEDs. The complete device structure and the energy level diagram of all the materials used in the devices is shown in figure 49c) and 49b) respectively. We have compared the device performance constructed with SAMs for HTM with the devices based on PTAA and without HTM.
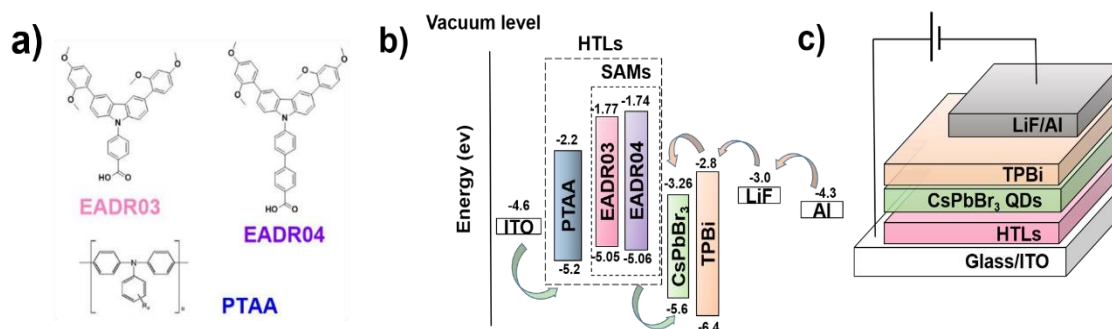
Figure 49 (a) Molecular structures of the materials used as HTM in this work; (b) energy levels and (c) device structure of the PeLEDs prepared in this work.

4.2 Experimental Section

In this work, we have synthesized the CsPbBr$_3$ nanocrystals, and the two SAM molecules were synthesized previously by our colleagues Dr. Ece Aktas and Dora Alejandra González Ruiz. The synthesis is reported elsewhere.[18]

4.2.1 Film fabrication

We have prepared the films of ITO/HTLs/NCs with EADR03 and EADR04 as SAMs HTL and the reference films with PTAA as HTL and no HTL for optical and morphological characterization. The SAMs and PTAA were deposited with the same conditions as device fabrication described below.

4.2.2 Device fabrication

In this work, we have used Indium-doped Tin Oxide (ITO) coated/patterned glass substrates (15 mm x 15 mm) as the anode for our devices which has the sheet resistivity of 15 Ω/m^2.After cleaning, the ITOs were transferred to UV/Ozone equipment for Ozone treatment of the substrates for 30 min prior to further deposition of layers. PTAA, purchased from Sigma-Aldrich was dissolved in toluene (2 mg/mL) and deposited as the hole transporting material on the substrates at 5000 rpm for 30 seconds followed by annealing at 100 ºC for 10 minutes which forms the smooth layer of 10 nm. Also, EADR03 and EADR04 were dissolved in anhydrous isopropanol (1 mg/mL) and

deposited with dip-coating method on the ITO substrates by immersing completely in the SAM solution and keeping them undisturbed for 4 h at constant temperature of 40 °C. Later, the substrates were rinsed by spin-coating IPA at 3000 rpm for 30 s followed by drying them with nitrogen for removing extra unattached molecules. The substrates were then transferred to N_2 filled glove box for further deposition. 50 µL of the $CsPbBr_3$ NCs solution as emissive material was spin coated on each device at 5000 rpm for 60 s followed by thermal annealing for 20 min at 100 °C. The devices were then transferred in an air-tight container to the thermal evaporator for thermal deposition of further layers at the base pressure of 1×10^{-6} mbar. 50 nm thin layer of an electron transporting material TPBi {2,2',2''-(1,3,5-Benzinetriyl) -tris(1-phenyl-1-H-benzimidazole)} was evaporated on the devices, 1 nm of Lithium fluoride (LiF) as a buffer layer and 100 nm of aluminum (Al) as cathode was deposited automatic evaporation. This process completes the fabrication of our PeLEDs which have an active area of 9 mm^2.

4.3 Result and Discussion

4.3.1 Nanocrystal Characterization

After the synthesis, we have characterized our NCs colloidal dispersion in toluene to study their optical properties.

The estimation of the PLQY of the NCs calculate at different excitation wavelengths of 435 nm, 445 nm and 455 nm were 27%, 27.6% and 29.5% respectively.

For the different measurements of NCs and Coumarin dye, toluene and ethanol were used as a reference shown in figure 50a) and 50b). The PL maximum after excitation at 424 nm was located at 518 nm with a full width at half maximum (FWHM) of 23 nm. Finally, the PLQY were estimated at three different excitation wavelengths 435, 445 and 455 nm, which were chosen between the absorbance maximum of NCs (at 518 nm) and the coumarin dye (at 522 nm) respectively.
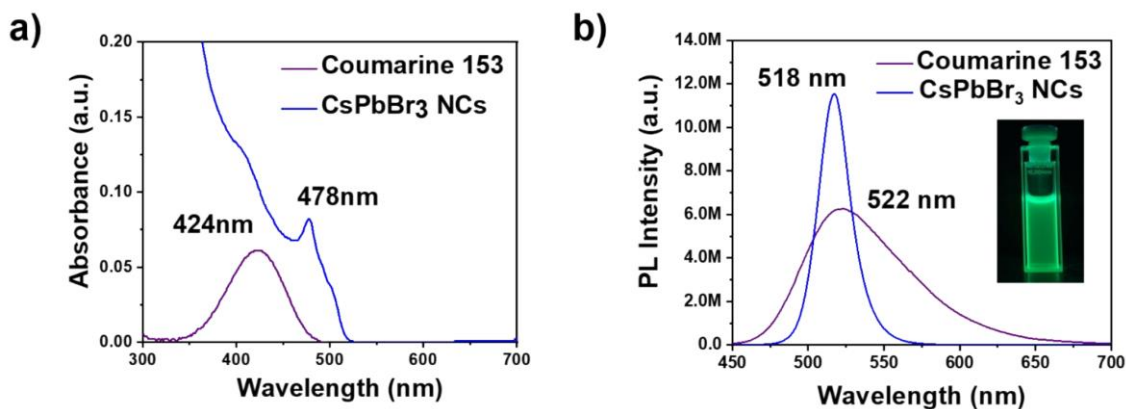
Figure 50 UV-vis absorption (a) and fluorescence spectra (b) of the CsPbBr₃ NCs in toluene solution and the solution of coumarin 153 was used as reference. The excitation wavelength was 424 nm.

For the further estimation of radiative lifetimes of our NCs, time correlated single photon counting (TCSPC) measurements were performed. The measurements were done at a constant 50 ns for the NCs and 120 ns for the NCs solution shown in figure 51. The fluorescence decay lifetime was fitted using a bi-exponential function. Finally, the average lifetime of the fluorescence decay of the nanocrystals is 9.6 ns.
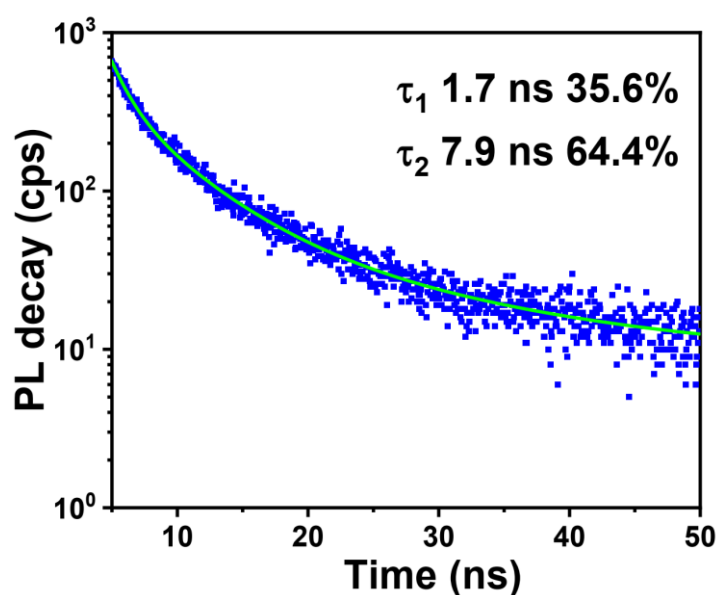
Figure 51 Photoluminescence decay with time of the CsPbBr₃ NCs in solution after excitation at 470 nm. the solid line represents the exponential fitted decay whose fitting parameters are indicated in the legend.

To know the size and morphology of nanocrystals, we have analyzed them with Transmission electron microscopy (TEM) shown in figure 52a). We have found that the NCs were nearly cube shaped NCs with average size of 7.6 ± 1.9 nm which is shown through a size-distribution curve in figure 52b). The XRD pattern shown in figure 52c)

reveal peaks located at 13.7º, 15.1º, 21.3º, 24.1º, 30.1º, 33.8º, 37.5º and 45.9º that correspond to the reflections of the crystal planes (100), (110), (200), (211) and (202) corresponding to the cubic structure. Cyclic voltammetry measurements of NCs were performed using a computer controlled potentiostat in a three-electrode cell shown in figure 52d).
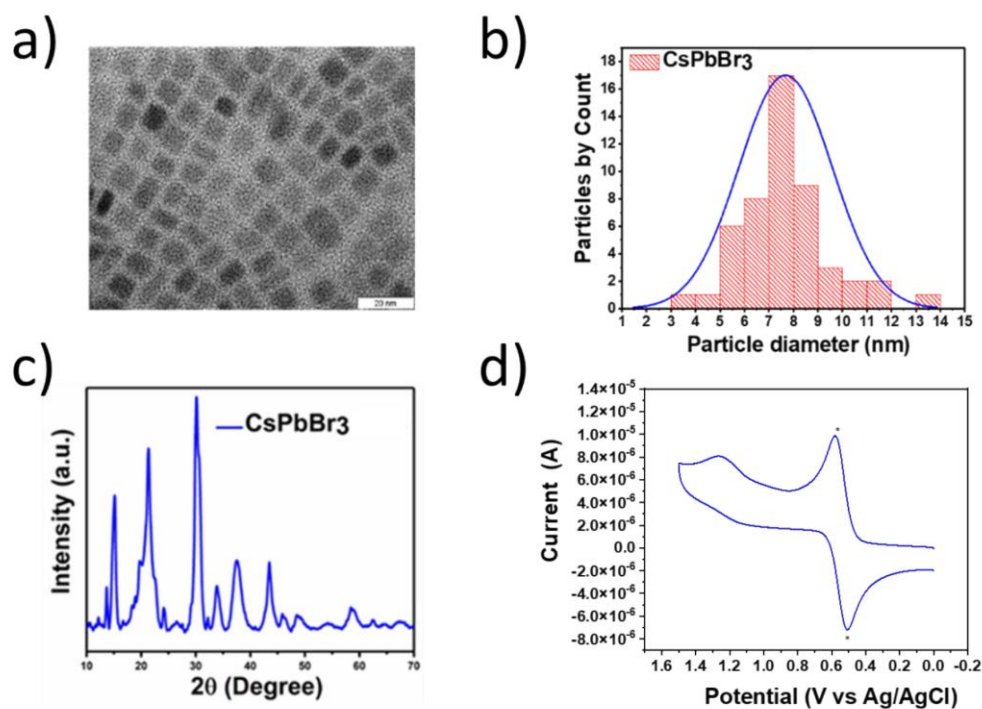
Figure 52 a) TEM images of the $CsPbBr_3$ nanocrystals (NCs) prepared in solution, b) Histogram showing the particle size distribution c) XRD pattern of the $CsPbBr_3$ NCs measured in solution d) Cyclic voltammogram of the PSK NCs measured in toluene and 0.1 M $TBAPF_6$ using ferrocene as internal reference (the corresponding signals are marked as *)

Whereas the valence band has been calculated by cyclic voltammetry to be at -5.6 eV (Fig. 52d), the band gap of the NCs has been estimated at 2.34 eV with the help of Tauc plot shown in Figure 53. By combining both measurements, the conducting band (CB) has been estimated to be at -3.26 eV which agrees with the values reported previously in the literature calculated by cyclic voltammetry and UPS.[19,20,21]
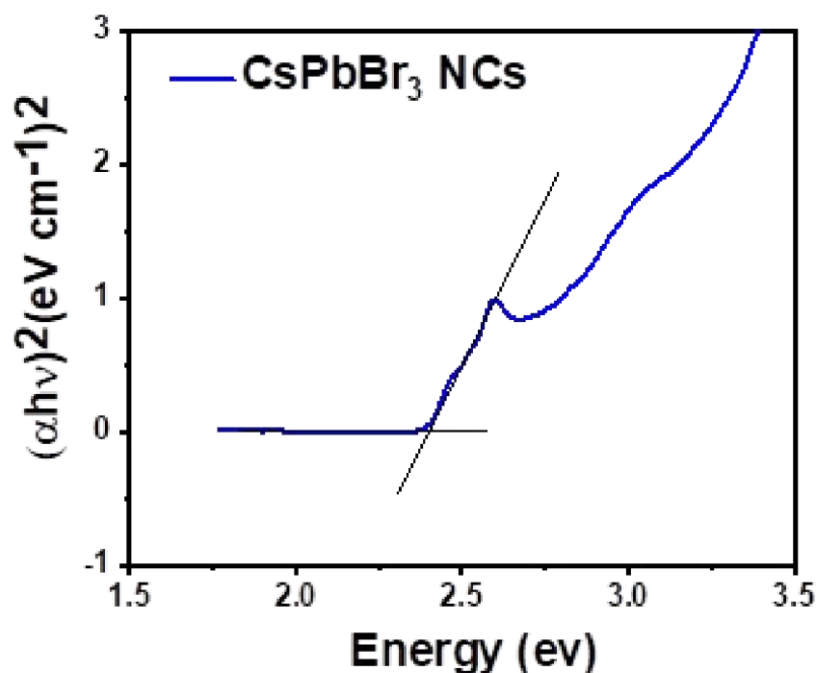
Figure 53 Tauc plot of the CsPbBr₃ NCs in toluene solution

4.3.2 Films Characterization

For the optical characterization of films, the samples were made of ITO/HTM/MHP NCs/PMMA where PMMA is a thin layer of poly methyl methacrylate (PMMA) deposited on top to prevent degradation. The figure 54 shows the optical characterization of the films. The UV-VIS absorption spectra of the films which have SAMs as underlying HTL, shows the peaks at 475 nm as shown in figure below 54a). While figure 54b) indicates the PL peaks at 513 nm in the films for both the SAMs and at 517 nm in the films with PTAA and Blank. The calculation of FWHM indicated in the table 2 shows that PL peaks of the films PTAA and Blank coincides with the PL of NCs solution whereas PL signal is broader in case of the films with SAMs molecules underlying that the NCs are more dispersed when in contact with SAM molecules.
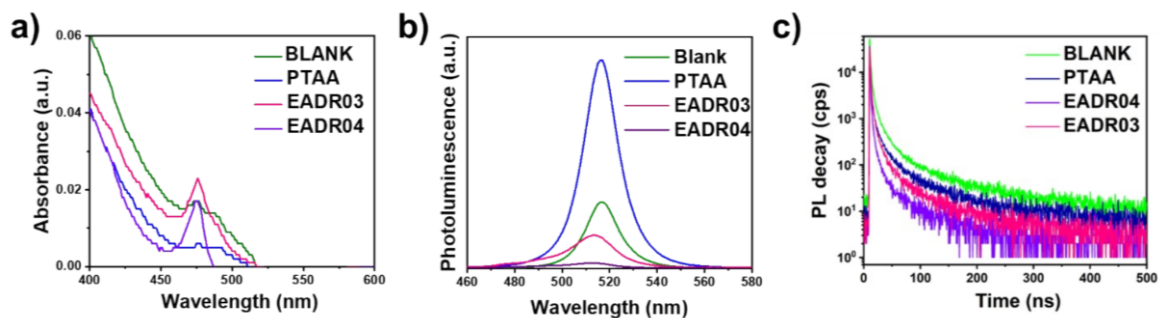
Figure 54 Optical characterization of the films made of ITO/HTMs/CsPbBr3 NCs: (a) UV-VIS absorption spectra, (b) Steady-state fluorescence spectra of the samples covered with PMMA, and (c) Fluorescence time decay of the samples measured after excitation at 470 nm.

To understand the reason behind the blue shift with SAMs, we have performed the PL spectroscopy again with the NCs mixed with PTAA and NCs mixed with EADR04. We found that the PL signal of NCs solution mixed with PTAA are similar with the NCs solution alone where the PL signal of NCs mixed with EADR04 shows a blue shift shown in figure 55. This indicates that the methoxy substituents could interact with the Pb atoms and Cs^+ ions at the surface and donate the electrons by a Lewis acid-base reaction inducing a 4 nm of blue-shift.
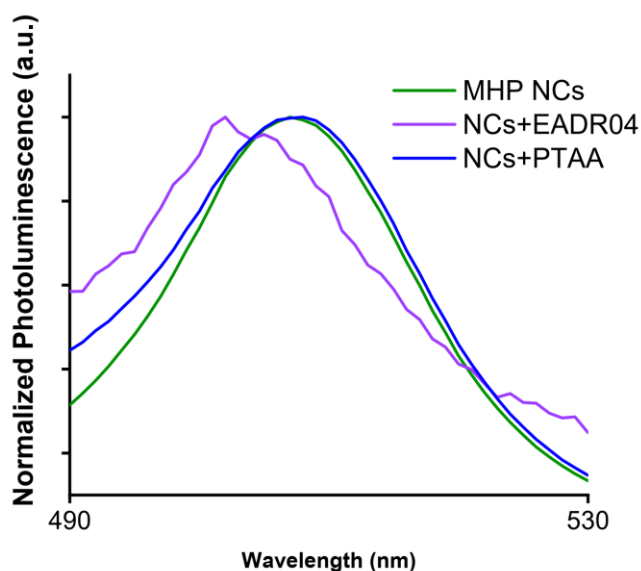
Figure 55 PL Steady-state fluorescence spectra of the solutions of MHP NCs, MHP NCs mixed with PTAA and MHP NCs mixed with **EADR04.**

Time correlated single photon counting (TCSPC) shown in figure 54c) indicates that with the EADR04 films, the signal decays faster in comparison to the NCs in solution showing an efficient extraction of carriers by SAMs when compared to the signal decays of PTAA based films. Two decay lifetimes were observed which are assigned to the radiative recombination due to surface defects which are fast decays and into the bulk which leads to slow decays. It is interesting that EADR04 decreases the lifetime and weighting coefficient for surface defects and increases the same for the bulk. Here, we understand that both the SAM molecules have the same peripheral substituents and yet EADR04 shows better charge transport ability than EADR03.

ITO/HTMs/NCs	λ_{max} (nm)	FWHM (nm)	τ_{av} (ns)	τ_1 (ns)	A_1 (%)	τ_2 (ns)	A_2 (%)
Blank	517	18	69.9	17.2 ± 0.7	29.8	92.4 ± 3.1	70.2
PTAA	517	18	71.1	21.1 ± 1.4	33.1	95.7 ± 5.9	66.9
EADR03	513	22	67.1	19.1 ± 1.0	34.5	92.5 ± 6.0	65.5
EADR04	513	27	56.2	15.4 ± 2.9	23.1	68.5 ± 6.1	76.9

Table 2 Fluorescence characterization of the MHP NCs deposited on top of different HTMs/ITO samples: maximum intensity wavelength and FWHM of the peak estimated from
steady state fluorescence, and average fluorescence lifetime decays (τ_{av}), lifetime values (τ) and weighting coefficients for each decay channel (A).

Contact angle measurements done of the substrates ITO/HTM with water droplets reveals the wettability of the HTMs which are shown in table 3 and already reported[18]. It is evident that the nature of the substrates changes from hydrophilic character in the case of the bare ITO, to hydrophobic when PTAA is deposited and yet the NCs film deposited by spin-coating forms a continuous film.

For studying the surface topography, ITO/HTM/NCs films were fabricated to analyze by Atomic Force Microscopy (AFM) which are shown in figure 56. The films roughness RMS values are shown in table 3 which are lowest in case of SAMs. Considering that the average size of NCs are 7.6 nm and RMS values are nearly 5 nm with the difference of less than 1 nm, it suggests that the films formed are not completely homogenous. Additionally, we have estimated the grain densities of these samples indicating that the blank samples contain higher numbers of NCs per unit area than the other samples. On the other hand, the total volume between the grain surface and the plane of PTAA and Blank are higher than in comparison to EADR03 and EADR04 which is shown in table 3

suggesting that even if RMS values and grain densities are similar, the NCs layer deposited on the top of PTAA is thicker than the same layer deposited on SAMs.
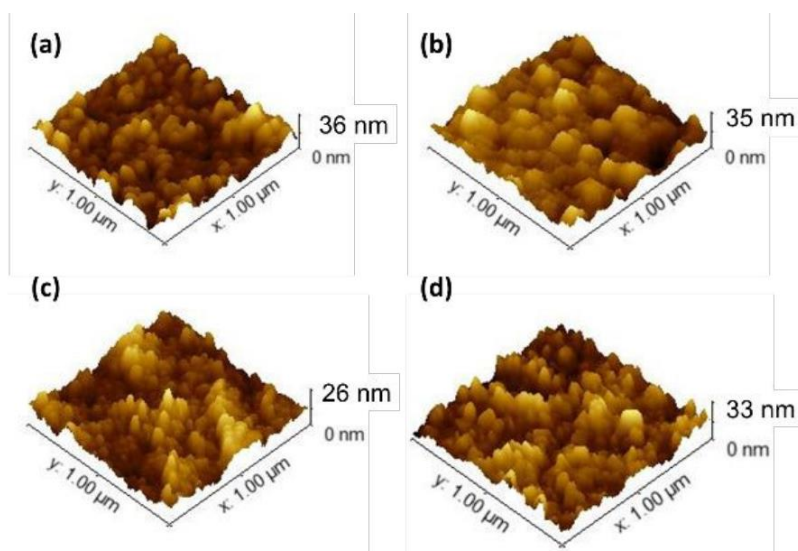
Figure 56 AFM images of the films of ITO/HTM/CsPbBr$_3$ NCs where HTM was: (a) blank, (b) PTAA c) EADR03 and d) EADR04.

ITO/HTMs/NCs	Contact angle (θ)	RMS (nm)	Grain.density (gains.μm^{-2})	Grain Volume (μm^3)
Blank	8.13	5.04	4218	0.069
PTAA	88.15	4.67	3353	0.026
EADR03	50.19	4.13	3494	0.017
EADR04	51.63	4.38	3343	0.019

Table 3 Characterization of the MHP NCs deposited on the top of different HTM/ITO samples: Value of the water contact angle, roughness mean square values (RMS), grain density and volume between the grain surface and the plane, estimated from AFM measurements.

To get more information, we have also analyzed height threshold images shown in figure 57 that reveals the NCs layers are deposited as a bilayer on the SAMs, as a multilayer on bare ITO and as two to three layers on the top of PTAA. The presence of SAMs clearly affects the NCs deposition.
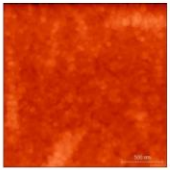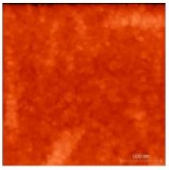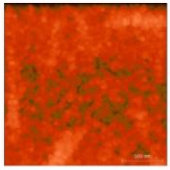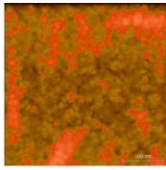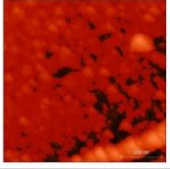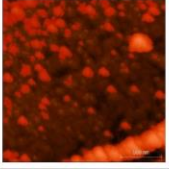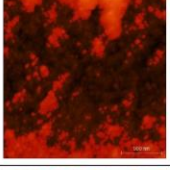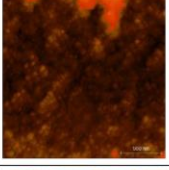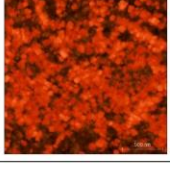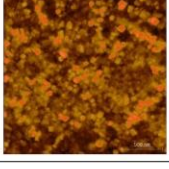
Sample	Threshold 15 nm	Threshold 25 nm	Threshold 40 nm	Threshold 50 nm
BLANK				
PTAA			----	----
EADR03			----	----
EADR04			----	----

Figure 57 Threshold image analysis of the AFM images of the films of ITO/HTM/CsPbBr3 NCs where HTM is blank, PTAA, **EADR03**, and **EADR04**. The
red colour correspond to the masked regions whose height is higher than the threshold
value indicated at the top of each column.

4.3.3 Device Characterization

In our device structure, ITO/SAMs (< 5 nm) or PTAA (10 nm)/CsPbBr$_3$/TPBi (50 nm)/LiF (1nm)/Al (100 nm) the SAMs and PTAA act as hole injection materials, the CsPbBr$_3$ as emissive layer, TPBi as an electron transport material, LiF as a cathode buffer material and Al as an electrode. The reference device, named as Blank, was prepared without the hole transport material following the structure ITO/CsPbBr$_3$/TPBi/LiF/Al. The energy levels of all the materials shown in figure 49b) were taken from the literature.[22] The performance of the devices is shown with the help of figure 58 a), 58 b), 58 c) and table 4. Our devices show different luminance values depending upon different HTMs. The highest luminance was achieved with the devices which has SAM EADR04, followed by EADR03 and then the references with PTAA and without HTM. We have shown the luminance of all devices prepared in different batches collectively to demonstrate the

reproducibility of our results in Fig. 58 c) whereas Figure 59 shows the current efficiency variation with the applied bias. From the table 4, we can see that the devices prepared with SAMs shows the lowest turn on voltage values while the blank devices have highest voltage. On the one hand, HOMO levels of our SAM molecules are in between valence band (VB) of NCs and work function of ITO, which makes it easier to inject holes when compared to PTAA. Also, LUMO levels of our SAMs are higher than the PTAA, suggesting better electron blocking properties which promotes radiative recombination.
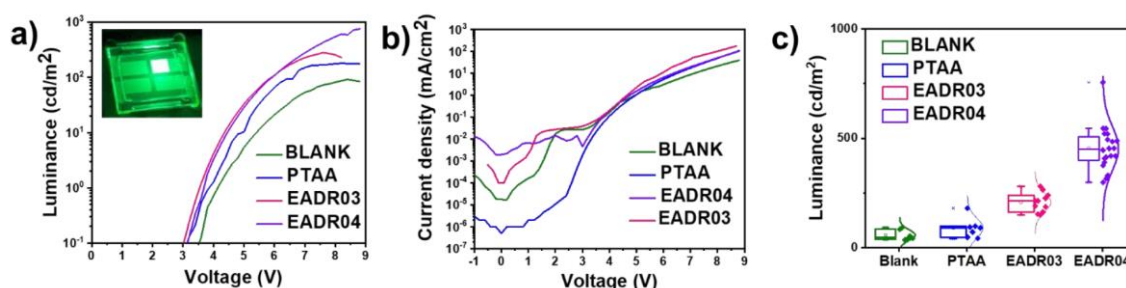
Figure 58 Performance of the PeLEDs prepared with different HTMs: a) Variation of the luminance as a function of the applied bias, b) evolution of the current density with the applied bias; and c) device performance statistics of the luminance values achieved on over 30 devices containing blank, PTAA, **EADR03** and **EADR04**

Table 4 Performance of PeLEDs prepared with different HTMs

HTMs	Maximum Luminance (cd/m^2) [Average values]	Turn-on Voltage[a] V_{on} (V)	Lifetime[b] T_{50}/T_t (s)
Blank	92 [57.5 ± 24.4]	4	4/354
PTAA	180 [89.1 ± 45.9]	3.2	6/596
EADR03	281 [207.2 ± 43.8]	3.1	4/384
EADR04	756 [453.6 ± 101.2]	3.1	11/1157

[a]Turn-on voltage of the devices is the voltage at which devices achieve 0.1 cd/m^2 of luminance.

[b]The lifetime of the devices: T_{50} time range in which luminance decrease to half of its initial value under a constant applied current of 2 mA, T_t is defined as the time range at which the luminance of the devices is higher than 1 cd/m^2 under a constant applied current of 2 mA
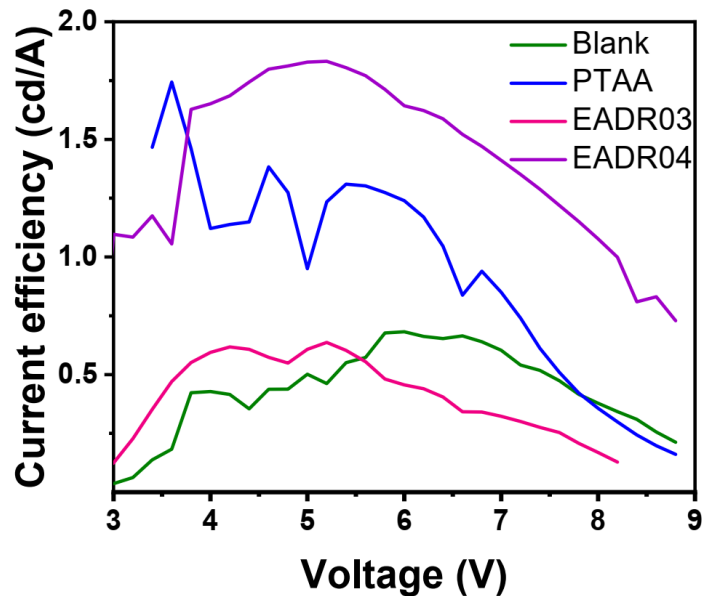
Figure 59 Current efficiency vs. applied bias for the PeLEDs prepared with different HTMs.

The electroluminescence (EL) was recorded after applying a constant voltage of 9 V to our devices which is displayed in Fig 60 a), where we see the EL peak intensity at 517 nm. The EL spectra of the reference devices blank and the devices made with PTAA are identical to their PL measurement which corresponds to the NCs in contrast to the position of EL peaks in case of SAMs has shifted 4 nm in comparison to their PL spectra. Therefore, despite different HTMs, the origin of Electroluminescence is the same in all the devices.

Finally, we have analyzed the operational stability of the devices by applying a constant current of 2 mA and recording the emitted light versus time. The results are shown in table 4. T_t is the total lifetime of devices and can be described as the total time when the devices show brightness higher than 1 cd/m^2. T_{50} is the time for the brightness to decrease to half of its initial value. It is observed from Figure 60 b) normalized luminance decay and Figure 60 c) luminance decay that all the devices show an exponential decrease which is more pronounced in the case of the PTAA. The light emission from the devices with EADR04 decreases slowly and shows the highest operational lifetime 50% higher than PTAA. The operation instability in PeLEDs can be explained in the following ways according to the literature: (i) the initial migration of mobile ions in the MHP NCs towards the local defects induced by applied electrical field, that can generate a transient increase of light emission intensity, that is not observed in these cases[23] , and

(ii) charge injection imbalance leads to charge accumulation at the interface which can promote interfacial degradation[24] (iii) Joule heating due to the heat accumulation at the interface due to undesired electrochemical reactions[25].
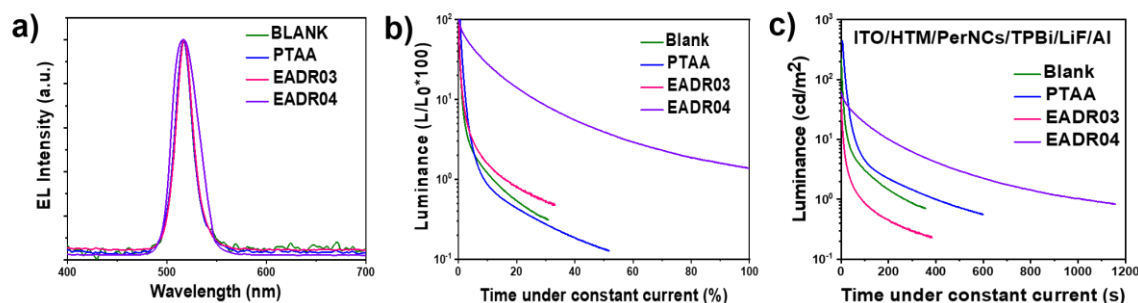
Figure 60 (a) Electroluminescence measured after applying a constant voltage of 9V to PeLEDs prepared with SAMs as HTM and with PTAA and blank; (b) Normalized luminance vs time; (c) operational lifetime recorded under the same conditions displayed using absolute values of luminance

We have also investigated the degradation rate by measuring the current density before and after the lifetime stability measurements. Figure 61 shows the variation of current densities of the devices with different HTMs with applied bias. In Hybrid LEDs, space charge limited current (SCLC) model explains the change in the regime from linear to exponential.[26,27] Due to the better charge transport properties of the HTMs into the emissive layer, electrons are accumulated at the interface. Hence, when the balance in charge injection into the photoactive layer is achieved, the exponential increase of the current density occurs. It happens when the applied voltage reaches a certain voltage called turn-on voltage where the luminance is observed. From our experiments, the devices which have SAMs require lower turn-on voltages for luminance to appear when compared to the devices with PTAA and blank, which suggests good hole injection ability of the SAMs. Again, as shown in figure 61, when after exposing our device to a constant current for lifetime measurements, the current density curve shows a resistive behavior for the devices with EADR03, PTAA and Blank, while for EADR04 the current density behavior was still the same. This phenomenon strongly suggests that the EADR04 molecule can remain un-destroyed for a longer period leading to the better stability of devices.
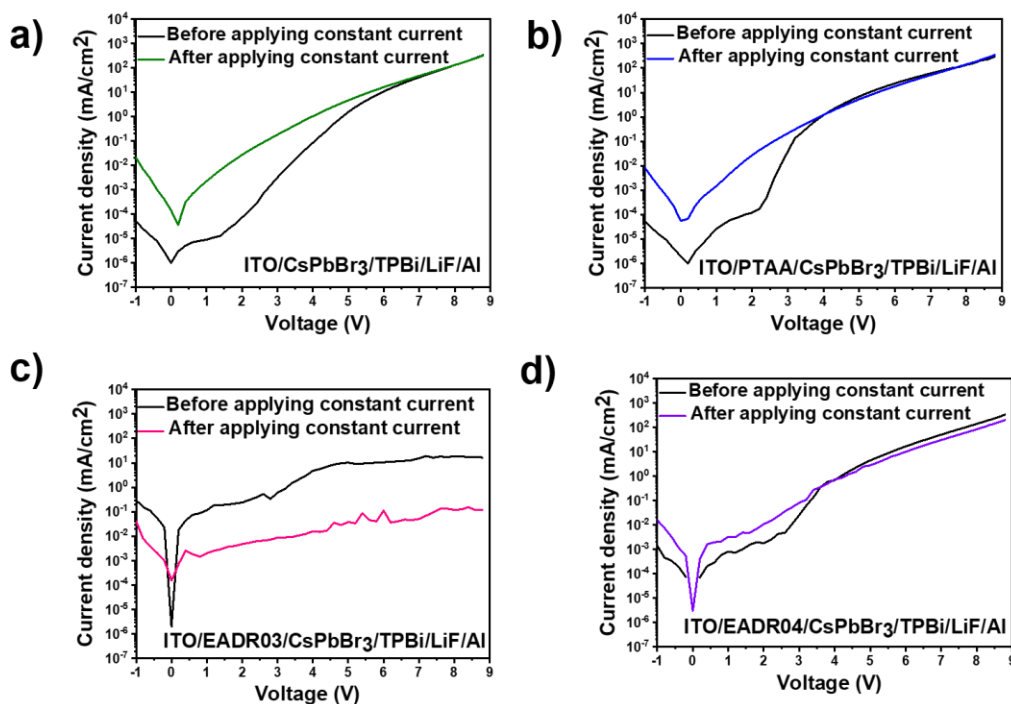
Figure 61 Current density variation with the application of an external bias in devices before and after the measurement of lifetime stability that consist in the application of 2 mA until the luminance decay reaches 1 cd/m^2.

4.4 Conclusions

From our experiments, we have observed that the PeLEDs fabricated with the carbazole-based SAM molecules EADR04 show better performance than the reference devices (the one with PTAA as hole transport material and the blank prepared without any HTM). The investigation demonstrates that, first, the use of both EADR03 and EADR04 SAMs, influence the formation of the films made by the NCs and increase the luminance of the PeLEDs whereas lowering the turn-on voltage due to the enhanced charge injection ability of the SAMs in comparison to PTAA. And second, that the fine tuning of the SAM structure, such as the addition of a second phenyl moiety in the linkage part of the EADR04, enhance the operational stability of the devices due to the increased resistance of the SAM to decomposition induced by operando conditions.

4.5 References

1. Cho, Himchan, et al. "Improving the stability of metal halide perovskite materials and light-emitting diodes." *Advanced Materials* 30.42 (2018): 1704587.

2. Miyasaka, Tsutomu, Akihiro Kojima, and Kenjiro Teshima. "Lead halide perovskites as quantum dot sensitizers for mesoscopic TiO2 photovoltaic cells." *Meeting Abstracts*. No. 9. 2009.

3. Kim, Jin Young, et al. "High-efficiency perovskite solar cells." *Chemical Reviews* 120.15 (2020): 7867-7918.

4. Liang, Aihui, et al. "Highly Efficient Halide Perovskite Light-Emitting Diodes via Molecular Passivation." *Angewandte Chemie International Edition* 60.15 (2021): 8337-8343.

5. Miao, Jianli, and Fujun Zhang. "Recent progress on highly sensitive perovskite photodetectors." *Journal of Materials Chemistry C* 7.7 (2019): 1741-1791.

6. Li, Chenglong, et al. "Ultrafast and broadband photodetectors based on a perovskite/organic bulk heterojunction for large-dynamic-range imaging." *Light: Science & Applications* 9.1 (2020): 31.

7. Zhang, Qing, et al. "Halide perovskite semiconductor lasers: materials, cavity design, and low threshold." *Nano Letters* 21.5 (2021): 1903-1914..

8. Akkerman, Quinten A., et al. "Genesis, challenges and opportunities for colloidal lead halide perovskite nanocrystals." *Nature materials* 17.5 (2018): 394-405.

9. Tan, Zhi-Kuang, et al. "Bright light-emitting diodes based on organometal halide perovskite." *Nature nanotechnology* 9.9 (2014): 687-692..

10. Kim, Young-Hoon, et al. "Comprehensive defect suppression in perovskite nanocrystals for high-efficiency light-emitting diodes." *Nature Photonics* 15.2 (2021): 148-155.

11. Moon, Hyungsuk, and Heeyeop Chae. "Efficiency enhancement of all-solution-processed inverted-structure green quantum dot light-emitting diodes via partial ligand exchange with thiophenol derivatives having negative dipole moment." *Advanced Optical Materials* 8.1 (2020): 1901314.

12. Ye, Fanghao, et al. "Operational and spectral stability of perovskite light-emitting diodes." *ACS Energy Letters* 6.9 (2021): 3114-3131.

13. Li, Junming, et al. "Biological impact of lead from halide perovskites reveals the risk of introducing a safe threshold." *Nature communications* 11.1 (2020): 310..

14. Filippetti, A., et al. "Fundamentals of tin iodide perovskites: a promising route to highly efficient, lead-free solar cells." *Journal of Materials Chemistry A* 9.19 (2021): 11812-11826..

15. Zhang, Baowei, et al. "Stable and size tunable CsPbBr3 nanocrystals synthesized with oleylphosphonic acid." *Nano letters* 20.12 (2020): 8847-8853.

16. Xu, Leimeng, et al. "A bilateral interfacial passivation strategy promoting efficiency and stability of perovskite quantum dot light-emitting diodes." *Nature Communications* 11.1 (2020): 3902..

17. Rana, Aniket, et al. "Hole transport layer influencing the charge carrier dynamics during the degradation of organic solar cells." *Journal of Applied Physics* 125.5 (2019): 053102..

18. Aktas, Ece, et al. "Understanding the perovskite/self-assembled selective contact interface for ultra-stable and highly efficient p–i–n perovskite solar cells." *Energy & Environmental Science* 14.7 (2021): 3976-3985..

19. Zheng, Hongzhi, et al. "Circularly polarized luminescent carbon dot nanomaterials of helical superstructures for circularly polarized light detection." *Advanced Optical Materials* 6.23 (2018): 1801246..

20. Ravi, Vikash Kumar, Ganesh B. Markad, and Angshuman Nag. "Band edge energies and excitonic transition probabilities of colloidal CsPbX3 (X= Cl, Br, I) perovskite nanocrystals." *ACS Energy Letters* 1.4 (2016): 665-671. Nanocrystals. ACS Energy Lett. **1**, 665–671 (2016).

21. Pradhan, Sajan, et al. "Stable lead-halide perovskite quantum dots as efficient visible light photocatalysts for organic transformations." *Nanoscale Advances* 3.5 (2021): 1464-1472.

22. Lu, Yongsheng, et al. "Tuning hole transport layers and optimizing perovskite films thickness for high efficiency CsPbBr3 nanocrystals electroluminescence light-emitting diodes." *Journal of Luminescence* 234 (2021): 117952.

23. Lee, Seungjin, et al. "Versatile defect passivation methods for metal halide perovskite materials and their application to light-emitting devices." *Advanced Materials* 31.20 (2019): 1805244.

24. Wang, Tiantian, et al. "Controllable transient photocurrent in photodetectors based on perovskite nanocrystals via doping and interfacial engineering." *The Journal of Physical Chemistry C* 125.10 (2021): 5475-5484.

25. Dong, Qi, et al. "Operational stability of perovskite light emitting diodes." *Journal of Physics: Materials* 3.1 (2020): 012002.

26. Xu, Lili, et al. "Charge-carrier dynamics and regulation strategies in perovskite light-emitting diodes: From materials to devices." *Applied Physics Reviews* 9.2 (2022): 021308..

27. Lu, Li Ping, Dinesh Kabra, and Richard H. Friend. "Barium hydroxide as an interlayer between zinc oxide and a luminescent conjugated polymer for light-emitting diodes." *Advanced Functional Materials* 22.19 (2012): 4165-4171.

Chapter 5: Small Molecule PDINO as ETLs for CdSe@ZnS Quantum-dot Light Emitting Diodes

Abstract

Cadmium-selenide-based quantum dots have demonstrated their potential in the application of efficient light emitting diodes. However, the performance of the devices is still hindered by appalling device architecture and the charge transport layers. So far, organic solar cells with PDINO as electron transport layers have been demonstrated with more stability and device efficiency. In this work, we have used a small organic PDINO molecule [N, N'-Bis (N, N-dimethylpropan-1-amine oxide) perylene-3,4,9,10-tetracarboxylic diimide] as an electron transport material in the Inverted structured of commercial CdSe@ZnS quantum dots-based light emitting diodes. We observed that by adding PDINO in the cathode side increases the stability of the devices.

5.1 Introduction

After the emerging research about OLEDs (organic light emitting diodes), quantum-dots (discovered in 1980) are the next generation materials for the application in LEDs. The notable research done since last three decades in developing QLEDs with new materials has led to the rapidly expanding QLEDs (Quantum-dot light emitting diodes) market. After investigating out that the optical properties of quantum dots are dependent on their sizes[1,2], their application has become very interesting among researchers. Because of their exceptional properties like colour purity, ability to alter the band gap by tuning their size, various applications in biomedical research[3], solar cells[4], light emitting diodes[5] and Quantum computer[6] etc. are progressing rapidly. The most commonly used Quantum dots are CdSe@ZnS in the light emitting devices since its first application by Covlin et al in 1941[7]. While the research is dedicated towards finding the solutions for efficient devices, we must also consider that to get the optimum performance from the devices, charge transporting layers has as much importance as the active layer.

In QLEDs, SnO_2, ZnO or PEI are the most commonly and widely used electron transporting materials. Zinc oxide (ZnO) NPs are popular in QLEDs because of their high electron mobility[8,9]. But their properties of causing poor shelf stability, less electroluminescence efficiency and positive aging in devices[10] make the ZnO ETL unfit for the application in QLEDs. However, the new Tin-oxide (SnO_2) nanoparticle ETL replaces the former layer from the devices providing the better shelf stability[11]. On the other hand, in the inverted structure of QLEDs, polyethylenimine (PEI) is an extensively used polymer as electron transporting/electron injecting layer. PEI layer is used to balance the charge injection in the devices by lowering the cathode contact´s work function[12] with their intrinsic molecular dipole[13,14]. In spite of this lead, it's intrinsic insulative nature causes the electron injection blocking and hinders the performance of the devices[15]. Thus, more investigation is devoted towards finding the new electron transporting materials which are suitable for the QLEDs.

PDINO carrying *N*-oxide group on perylene-diimide (PDI) is a widely used material as cathode in standard structure of organic and polymer solar cells[16]. Zhang et al in 2014 showed that the PDINO based solar cells had higher efficiency than the reference devices due to π-delocalized planar structures with high electron affinities[17]. Tianyu et al in 2021 demonstrated that the PDINO molecular electron transport layer enhanced the

efficiency of the devices significantly when compared to the SnO_2 NPs ETL by showing surface passivation effects[18].

In this work, we have employed PDINO molecule as an electron transporting material to fabricate the quantum-dot light emitting diodes. The molecular structure of PDINO, the complete architecture of LED devices and the energy level diagram of all the materials used in experiments are shown in Figure 62a), 62b) and 62c) respectively. We have tested the performance of the devices with PDINO as electron transporting layers (ETL) ITO/PDINO and ITO/PDINO/PEI and compared them with the reference devices containing ITO/PEI as ETL. The energy levels of all materials in the figure 62c) were picked from literature e.g., PDINO[19], CdSe@ZnS quantum dots from Cytodiagnostics, PVK[20] and PEDOT: PSS[21].

5.2 Experimental Section

5.2.1 Film Preparation

For understanding the charge transport in our devices, we have prepared the films of ITO/ETL/QDs. The films with different ETLs PEI, PDINO and PEI/PDINO were used for the optical and morphological characterization. The QDs film and different ETL films were deposited with the same deposition condition as fabrication of devices.

5.2.2 Device Fabrication

Indium-doped Tin Oxide (ITO) coated glass substrates (3 mm x 3 mm) with the sheet resistivity of 15 Ω/m^2, purchased from Xinyan Technology Limited were used for the substrate for fabrication of the Quantum dot light emitting diodes (QLEDs). The substrates were cleaned in a few steps with the help of ultrasonicator in the mixture of alkaline cleaning concentrated Hallmanex and DI water, acetone, and two times from isopropanol in sequence of 10 min with each step. Subsequently, the substrates were exposed to Ozone treatment in the UV/Ozone equipment for 30 min in order to clean any possible organic impurities from the top of substrates prior to deposition of any layers. For the inverted structure, the substrates were transferred to N_2 filled glove box for the

spin-coting of electron transporting layer. PDINO was dissolved in methanol with 1 mg/ml concentration and spin coated on the top of ITO with 3000 rpm for 45 sec as an electron transport layer (ETL) with no further annealing to form a very thin layer of ($<$ 5 nm). To obtain the reference devices, 0.2 % PEI was prepared in ethanol solvent and spin coated on the top of ITO or ITO/PDINO with 3000 rpm for 40 sec and annealed at 120 ^{0}C for 15 min as an electron transport layer and an interlayer respectively. Further, CdSe@ZnS colloidal quantum dots (5 mg/ml in toluene) were purchased from "Cytodiagnostics" to use in the devices as emissive material. The quantum dots were spin coated with 1000 rpm for 60 sec followed by annealing at 100 ^{0}C for 20 min as the emissive layer. On the top, Poly(9-vinylcarbazole) (PVK) was dissolved at 10 mg/ml in 1,4 Dioxane and spin coated with 3000 rpm for 45 sec followed by annealing at 120 ^{0}C for 20 min as hole transporting layer. The devices were taken out of the glove box for the deposition of PEDOT: PSS mixed with equal amount of Isopropanol Alcohol (1:1) as a hole injecting layer to reduce the barrier between anode electrode and the quantum dot layer and was deposited with spin speed 4500 rpm for 45 sec and annealed at 150 ^{0}C for 20 min to form a 40 nm thin layer.

To note the point, all the layers, except PEDOT: PSS, were deposited inside the glove box to maintain the film quality and smoothness. At last, 100 nm of Al was thermally evaporated as anode at 1·10^{-6} mbar of pressure to have the complete structure of devices. Some part of these experiments was done at INAM for EQE including EQE and stability measurements. Some sets of devices and films were fabricated by Laia Marín and Maria Méndez for this project.
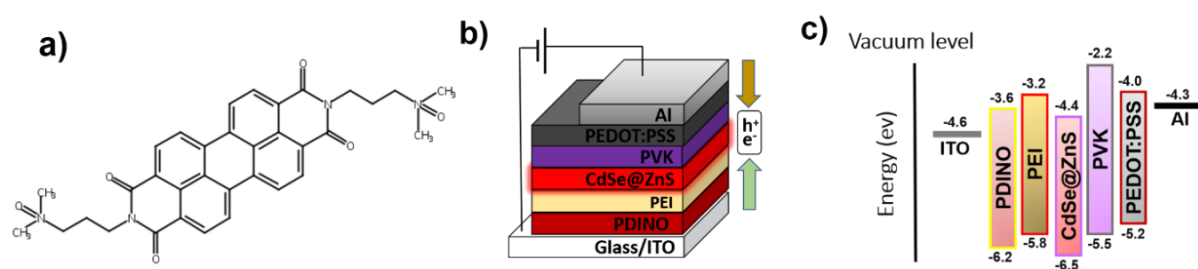
Figure 62 a) PDINO Molecule b) Device structure c) Energy level diagram.

5.3 Result and Discussion

5.3.1 Characterization of Quantum dots

UV-Vis absorption spectra of CdSe@ZnS quantum dots in toluene were measured with toluene as a reference solvent. Absorption spectra shown in in Figure 63 (left) shows two absorption peaks at **636 nm** and **588 nm** which corresponds to the red region of visible spectrum. Fluorescence spectra was carried out within the range of 450-650 nm. From the same Figure, we can see that the quantum dots show a sharp and narrow emission peak at **643 nm** with the FWHM of 33.8 nm. Figure 63 (right) shows the Transmission electron microscopy image where the average size of the particles was observed to measure 5.34 nm.
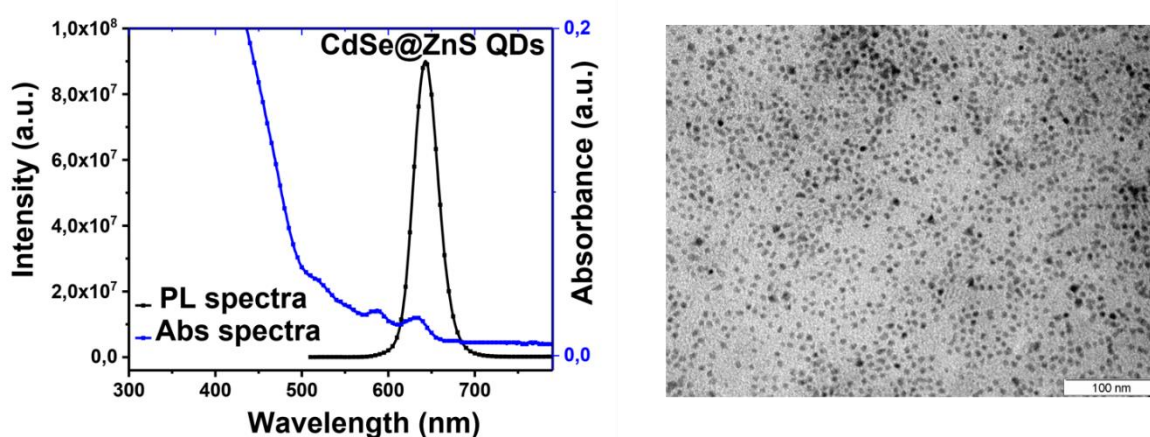
Figure 63 (left) UV-VIS Absorption and PL Spectra (λ_{ext} 500 nm), (right) TEM image of CdSe@ZnS quantum dots.

5.3.2 Characterization of Films

5.3.2.1 Optical Characterization

Figure 64 shows the optical characterization of the films with different ETLs which were used in our devices. From emission spectra (excitation wavelength 590 nm) we can observe that the PDINO only film has the emission peak at 644 nm with FWHM of 32 nm. The emission peak is the same at 644 nm for the films of only QDs with FWHM of 27.2 nm. On the other hand, when we deposit PEI layer on the top for films PDINO/PEI,

the emission peak blue-shifts with 2 nm to make it at 642 nm with FWHM 25.5 nm and blue shifts further 1 nm more when in the case of only PEI films which is at 641 nm with FWHM 25 nm. Figure 64 a) shows the absorption spectra of all the films. We can observe from the figure that absorption peak of PDINO only film is at 380 nm which is again same as the absorption peak of only QDs. On the other hand, we deposit PEI on the top of PDINO, the absorption red shift with 35 nm while peak observed at 415 nm which red shifts with 2 nm in the case of only PEI film which is at 417 nm. Table 5 shows the values from UV-VIS and PL spectra of the films mentioned.
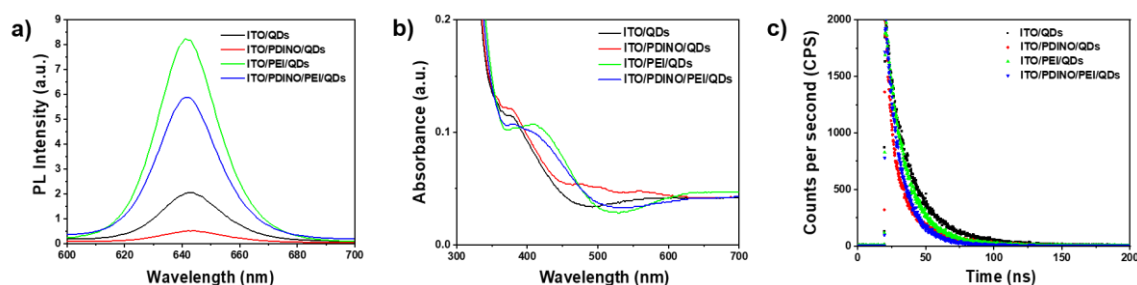
Figure 64 a) Absorbance spectra b) PL spectra after excitation at 590 nm, c) Fluorescence time decay of the samples measured after excitation at 405 nm at constant counts 2K

Table 5 UV-VIS and PL spectra summary table of films ITO/ETL/QDs

ITO/ETLs/QDs	Absorption Peak (nm)	Emission Peak (nm)	FWHM (nm)
No ETL	380	644	27.2
PDINO	380	644	32
PDINO/PEI	416	642	25.5
PEI	420	641	25

TCSPC measurements were done on the films of ITO/ETLs/QDs to understand the recombination trend in our devices. The films were measured in 2000 counts per second which are shown in figure 64 c) and the values of the radiative lifetimes are shown in table 6. From the table, we can observe that the average lifetime in the films which has PEI as ETL is the lowest and this tendency increases when we use PDINO in the films with PDINO/PEI and only PDINO as ETL. On the other hand, films with no ETL have the highest radiative lifetime. Overall, these values coincide with our device results and PEI has the better charge transport ability.

Table 6 Average fluorescence lifetime decays (τ_{av}), lifetime values (τ) and weighting coefficients for each decay channel (A) for the films prepared ITO/ETL/QDs

ITO/ETLs/QDs	τ_{av} (ns)	τ_1 (ns)	A_1 (%)	τ_2 (ns)	A_2 (%)
No ETL	23.6	10.47	29.26	25.03	70.74
PDINO	21.6	5.46	34.03	23.23	65.97
PDINO/PEI	13.7	7.82	33.66	15.13	66.34
PEI	17	10.79	39.53	19.46	60.47

5.3.2.2 Morphological Characterization

The Atomic Force Microscopy images, figure 65, show the interface qualities of the electron transport layers to the quantum dot layers in the devices. The ITO/PDINO/QDs film shows more roughness than the ITO/PDINO/PEI/QDs and ITO/PEI/QDs films (Table 7) which also contributes the rough interfaces between the ETL and the emissive layers explaining the worse electron injection possibility through the cathode.
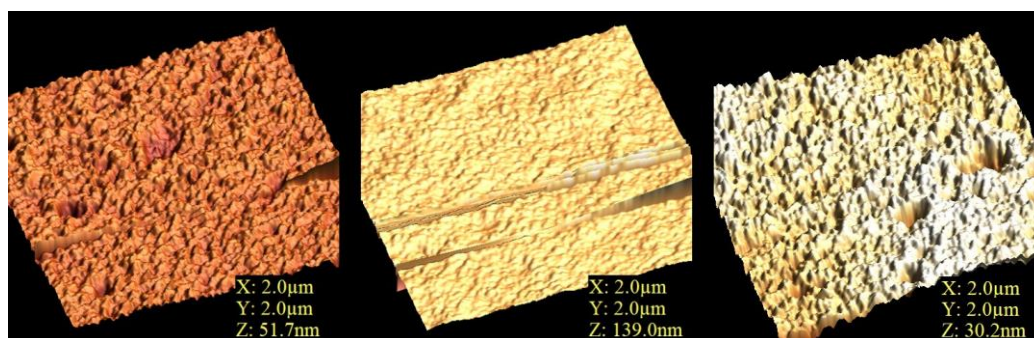
Figure 65 AFM Images of the films ITO/PDINO/PEI/QDs, ITO/PDINO/QDs and ITO/PEI/QDs

To understand the interfaces further, we have performed Contact angle measurements on our films which are shown in Figure 66 and were measured with water. Table 7 shows that all the films are hydrophilic. The hydrophilicity of films with only PDINO as ETL is least in comparison to PDINO/PEI and PEI which has the lowest contact angle. This data suggests that the films with ITO/PDINO layer have less ability to let the QDs layer spread properly on the top of PDINO layer in which enhances when we use PEI on the top of PDINO in ITO/PDINO/PEI layers and ITO/PEI.
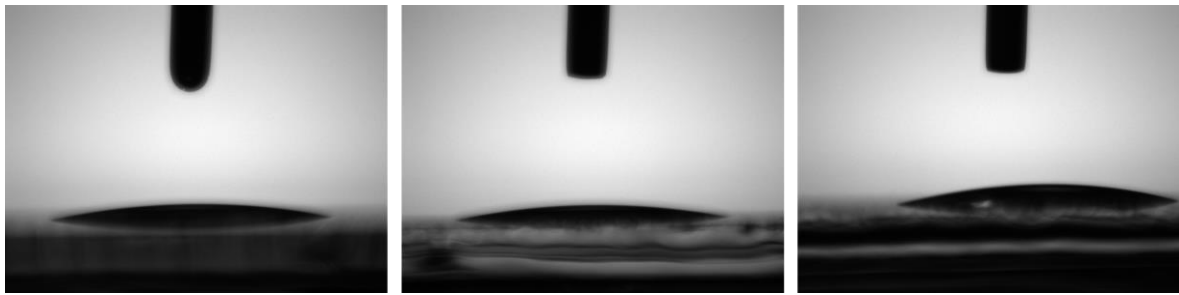
Figure 66 Contact angle a) ITO/PDINO/PEI/QDs b) ITO/PDINO/QDs c) ITO/PEI/QDs

Table 7 Morphological Characterization summary of the films ITO/ETLs/QDs

ITO/ETLs/QDs	Contact Angle (θ)	RMS roughness (nm)
PEI	12.5	2.21
PDINO	19.8	4.15
PDINO/PEI	13.2	2.72

5.3.3 Characterization of devices

The devices were measured by applying a voltage range of -1 v to 15 V at ICIQ. Our reference devices with structure ITO/PEI/CdSe@ZnS/PVK/PEDOT: PSS/Al shows the maximum luminance values of 2960 cd/m^2 at a turn-on voltage of 7.3 V, while the maximum luminance recorded from the devices with structure ITO/PDINO/PEI/CdSe@ZnS/PVK/PEDOT:PSS/Al and ITO/PDINO/CdSe@ZnS/PVK/PEDOT:PSS/Al were 1238 cd/m^2 and 896.7 cd/m^2 at the turn-on voltages of 7.4 V and 8.6 V, respectively. The results are shown in Figure 67 and table 8. Hence, large voltage is required to induce radiative recombination in the emissive layer when PDINO is used. When a thin layer of PEI ($<$ 5 nm) was spin-coated at the top of PDINO (in the devices with ITO/PDINO/PEI cathode), the performance of the devices is more similar to devices prepared with PEI only than PDINO only.
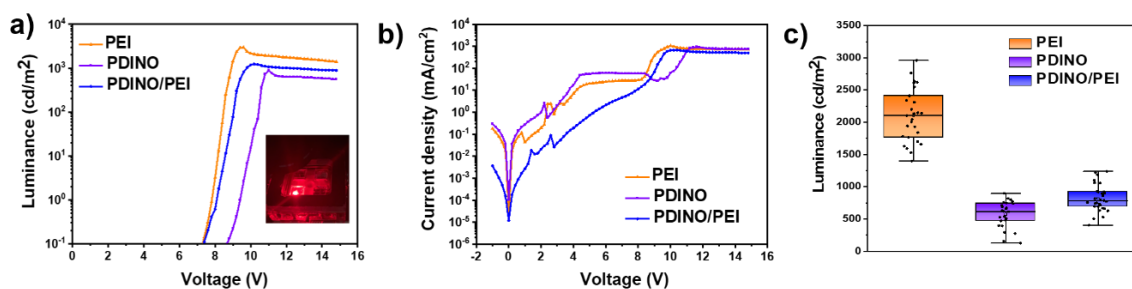
Figure 67 Performance of red QDLEDs with different ETLs a) Luminance vs applied bias b) Current density vs applied bias c) Luminance statistics of devices on over 25 devices

Table 8 Performance table of red QLEDs

ITO/ETMs/QDs	Maximum Luminance (cd/m^2) [Average values]	Turn-on Voltage[a] V_{on} (V)
PEI	2960 [2102 ± 412]	7.3
PDINO/ PEI	1238 [819 ± 208]	7.4
PDINO	896.7 [574 ± 203]	8.6

[a]Turn-on voltage of the devices is the voltage at which devices achieve 0.1 cd/m^2 of luminance.

In a typical QDLED, electron injection is always more efficient than hole injection and that is because the HOMO level of most widely used HTMs are around 5 – 5.5 ev which is far than the valence level of QDs (> 6ev), so it requires to balance the carrier injection within device [22].

Therefore, in order to further optimize the device architecture, we have replaced the anode side from PEDOT: PSS/Al to MoO$_3$/Ag and MoO$_3$/Au in the devices. We have found that the overall device performances with these hole transporting layers were not as good as our usual combination of layers PEDOT: PSS/Al. In MoO$_3$/Au based devices PDINO ETL shows higher luminance in when compared to the PEDOT: PSS/Al based devices, but they were not very economic friendly because of the use of Gold. Figure 68 and Table 9 shows the statistics of device performances with the different anode and cathode sides.
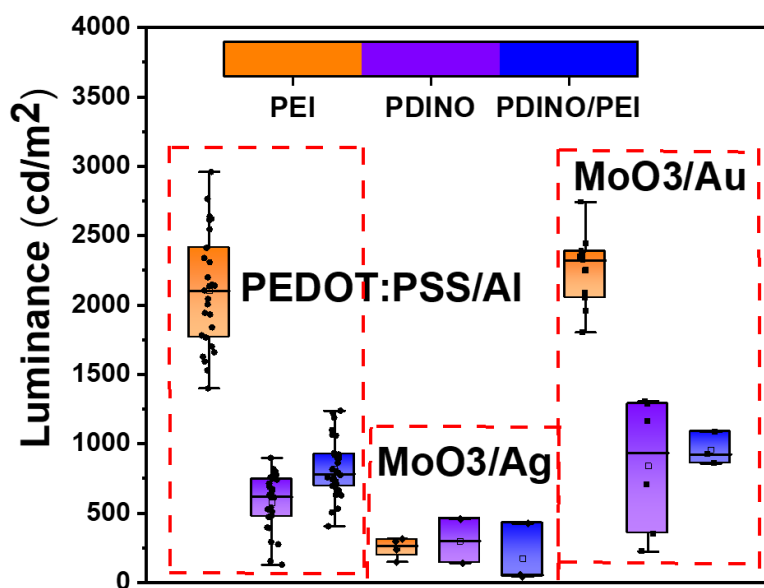
Figure 68 Statistical graph for the different ETL and Anode electrodes of red QLEDs

Table 9 Performance table of the QLEDs with different Anode and Cathode sides

Devices with different ETL side	Max Luminance (cd/m^2)		
	[Average values] of the devices with different Hole transporting electrodes		
	PEDOT: PSS/Al	MoO$_3$/Ag	MoO$_3$/Au
ITO/PEI /QDs	2960 [2102 ± 412]	314 [248 ± 75]	2742 [2250 ± 260.2]
ITO/ PDINO/QDs	896.7 [574 ± 203]	456 [298 ± 223]	1306 [839 ± 481]
ITO/ PDINO/ PEI/QDs	1238 [819 ± 208]	425 [174 ± 217]	1085 [955 ± 117]

Thus, we have introduced a 23 nm thin layer of fullerene C$_{60}$ donor as hole blocking layer between the PDINO and PEI in our devices. For that, thin (23 nm) C$_{60}$ layer was deposited by manual thermal evaporation at the rate of 15-20 kA/s at pressure values of $1\cdot10^{-6}$ mbar. C$_{60}$ layer not only block the holes to go from valence band of the QDs to the HOMO level of ETL; but also acts as barrier for the electron injection from LUMO levels of the ETLs. From the Figure 69 we observed that the devices show overall very lower luminance which, further couldn't be a better architecture for our devices. From our experiments we found that the ITO/PEI based LEDs were the best in exhibiting light.
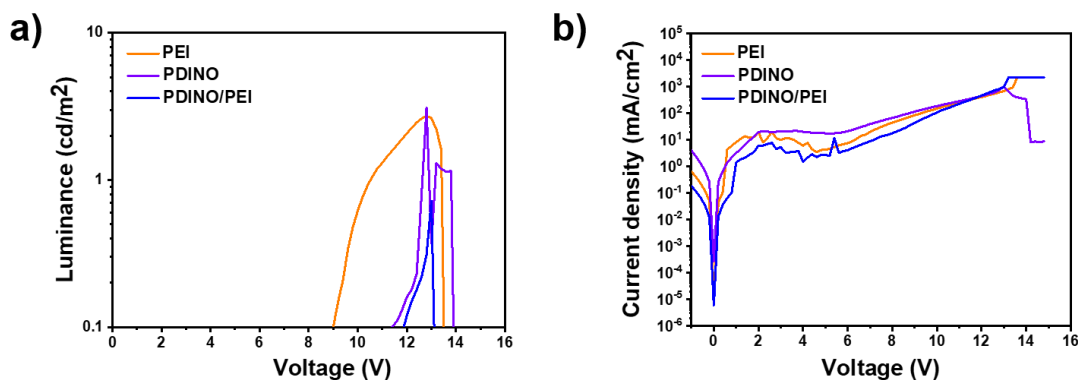
Figure 69 Performance of QDLEDs C_{60} as an interlayer in the device structure ITO/ETLs/C_{60}/QDs/PVK/PEDOT: PSS/Al with different ETLs a) Luminance vs applied bias b) Current density vs Applied bias

As we know that the best architecture is not the optimum in order to optimize the structure further, we examined the electroluminescence stability of our devices. For that, a constant current of 15 mA was applied, and the electroluminescence was recorded with the time. Figure 70 a) shows that the ITO/PEI based devices, which were the best in showing luminance has the minimum Half-lifetime (T_{50}) of 36 sec. T_{50} is defined as the amount of time taken by devices to reach the half of their initial electroluminescence values. On the other hand, devices with the ETLs of ITO/PDINO/PEI and ITO/PDINO shows the operational stability of 46 sec and 53 sec respectively which is shown in Table 10. The reproducible results of our stability measurements explain that the introduction of the PDINO layer in QLEDs makes devices more stable in comparison to the reference devices.

The electroluminescence spectra were measured of the devices of three configuration. From figure 70 b) we observed that the devices with cathode side of ITO/PEI shows a sharp EL peak at 658 nm which is a 15 nm red shift in comparison to the PL emission spectra of QDs, while the devices with ITO/PDINO/PEI and ITO/PDINO exhibit EL peaks at 659 nm and 663 nm respectively accounting for a red shift of 16 nm and red shift of 20 nm to QDs emission respectively. Since, the polymer PEI also has a fluorescence, the devices with ITO/PEI and ITO/PDINO/PEI cathode shows a weak signal from PEI at 429 nm in the EL vs wavelength spectra. To observe better the performance of our devices, the external quantum efficiency (EQE) measurements were performed. Figure 70 c) shows that the reference devices show maximum EQE of 2.9%, where the devices with ITO/PDINO/PEI and ITO/PDINO shows relatively lower EQE of 2.2% and 1.1% respectively.
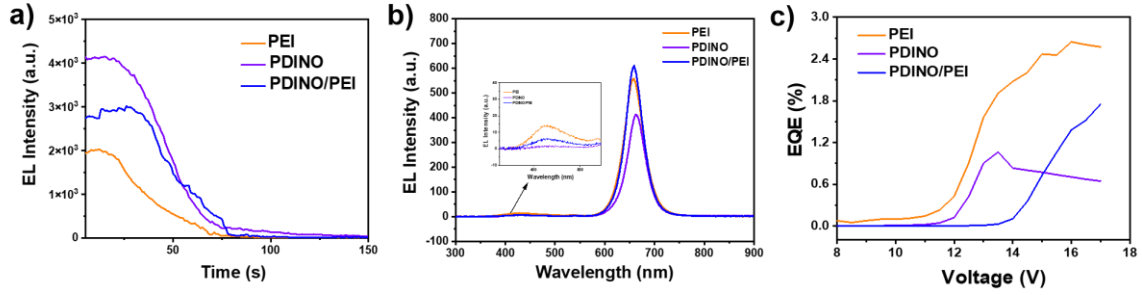
Figure 70 a) Operational Stability Curve measured at constant 15 mA current b) Electroluminescence spectra c) External Quantum Efficiency (EQE) of the QLEDs with different ETLs

Table 10 Electroluminescence lifetime of the QLEDs at constant current density with different cathode sides

ITO/ETMs/QDs	Initial EL	Half EL	EQE (%)	[b]Half- Lifetime T_{50} (sec)
PEI	1982	991	2.9	36
PDINO/ PEI	2734	1367	2.3	53
PDINO	4399	2199	1.1	46

[b] Half-lifetime of the devices is defined as the time range at which the electroluminescence of the devices reaches to half of its initial value under a constant applied current.

To understand the electron transport better in our devices, we performed electron charge mobility measurements in the QDLEDs of structure ITO/ETL/QDs/TPBi/LiF/Al where PDINO and PEI were used as ETLs, and the reference were ITO/QDs based devices. The procedure to build electron only devices is included in **chapter 3**.

For that, we have calculated the trap density and the electron mobility average values of the three configurations devices which are stated below in following table 11. As we can see, PEI based devices have the highest trap density which suggests there are high traps present at the interface of ETL/QDs due to the materials quality. It is lower in the devices with PDINO which reinforce the hypothesis that; as we know that there is more efficient electron flow in comparison to holes as usual in QDLEDs[23], the more trap states present at this interface, the more balance is the charge injection is in the devices. Hence, there is more luminance from the devices with PEI in comparison to PDINO.

Table 11 Trap density and Electron mobility calculated from electron only LEDs

Device with ETL	N_{traps} Average (cm 3) [standard deviation]	Mobility Average (cm^2/V·s) [standard deviation]
ITO/QDs	$1.9 \cdot 10^{17} \pm 2.2 \cdot 10^{16}$	
ITO/PDINO/QDs	$1.1 \cdot 10^{17} \pm 5.2 \cdot 10^{16}$	$6.6 \cdot 10^{-6} \pm 3.10^{-6}$
ITO/PEI/QDs	$2.2 \cdot 10^{17} \pm 1.5 \cdot 10^{16}$	-

5.4 Conclusion

From our study, we have found that the organic molecule PDINO is a functional electron transport material for CdSe@ZnS quantum dot-based light emitting diodes. While the Luminance of the devices with introduction of PDINO has decreased, the operation stability is increased when compared to our reference devices. Overall, thin electron transporting layers and the Quantum-dot layers aids in achieving thin sized QLEDs and promotes less material consumption.

5.5 References

1. Neeleshwar, S. *et al.* Size-dependent properties of CdSe quantum dots. *Phys. Rev. B - Condens. Matter Mater. Phys.* **71(20)**, 201307 (2005).

2. Heath, J. R., Shiang, J. J. & Alivisatos, A. P. Germanium quantum dots: Optical properties and synthesis. *J. Chem. Phys.* **101(2)**, 1607–1615 (1994).

3. Wagner, A. M., Knipe, J. M., Orive, G. & Peppas, N. A. Quantum dots in biomedical applications. *Acta Biomater.* **94**, 44–63 (2019).

4. Kim, M. R., & Ma, D. Quantum-dot-based solar cells: recent advances, strategies, and challenges. *The journal of physical chemistry letters*, *6(1)*, 85-99, (2015).

5. Moon, H., Lee, C., Lee, W., Kim, J. & Chae, H. Stability of Quantum Dots, Quantum Dot Films, and Quantum Dot Light-Emitting Diodes for Display Applications. *Adv. Mater.* **31(34)**, 1–14, 1804294, (2019).

6. Ladd, T. D. *et al.* Quantum computers. *Nature* **464(7285)**, 45–53 (2010).

7. Colvin, V. L., Schlamp, M. C. & Alivisatos, A. P. Light-emitting diodes made from cadmium selenide nanocrystals and a semiconducting polymer. *Nature* **370(6488)**, 354–357, (1994).

8. Kirkwood, N., Singh, B. & Mulvaney, P. Enhancing Quantum Dot LED Efficiency by Tuning Electron Mobility in the ZnO Electron Transport Layer. *Adv. Mater. Interfaces* **3(22)**, 1600868, (2016).

9. Pearton, S. J. & Ren, F. Advances in ZnO-based materials for light emitting diodes. *Curr. Opin. Chem. Eng.* **3**, 51–55 (2014).

10. Wang, Y., Zhu, X., Xue, X., Chi, X., Wang, R., & Ji, W. Electron transport mechanism in colloidal SnO2 nanoparticle films and its implications for quantum-dot light-emitting diodes. *Journal of Physics D: Applied Physics*, *55(37)*, 374004, (2022).

11. Chen, M. *et al.* Highly Stable SnO 2 -Based Quantum-Dot Light-Emitting Diodes with the Conventional Device Structure. *ACS Nano* **16(6)**, 9631-9639, (2022)

12. Cun, Y. *et al.* All-solution processed high performance inverted quantum dot light emitting diodes. *J. Mater. Chem. C* **8(12)**, 4264–4270 (2020).

13. Gu, W. *et al.* Silicon-Quantum-Dot Light-Emitting Diodes with Interlayer-Enhanced Hole Transport. *IEEE Photonics J.* **9(2)**, 1–10 (2017).

14. Kim, Y. H. *et al.* Polyethylene imine as an ideal interlayer for highly efficient inverted polymer light-emitting diodes. *Adv. Funct. Mater.* **24(24)**, 3808–3814, (2014).

15. Ding, K. *et al.* Polyethylenimine Insulativity-Dominant Charge-Injection Balance for Highly Efficient Inverted Quantum Dot Light-Emitting Diodes. *ACS Appl. Mater. Interfaces* **9(23)**, 20231–20238 (2017).

16. Bin, H. *et al.* 11.4% Efficiency non-fullerene polymer solar cells with trialkylsilyl substituted 2D-conjugated polymer as donor. *Nat. Commun.* **7(1)**, 13651, (2016).

17. Zhang, Z. G. *et al.* Perylene diimides: A thickness-insensitive cathode interlayer for high performance polymer solar cells. *Energy Environ. Sci.* **7(6)**, 1966–1973, (2014).

18. Kong, T., Wang, R., Zheng, D. & Yu, J. Modification of the SnO2 Electron Transporting Layer by Using Perylene Diimide Derivative for Efficient Organic Solar Cells. *Front. Chem.* **9**, 703561, (2021).

19. Amusan, O. O., Louis, H., -Uz-Zafar, S., Hamzat, A. T. & Peter, D. M. Chemical Methodologies Different Interface Engineering in Organic Solar Cells: A Review. *Chem. Methodol.* **3**, 425–441 (2019).

20. Lan, L. *et al.* Preparation of efficient quantum dot light-emitting diodes by balancing charge injection and sensitizing emitting layer with phosphorescent dye. *J. Mater. Chem. C* **7(19)**, 5755–5763, (2019).

21. Lessmann, R. & Hümmelgen, I. A. Thin copolymer-cased light-emitting display made with fluorine-foped tin oxide substrates. *Mater. Res.* **7**, 467–471 (2004).

22. Park, M. *et al.* Improved performance of quantum dot light emitting diodes by using charge blocking layer. *Dig. Tech. Pap. - SID Int. Symp.* **45**, 1309–1311 (2014).

23. Zhang, X. *et al.* Energy Level Modification with Carbon Dot Interlayers Enables Efficient Perovskite Solar Cells and Quantum Dot Based Light-Emitting Diodes. *Adv. Funct. Mater.* **30**, 1–9 (2020).

Chapter 6: Enhanced performance of perovskite light emitting diodes by the doping of Dysprosium

Abstract

Halide perovskite are the new and emerging materials for the application in light emitting diodes. For increasing the efficiency of PeLEDs, perovskite doping has been one of the effective techniques. In this chapter, we have described the effect of doped $MAPbBr_3$ perovskite with Dysprosium rare earth element at different concentrations in our PeLEDs. We have found that when a small concentration of Dysprosium (Dy^{3+}) is added to the commonly used perovskite $MAPbBr_3$ for LEDs application, the device performance has increased in comparison to the pristine devices.

6.1 Introduction

In recent years, metal halide perovskite (MHPs) semi-conducting materials have drawn a huge attention due to their application in photovoltaic technologies, photodetectors, LASERs and in Light emitting diodes (LEDs). Perovskite materials (ABX_3) are easily processable at low cost by different processing technologies. In addition, band gap tunability, high absorption coefficients and narrow emission spectra (full width at half maximum ≈ 20 nm)[1], small excitonic binding energy (few tens of meV in lead halide perovskites)[2], long diffusion length (over 1 μm in thin films or nano structures and >100 μm in single crystals)[3], like optoelectronic properties makes the material very interesting among researchers. Since their first LED application in 2014 when Zhi-Kuang Tan et al reported green LEDs with EQE of 0.1%,[4] research has been expanding more in the field to develop perovskite light emitting diodes.

With the developing research, among many strategies followed to optimize the application of MHPs in the LEDs, as they are economically viable in comparison to the OLEDs, several structures have been tested i.e., use of organic-inorganic perovskites, mixed halide perovskites [5], mixed triple cation perovskites [6] etc., In addition, an in order to overcome the challenge of toxicity because of the presence of carcinogenic element Lead (Pb) in the most efficient devices, lead-free perovskites have been explored for the LED applications i.e., Pb^{+2} has been replaced by Sn^{+2} [7]. On the other hand, researchers found that by altering the dimensionality of the perovskites can alter their optical properties. Byun et al in 2016 showed that the quasi-2D perovskites mixed 2D/3D perovskites have increased the efficiency of the PeLEDs and increased the luminescent properties of the perovskites [8]. Further Fakharuddin et al in 2019 suggested that the application of 2D/3D perovskite based emissive layer increased the stability of the devices by reducing the roll-off efficiency [9].

Regarding the 0-D perovskites, the success in developing PeLEDs based upon perovskite Quantum Dots can be shown through the reports published by Protesescu et al in 2015 [10] because of materials high colour purity/tunability and narrow spectral width. The performance of Perovskite quantum dot-based LEDs has grown by some strategies to improve the photoluminescence quantum yield (PLQY) like use of long chain ligands [11] or mixed halide quantum dots etc. [12] After applying such low dimensional perovskite

materials in LEDs, researchers Zhe Liu et al achieved recently the breakthrough with very high EQE of more than 28.1% published in 2021 [13].

In spite of all the advantages with perovskite materials in LEDs, devices operational stability (due to ion migration most importantly and intrinsic phase instability) still lag behind the OLEDs which further limits them from practical use. Various reports suggest that the partial doping of B-site cation can reduce the defect density and, hence, reduce ion migration that in turns to increased operational stability of PeLEDs. Monovalent (K^+, Rb^+) [14], divalent (Mn^{2+}, Zn^{2+}, Cd^{2+}, Co^{2+}, Cu^{2+}, Sr^{2+}, Sn^{2+}, Ni^{2+}, Ge^{2+}) [15], trivalent (Sb^{3+}, Bi^{3+}, Al^{3+}, Y^{3+}) [16] and trivalent lanthanide cations (Ce^{3+}, Tb^{3+}, Yb^{3+}) [17] have been reported to improve the performance of MHPs in the perovskite LEDs. In recent years, Lanthanide Rare earth (RE) ions doped perovskites have received more attention for their potential application in photovoltaics and light emitting diodes [18]. Zhou et al in 2017 reported that the thermal stability and optical performance of Mn^{+2} doped $CsPbX_3$ perovskite nanocrystal improved making of it an efficient candidate for the LED application [19].

After few months, Pan et al published a report where they doped $CsPbCl_3$ nanocrystals with different lanthanide ions (Ce^{3+}, Sm^{3+}, Eu^{3+}, Tb^{3+}, Dy^{3+}, Er^{3+}, and Yb^{3+}) and found the increased Photo luminescence quantum yield (PLQY) with expanding the emission from visible region to NIR spectral region. They suggested that the lanthanide doped perovskites can play an important role with good magnetic and electric properties [20]. In 2018 Meenu Venugopal et al investigated that Dysprosium (Dy) and Samarium (Sm) co-doped calcium zirconated perovskite $CaZr_{0.9}Sm_{0.025}Dy_{0.075}O_3$ system was a potential material for the white light LED application. They achieved pleasant white light at 354 nm excitation with CIE coordinates (0.3310, 0.3349) [21]. Because of their luminescent properties Dysprosium element has been used interestingly for the LED applications [22].

In this work, we have studied the impact of Dysprosium ion (Dy^{3+}) doping in $MAPbBr_3$ perovskite as emissive layer for PeLEDs. In the bulk perovskite, we have fabricated the devices with the structure shown in Figure 71 a) of ITO/PEDOT: PSS/$MAPb_xDy_{1-x}Br_3$/TPBi/LiF/Al to find out the effects of different doping concentration on the devices. The energy levels of all the materials used in the experiments are shown in Figure 71 b).
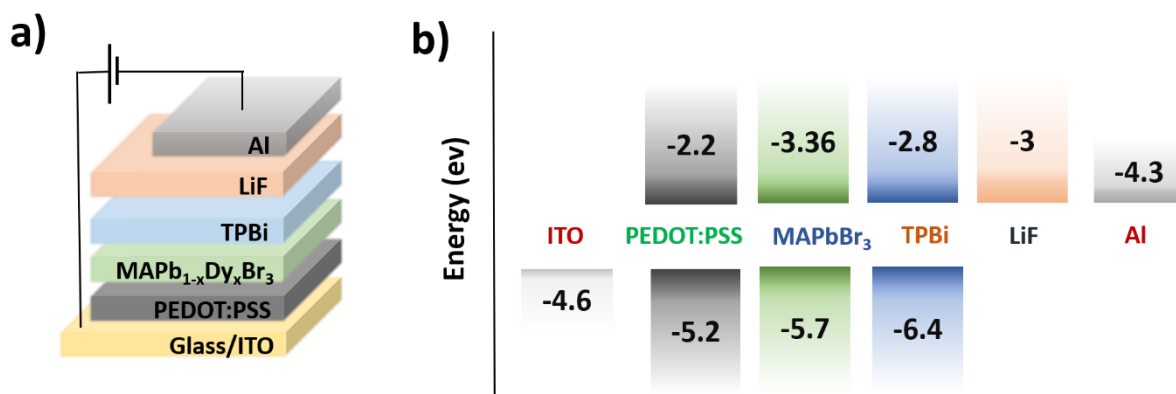
Figure 71 a) Device Architecture b) Energy level diagram of the materials used in devices.

6.2 Experimental Section

6.2.1 Preparation of MAPb$_x$Dy$_{1-x}$Br$_3$ perovskite

All the perovskite solutions were prepared with 1:24 molarity in the solvent of DMSO: DMF of 1:4. For pristine devices, 34.7 mg of methyl ammonium bromide (MABr) and 113.78 mg lead bromide (PbBr$_2$) were mixed to the solvent mixture of DMF: DMSO with the ratio of 1:4. The dysprosium nitrate Dy (NO$_3$)$_3$ dopant was added into the MABr and PbBr$_2$ mixture according to the wt % of 1%, 3%, 5%, and 10%. To obtain the perovskite solution with 1 % Dy doping i.e., MAPb$_{0.99}$Dy$_{0.01}$Br$_3$, 1.14 mg Dy (NO$_3$)$_3$, 112.31 mg PbBr$_2$ and 34.7 mg MABr was added into the solvent mixture. Similarly, other concentration of doped PSKs were prepared by mixing Dy (NO$_3$)$_3$ and PbBr$_2$ in the corresponding wt% to mix with MABr and finally dissolve in the DMF: DMSO solvent mixture. With this process, MAPb$_{0.99}$Dy$_{0.01}$Br$_3$, MAPb$_{0.97}$Dy$_{0.03}$Br$_3$, MAPb$_{0.95}$Dy$_{0.05}$Br$_3$, and MAPb$_{0.9}$Dy$_{0.1}$Br$_3$ were prepared.

6.2.2 Preparation of Perovskite Films

To study the charge behaviour of the doping in perovskites, we have prepared the films of ITO/PEDOT: PSS/PSK with different doping concentrations. Films were prepared with same deposition condition of PEDOT: PSS and perovskites as in the devices. The films were used for morphological characterization. On the other hand, in the films used for optical characterization, we have deposited on the top the PMMA with concentration 0.25 mg/mL in Chlorobenzene at 5000 rpm for 20 s followed by annealing at 100 ºC for 5 min.

6.2.3 Device Fabrication

Indium-doped Tin Oxide coated glass substrates (1.5 cm x 1.5 cm) with the sheet resistivity of 15 Ω/m^2, purchased from Xinyan Technology Limited were used as Anode electrode for our devices. Subsequent cleaning of ITO was done with the conventional method of cleaning for 10 minutes each in ultrasonication with the steps of Soap-DI water, DI water, acetone, two times with IPA. The substrates were then treated with UV-Ozone for 20 minutes to remove possible organic contaminations prior to any deposition. The PEDOT: PSS layer was spin-coated in ambient conditions as hole-transporting layer in 2 steps 4500 rpm and 3000 rpm for 45 s and 30 s respectively and annealed at 150 ^0C for 15 min to form the film of 35 nm. After that, films were carefully transferred to the nitrogen filled glove box for further deposition of layers. Perovskite layer was deposited at 6000 rpm for 60 sec at 2000 rpm/s and annealed at 100 ^0C for 1 hr. The thickness of the film is around 50 nm. TPBi {2,2',2''-(1,3,5-Benzinetriyl) -tris(1-phenyl-1-H-benzimidazole)} was thermally evaporated as an electron transporting layer on the top of perovskite layer forming a 50 nm thin film. 0.8 nm of LiF was evaporated as a buffer layer on the top of TPBi, followed by 100 nm film of Aluminium (Al), deposited as the cathode electrode to complete the device fabrication. All the thermal evaporation was done at the base pressure of $1x10^{-6}$ mbar. All in all, the active area of our devices was 3 mm x 3 mm.

To be noted, PEDOT: PSS layer was deposited outside of the N_2 filled glove box.

6.3 Result and Discussion

6.3.1 Film Characterization

6.3.1.1 Optical Characterization

Figure 72 a) shows the absorption spectra of different perovskite films. We can observe that the films of $MAPbBr_3$ perovskite shows an absorption peak at 522 nm. The perovskite films of $MAPb_{0.99}Dy_{0.01}Br_3$, $MAPb_{0.97}Dy_{0.03}Br_3$, $MAPb_{0.95}Dy_{0.05}Br_3$, and $MAPb_{0.9}Dy_{0.1}Br_3$ shows absorption peaks at 523 nm, 524 nm, 522 nm and 524 nm respectively which is the red shift of 1 nm, 2 nm, no red shift and 2 nm respectively in comparison to the pristine film. The red shift implies a decrease in band gap and more

prominent to the traps. Figure 72 b) shows the PL spectra of all the perovskite films. The emission peaks of $MAPbBr_3$, $MAPb_{0.99}Dy_{0.01}Br_3$, $MAPb_{0.97}Dy_{0.03}Br_3$, $MAPb_{0.95}Dy_{0.05}Br_3$, and $MAPb_{0.9}Dy_{0.1}Br_3$ are at 533 nm, 534 nm, 533 nm, 541 nm and 533 nm respectively. The emission spectra of films of $MAPb_{0.99}Dy_{0.01}Br_3$, and $MAPb_{0.95}Dy_{0.05}Br_3$ shows the 1 nm and 8 nm of red shift respectively with respect to $MAPbBr_3$ perovskite films.
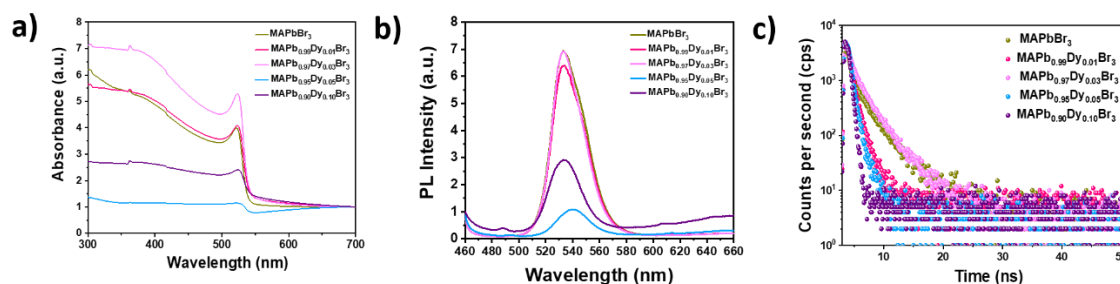
Figure 72 a) Absorbance spectra b) Emission Spectra c) TCSPC radiative decay of the perovskite films with different concentration of Dy^{3+}

Time correlated single photon counting was performed on the films to know the charge transfer dynamics in different films. The average lifetime values are shown below in Table 12. We have found in devices the highest doping concentration, the lowest is the radiative lifetime which suggests that these 5 wt% is optimum for our device performance. In our films, two lifetime decay processes are arising due to surface defects (τ_1) into the bulk (τ_2). Interestingly, in the films $MAPb_{0.95}Dy_{0.05}Br_3$ lifetime arising due to surface defects decrease and the lifetimes at bulk increases. These results suggest the possibility of fewer surface traps present in the films in comparison to other configurations of films.

Table 12 Lifetime decays Average fluorescence lifetime decays (τ_{av}), lifetime values (τ) and weighting coefficients for each decay channel (A) for the films prepared ITO/PEDOT: PSS/PSK

ITO/PEDOT: PSS/PSK	τ_{av} (ns)	τ_1 (ns)	A_1 (%)	τ_2 (ns)	A_2 (%)
$MAPbBr_3$	2.96	2.42±0.11	0.22	4.81±0.4	0.002
$MAPb_{0.99}Dy_{0.01}Br_3$	2.61	2.61±0.12	0.064	--	--
$MAPb_{0.97}Dy_{0.03}Br_3$	2.3	2.24±0.06	0.325	4.61±0.3	0.003
$MAPb_{0.95}Dy_{0.05}Br_3$	2.05	2.05±0.17	0.103	16.32±16.7	0.0
$MAPb_{0.9}Dy_{0.1}Br_3$	22.2	22.2±10.8	0.11	--	--

6.3.1.2 Structural Characterization

To prove the presence of dysprosium in the perovskite lattice, we have characterized the different doped and undoped perovskite by X-Ray Diffraction in the form of powder. For that, first we deposited different perovskite solutions on a clean glass substrate (cleaning process described in **Chapter 3**) with the same conditions as the devices. Then, after annealing, we scratched the films to carefully to collect our perovskite powders for XRD measurement. The XRD graph of different films collectively is shown in the Figure 73. The XRD pattern of MAPbBr$_3$ films matches with the literature[23]. From the following Figure, we can observe that the films which have the dysprosium shows more intense peak at 14.9^0 which corresponds to the (001) plane. On the other hand, MAPb$_{0.95}$Dy$_{0.05}$Br$_3$ film shows the most intense peak among all the samples which suggests that this concentration of dysprosium enhances the crystallinity of the perovskite more than in the other ratios. The XRD patterns also shows that all of the samples have the same cubic crystal structures.
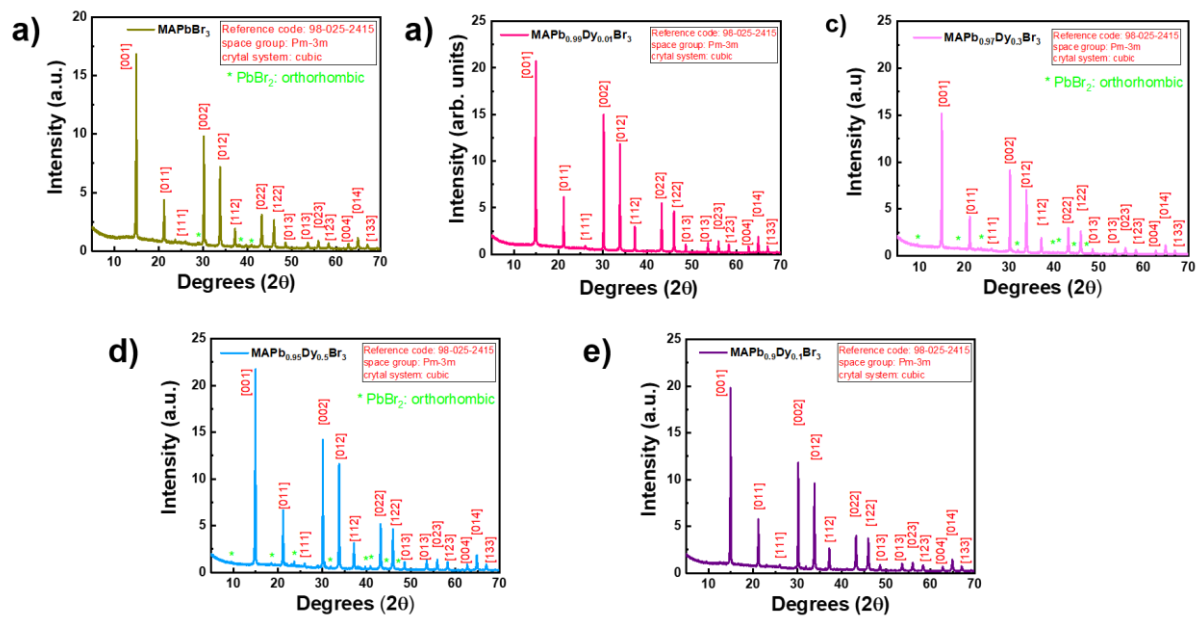
Figure 73 XRD patterns of the different perovskite powders

6.3.1.3 Morphological Characterization

We have characterized our films ITO/PSK with FE-SEM to observe the surface of our samples. For this, we have deposited different perovskite solutions on the ITO substrates. FESEM images of different films are shown in Figure 74. From the following figures, we find out that the $MAPb_{0.95}Dy_{0.05}Br_3$ films have not shown any white particles which can be the undissolved $PbBr_2$ and the increased grain size in this perovskite film shows the increased crystallinity shown in Figure 74 d).
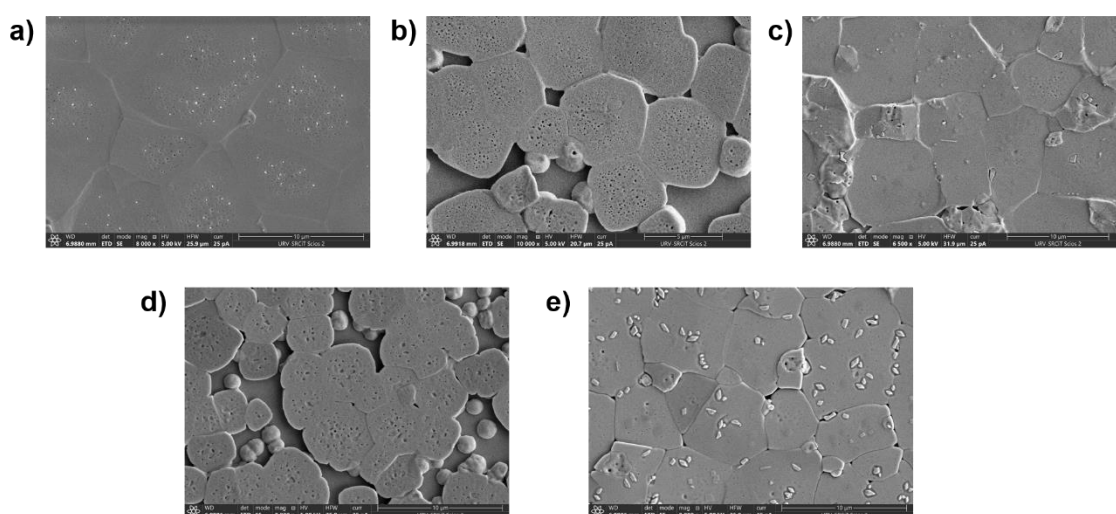
Figure 74 FESEM images of the films a) $MAPbBr_3$ b) $MAPb_{0.99}Dy_{0.01}Br_3$ c) $MAPb_{0.97}Dy_{0.03}Br_3$ d) $MAPb_{0.95}Dy_{0.05}Br_3$ e) $MAPb_{0.90}Dy_{0.10}Br_3$

6.3.2 Device Characterization

In our device structure, ITO/PEDOT: PSS (45 nm)/PSK (50 nm)/ TPBi (50 nm)/ LiF (0.8 nm)/ Al (100 nm), different doping concentrations of Dy^{3+} in $MAPbBr_3$ perovskite shows different luminance values shown in Figure 75 and Table 13. We have found that the luminance of the devices increases with the doping concentration of 3 wt% reaching maximum luminance value of 248 cd/m^2. With the further increase of Dy at 10 wt%, device performance decrease down to 25 cd/m^2. With 1 wt % of Dy^{3+}, the luminance of our device does not increase but it decreases the turn-on voltage in comparison to pristine device.
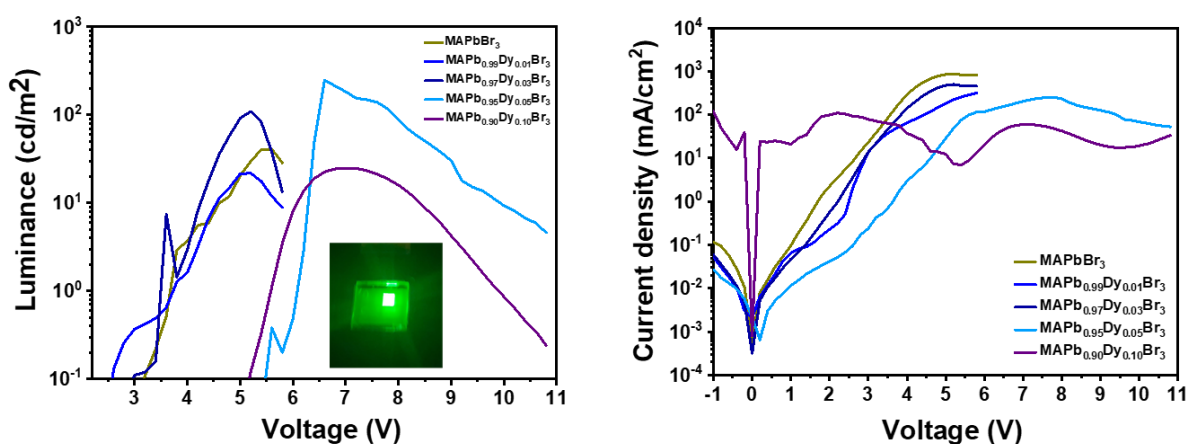
Figure 75 Device performance of the PeLEDs with different doping concentrations a) Luminance vs Voltage b) Current density vs Voltage

Table 13 Device performance of different perovskite films within the structure of ITO/PEDOT: PSS/TPBi/LiF/Al

ITO/PEDOT: PSS/PSK	Turn on Voltage (v_{On})	Max Luminance (cd/m^2)
$MAPbBr_3$	4	41
$MAPb_{0.99}Dy_{0.01}Br_3$	2.6	22
$MAPb_{0.97}Dy_{0.03}Br_3$	3	109
$MAPb_{0.95}Dy_{0.05}Br_3$	5.4	248
$MAPb_{0.90}Dy_{0.10}Br_3$	5.2	25

6.4 Conclusion

From our experiments, we have found that by doping with Dy^{3+} the $MAPbBr_3$ perovskite emissive layer of our green LEDs, the overall device performance gets enhanced. Our PeLEDs shows maximum luminance of 248 cd/m^2 with 5 wt% of Dy^{3+}. Hence, it is also the optimum concentration of Dy for the emissive layer in our PeLEDs. The decay lifetime of $MAPb_{0.95}Dy_{0.05}Br_3$ perovskite films are in correspond to the device results. Further, FESEM images and XRD data shows the enhanced crystallinity of $MAPb_{0.95}Dy_{0.05}Br_3$ which in-turns suggests the reasons of increased luminance of PeLEDs with optimum doping concentration of 5 wt %.

6.5 References

1. Quan, L. N. *et al.* Perovskites for Next-Generation Optical Sources. *Chem. Rev.* **119**, 7444–7477 (2019).

2. Wang, Qiang, et al. "Quantum confinement effect and exciton binding energy of layered perovskite nanoplatelets." *Aip Advances* 8.2 (2018).

3. Ma, J. & Wang, L. W. The Nature of Electron Mobility in Hybrid Perovskite CH3NH3PbI3. *Nano Lett.* **17**, 3646–3654 (2017).

4. Tan, Z.-K. *et al.* Bright light-emitting diodes based on organometal halide perovskite. *Nat. Nanotechnol.* **9**, 687–692 (2014).

5. Vashishtha, P. & Halpert, J. E. Field-Driven Ion Migration and Color Instability in Red-Emitting Mixed Halide Perovskite Nanocrystal Light-Emitting Diodes. *Chem. Mater.* **29**, 5965–5973 (2017).

6. Xie, G. *et al.* Stable mixed-cation perovskite light-emitting diodes. *Org. Electron.* **71**, 58–64 (2019).

7. Hong, W. L. *et al.* Efficient Low-Temperature Solution-Processed Lead-Free Perovskite Infrared Light-Emitting Diodes. *Adv. Mater.* **28**, 8029–8036 (2016).

8. Byun, J. *et al.* Efficient Visible Quasi-2D Perovskite Light-Emitting Diodes. *Adv. Mater.* **28**, 7515–7520 (2016).

9. Fakharuddin, A. *et al.* Reduced Efficiency Roll-Off and Improved Stability of Mixed 2D/3D Perovskite Light Emitting Diodes by Balancing Charge Injection. *Adv. Funct. Mater.* **29**, 1–12 (2019).

10. Protesescu, L. *et al.* Nanocrystals of Cesium Lead Halide Perovskites (CsPbX3, X = Cl, Br, and I): Novel Optoelectronic Materials Showing Bright Emission with Wide Color Gamut. *Nano Lett.* **15**, 3692–3696 (2015).

11. Zheng, C., Bi, C., Huang, F., Binks, D. & Tian, J. Stable and Strong Emission CsPbBr3 Quantum Dots by Surface Engineering for High-Performance Optoelectronic Films. *ACS Appl. Mater. Interfaces* **11**, 25410–25416 (2019).

12. Wei, Z. & Xing, J. The Rise of Perovskite Light-Emitting Diodes. *J. Phys. Chem. Lett.* **10**, 3035–3042 (2019).

13. Liu, Z. *et al.* Perovskite Light-Emitting Diodes with EQE Exceeding 28% through

a Synergetic Dual-Additive Strategy for Defect Passivation and Nanostructure Regulation. *Adv. Mater.* **33**, 1–9 (2021).

14.   Amgar, D., Binyamin, T., Uvarov, V. & Etgar, L. Near ultra-violet to mid-visible band gap tuning of mixed cation Rb: XCs1- xPbX3 (X = Cl or Br) perovskite nanoparticles. *Nanoscale* **10**, 6060–6068 (2018).

15.   Van der Stam, W. *et al.* Highly Emissive Divalent-Ion-Doped Colloidal CsPb1-xMxBr3 Perovskite Nanocrystals through Cation Exchange. *J. Am. Chem. Soc.* **139**, 4087–4097 (2017).

16.   Wang, Q. *et al.* Efficient sky-blue perovskite light-emitting diodes via photoluminescence enhancement. *Nat. Commun.* **10**, (2019).

17.   Yao, J. S. *et al.* Ce3+-Doping to Modulate Photoluminescence Kinetics for Efficient CsPbBr3 Nanocrystals Based Light-Emitting Diodes. *J. Am. Chem. Soc.* **140**, 3626–3634 (2018).

18.   Chen, Y. *et al.* An overview of rare earth coupled lead halide perovskite and its application in photovoltaics and light emitting devices. *Prog. Mater. Sci.* **120**, 100737 (2021).

19.   Zou, S. *et al.* Stabilizing Cesium Lead Halide Perovskite Lattice through Mn(II) Substitution for Air-Stable Light-Emitting Diodes. *J. Am. Chem. Soc.* **139**, 11443–11450 (2017).

20.   Pan, G. *et al.* Doping Lanthanide into Perovskite Nanocrystals: Highly Improved and Expanded Optical Properties. *Nano Lett.* **17**, 8005–8011 (2017).

21.   Venugopal, M., Padma Kumar, H., Satheesh, R. & Jayakrishnan, R. Tailoring the photoluminescent properties of samarium and dysprosium codoped calcium zirconate perovskites for WLED applications. *Int. J. Appl. Ceram. Technol.* **16**, 1228–1238 (2019).

22.   Choi, H., Kim, C. H., Pyun, C. H. & Kim, S. J. Luminescence of (Ca, La)S:Dy. *J. Lumin.* **82**, 25–32 (1999).

23.   Shen, H., Nan, R., Jian, Z. & Li, X. Defect step controlled growth of perovskite MAPbBr3 single crystal. *J. Mater. Sci.* **54**, 11596–11603 (2019).

Chapter 7: General Conclusion

Quantum dots are quasi zero-dimensional semiconductors whose size is smaller than the exciton Bohr radius and show quantum confinement effect. Hence, their 3-dimensional confinement results in discrete energy spectra which makes their band-gap dependent on the size of the nanocrystal. At present, quantum dots have grabbed scientists and industries' attention for their versatile application from biology to energy conversion field. On the other hand, self-assembled monolayers (SAMs) have been also applied extensively for electrode modification from the biomedical field to various devices.

The main goal of this thesis was to fabricate efficient LEDs with quantum dots and perovskite films as emissive material in an economic friendly way. We have used self-assembled molecules as thin charge transport layers for our QDLEDs and explored the doping of the perovskite as a strategy to increase the performance of the devices.

To do that, we have employed common lab techniques for the preparation of the devices and characterized materials and interfaces by optoelectronic and physicochemical measurements. The importance of a proper interfacial characterization has led us to relate the quality of the interactions between the charge transport layer and the emissive layer on the performance of the devices. Despite the fact that SAMs form ultrathin layers, their effect on the assembly of the photoactive layer layers is crucial for the performance of the devices. On the other hand, we have also explored a different strategy to enhance the performance of the devices which consists in the doping of the emissive layer. The obtained results open the way for further Optimization.

Therefore, the conclusions obtained in the experimental chapters are as follows:

Chapter 4: For investigating the suitable HTM materials for PeLEDs, we have employed our SAM molecules as HTMs in PeLEDs. Our main goal was to improve the overall performance of the PeLEDs including luminance and operational stability. In this study we have found that both our carbazole based SAMs EADR03 and EADR04 affect the formation of NCs films on the top of the molecules, in comparison to the PTAA and the blank prepared without HTM. The better interface between SAMs and NCs leads to increased luminance in the devices when compared to the PTAA and blank devices. Our investigation shows that the SAM HTLs enhance the charge injection abilities leading to lowering turn-on voltage of the devices in comparison to the reference devices.

Moreover, the EADR04 molecule gives rise to better stabilities of the devices, as demonstrated by lifetime measurements. This fact has been attributed to the extra phenyl moiety at the linkage part that enhances electron delocalization and thus, higher molecular stability. This observation opens the way for further tuning of the linker of SAMs to enhance stability and lifetimes of devices.

Chapter 5: This study was conducted in order find out if the widely known PDINO molecule can work as an ETL for the fabrication of CdSe@ZnS based red QDLEDs replacing other common materials to decrease the amount of material used in the preparation of the device while increasing the stability and the performance. We have found that the luminance of devices with PDINO as ETL is lower compared to the devices containing ETLs of PDINO/PEI and PEI. The film characterization, which is described in the chapter, indicates that the formation of CdSe@ZnS QDs film is smoother on the top of PEI rather than PDINO/PEI and in the case of PEI alone. The worse interface between the QD layer and PDINO leads to lower performance of our devices. The better charge balance in PEI based devices leads to higher luminance which is explained with trap density calculations. The stability measurements show that the devices with PDINO/PEI as ETL show longer lifetimes in comparison to the only PDINO or PEI based devices, which is also attributed to the interfacial quality. Therefore, despite the lower luminance, the use of PDINO can have beneficial effects on the stability, leading the way for further studies on the interface when mixed materials are used as charge transport layers.

Chapter 6 describes the preparation of $MAPb_{1-x}Dy_xBr_3$ perovskite solutions and their application in the fabrication of PeLEDs as an emissive layer. Our main goal was to study the effects of doping on the B-site of the perovskite to enhance the performance of the devices. From this study, we have found that the devices with 5 wt% doping concentration ($MAPb_{0.95}Dy_{0.5}Br_3$) show the maximum luminance in comparison to the pristine PeLEDs. The film characterization supports the successful insertion of Dy (III) into the lattice of perovskite increasing the crystallinity of the $MAPb_{0.95}Dy_{0.5}Br_3$ film. In addition to the enhanced performance of the devices, the use of paramagnetic ions could induce changes in the behavior of the devices when a magnetic field is applied. This effect will be studied in the future.

Annex i. Contribution to Scientific Community

1. **Kumari, S**., Sánchez, J. G., Imran, M., Aktas, E., González, D. A., Manna, L., ... & Palomares, E. (2023). Self-assembled molecules as selective contacts in CsPbBr 3 nanocrystal light emitting diodes. *Journal of Materials Chemistry C*, *11*(11), 3788-3795. This project was completed in ICIQ Tarragona.

2. Increasing the stability of CdSe@ZnS quantum dot light emitting diodes by PDINO as a functional electron transport layer. (to be Submitted)

Annex ii. List of Abbreviations

A	Ampere
AFM	Atomic Force Microscopy
Ag	Silver
AgCl	Silver Chloride
Al	Aluminium
Alq$_3$	Tris(8-hydroxyquinolinato) aluminium
Au	Gold
a.u.	Arbitary units
BPhen	Bathophenanthroline
Ca	Calcium
CsPbX$_3$	Cesium Lead Halide
C$_{60}$	Carbon Sixty
Cd	Candela
Cd/m^2	Candela per square meter (Luminance)
CdS	Cadmium Sulfphide
CdTe	Cadmium Telluride
CdSe@ZnS	Cadmium Selenide Zinc Sulphide
CdSeS@ZnS	Cadmium Selenium Sulphide
CIE	International Commission on Illumination
CV	Cyclic Voltammetry
DI water	Deionized Water
DMF	Dimethylformamide
DMSO	Dimethylsulfoxide
Dy	Dysprosium
EADR03	4-(3,6-bis(2,4-dimethoxyphenyl)-9*H*-carbazol-9-yl)benzoic acid

EADR04	4'-(3,6-bis(2,4-dimethoxyphenyl)-9*H*-carbazol-9-yl)-[1,1'-biphenyl]-4-carboxylic acid
EL	Electroluminescence
ETL	Electron Transporting Layer
ETM	Electron Transporting Material
EQE	External Quantum Efficiency
F8BT	Poly(9,9'-dioctylfluorene-co-benzothiadiazole)
FESEM	Field Emission Scanning Electron Microscopy
H	Hours
HOMO	Highest occupied molecular orbital
HIL	Hole Injection Layer
HTL	Hole Transporting Layer
HTM	Hole Transporting Material
HyLED	Hybrid Light Emitting Diodes
IPA	2-Propanol
ITO	Indium Titanium Oxide
LEDs	Light Emitting Diodes
LiF	Lithium Flouride
LUMO	Lowest Unoccupied Molecular Orbital
mA/cm^2	mili-ampere per square meter
$MAPbX_3$	Metal Lead Halide
MEH-PPV phenylene	Poly[2-methoxy-5-(2'-ethylhexyloxy)-1,4- vinylene
MoO_3	Molybdnum Oxide
NCs	Nanocrystals
NIR	Near Infra-Red
NPs	Nanoparticles
OA	Oleic Acid
ODE	Octadecene
OLA	Oleylamine

OLEDs	Organic Light Emitting Diodes
PCE	Power Conversion Efficiency
PDINO	2,9-Bis[3-(dimethyloxidoamino)propyl]anthra[2,1,9-def:6,5,10-d'e'f']diisoquinoline-1,3,8,10(2H,9H)-tetrone
PEDOT: PSS	Poly(3,4-ethylenedioxythiophene) polystyrene sulfonate
PEI	Polyethylenimine
PolyTPD	(N, N'-bis-4-butylphenyl-N,N'-bisphenyl)benzidine
PeLEDs	Perovskite Light Emitting Diodes
PL	Photoluminescence
PLQY	Photoluminescence Quantum Yield
PMMA	Polymethyl methacrylate
PSK	Perovskite
PTAA	Poly[bis(4-phenyl) (2,4,6-trimethylphenyl) amine
PVK	Poly (9-vinylcarbazole)
PQDs	Perovskite Quantum Dots
QDs	Quantum Dots
QDLEDs	Quantum Dot Light Emitting Diodes
QY	Quantum Yield
RMS	Root Mean Square
RPM	Revolution per Second
S	Second
SAMs	Self Assembled Monolayers
SnO_2	Tin Dioxide
TCSPC	Time co-related Single Photon Counting
TEM	Transmission Electron Miscroscopy
TiO_2	Titanium Oxide
$TBAPF_6$	Tetrabutylammonium hexafluorophosphate

TmPyPB	1,3,5-Tris(3-pyridyl-3-phenyl) benzene
TPBi	2,2',2''-(1,3,5-Benzinetriyl)-tris(1-phenyl-1-H-bbenzimidazole)
TPD diphenylbenzidine	N,N′-Bis(3-methylphenyl)-N,N′-
UV-VIS	Ultraviolet-Visible
UPS	Ultraviolet Photoelectron Spectroscopy
ZnO	Zinc Oxide
V	Voltage
VB	Valence Band
XRD	X Ray Diffraction
Zn(ac)$_2$·H$_2$O	Zinc Acetate Dihydrate
θ	Theta
λ	Lambda (Wavelength)
Ω/m^2	Ohm per square meter (Resistivity)
Cd/A	Candela per-Ampere
Nm	nanometer
m^2-kg /s	Meter square kilogram per second